NASA TM-80056

NASA Technical Memorandum 80056

CRACK PROPAGATION IN ALUMINUM SHEETS REINFORCED WITH BORON-EPOXY

G. L. Roderick

March 1979

National Aeronautics and Space Administration

Langley Research Center
Hampton, Virginia 23665

1 Report No	2 Government Accession No	3 Recipient's Catalog No
NASA TM-80056		

4 Title and Subtitle	5 Report Date
CRACK PROPAGATION IN ALUMINUM SHEETS REINFORCED WITH BORON-EPOXY	March 1979
	6 Performing Organization Code
7 Author(s)	8 Performing Organization Report No
G. L. Roderick	
	10 Work Unit No
9 Performing Organization Name and Address	505-02-43-02
Structures Laboratory U.S. Army Research and Technology Laboratories NASA-Langley Research Center Hampton, VA 23665	11 Contract or Grant No
	13 Type of Report and Period Covered
12 Sponsoring Agency Name and Address	Technical Memorandum
National Aeronautics and Space Administration Washington, DC 20546	14 Sponsoring Agency Code

15 Supplementary Notes

16 Abstract

The literature has shown that crack propagation in cracked metal sheets can be significantly reduced by bonding an uncracked reinforcement to the metal sheet. However, cyclic debonding typically occurs over a localized area near the crack. Herein, an analysis was developed to predict both the crack growth and debond growth in a reinforced system. The analysis was based on the use of complex variable Green's functions for cracked, isotropic sheets and uncracked, orthotropic sheets to calculate inplane and interlaminar stresses, stress intensities, and strain-energy-release rates. An iterative solution was developed that used the stress intensities and strain-energy-release rates to predict crack and debond growths, respectively, on a cycle-by-cycle basis. The analysis was verified with experiments.

The analysis was used in a parametric study of the effects of boron-epoxy composite reinforcement on crack propagation in aluminum sheets. The study showed that the size of the debond area has a significant effect on the crack propagation in the aluminum. For small debond areas the crack propagation rate is reduced significantly, but these small debonds have a strong tendency to enlarge. Debond growth is most likely to occur in reinforced systems that have a cracked metal sheet reinforced with a relatively thin composite sheet.

The analysis predicts crack growth in reinforced systems. Hence, the analysis can be applied in developing methods to repair damaged metal structures and to increase the lives and payloads of metal structures by selective reinforcement.

17 Key Words (Suggested by Author(s))	18 Distribution Statement
Reinforcement Aluminum Crack growth Fatigue Composite materials	Unclassified - Unlimited Subject Category 39

19 Security Classif (of this report)	20 Security Classif (of this page)	21 No of Pages	22 Price*
Unclassified	Unclassified	245	$9.50

* For sale by the National Technical Information Service, Springfield, Virginia 22161

CRACK PROPAGATION IN ALUMINUM SHEETS REINFORCED WITH BORON-EPOXY

by

G. L. Roderick

ABSTRACT

The literature has shown that crack propagation in cracked metal sheets can be significantly reduced by bonding an uncracked reinforcement to the metal sheet. However, cyclic debonding typically occurs over a localized area near the crack. Herein, an analysis was developed to predict both the crack growth and debond growth in a reinforced system. The analysis was based on the use of complex variable Green's functions for cracked, isotropic sheets and uncracked, orthotropic sheets to calculate inplane and interlaminar stresses, stress intensities and strain-energy-release rates. An iterative solution was developed that used the stress intensities and strain-energy-release rates to predict crack and debond growths, respectively, on a cycle-by-cycle basis. The analysis was verified with experiments.

The analysis was used in a parametric study of the effects of boron-epoxy composite reinforcement on crack propagation in aluminum sheets. The study showed that the size of the debond area has a significant effect on the crack propagation in the aluminum. For small debond areas the crack propagation rate is reduced significantly,

but these small debonds have a strong tendency to enlarge. Debond growth is most likely to occur in reinforced systems that have a cracked metal sheet reinforced with a relatively thin composite sheet.

The analysis predicts crack growth in reinforced systems. Hence, the analysis can be applied in developing methods to repair damaged metal structures and to increase the lives and payloads of metal structures by selective reinforcement.

TABLE OF CONTENTS

LIST OF FIGURES

LIST OF TABLES

LIST OF SYMBOLS

a	Half-length of crack, in
da/dN	Crack propagation rate in metal, in/cycle
$A(\zeta)$	Kernel for contour integration
A_c, B_c	Constant coefficients in stress functions for orthotropic sheet
A_o, B_o, C_o	Expressions used for determination of yielding of the adhesive layer
A_{11}, B_{11}, C_{11}, D_{11}	Constants for analysis of unsymmetrical beams under axial loads
AA	Integrals of displacement Green's functions for cracked metal sheet, in
b	Debond length along the y-axis, in
db/dN	Debond propagation rate along the y-axis, in/cycle
bb	Integrals used to find displacements from interlaminar shear stresses
BB	Integrals of displacement Green's functions for orthotropic sheet, in
BI	Complex function used in displacement Green's functions for cracked metal sheet, in
c_1	Constant coefficient in crack propagation equation for cracked metal sheet, in

c_2	Constant coefficient in debond propagation equation
[C]	Stiffness matrix for an isotropic sheet in plane stress, psi
C11, C12 C21, C22	Complex constants used in orthotropic stress analysis
d	Distance from test machine grips to change in cross section of debond specimen
[D]	Stiffness matrix for an orthotropic sheet in plane stress, psi
e	Numerical constant 2.718281824••••
e_o	Eccentricity of axial load in beam column analysis, in
E	Young's modulus of elasticity, psi
f	Interlaminar shearing stresses, psi
F	Aspect ratio of elliptical debond b/a
F_o	Complex function that relates pressure on a crack to displacement field, psi
F_p	Complex function that relates point loads to displacements in an uncracked isotropic sheet, in
F_1, F_2	Complex functions that relate remote stresses in a cracked metal sheet to displacements, in
F_3, F_4	Complex functions that relate remote stresses to displacements inan uncracked orthotropic sheet, in
F_5, F_6	Complex functions that relate interlaminar shear stresses to displacements in a cracked isotropic sheet, in

F_7, F_8	Complex functions that relate interlaminar sheet stresses to displacements in an uncracked orthotropic sheet, in
g	Increment of interlaminar stresses between loads that cause successive yielding of elements, psi
g_o	Complex function used in developing the displacement Green's functions for a cracked isotropic sheet
$\mathcal{G}$	Strain energy release rate, in-lb/in
G	Shear modulus, psi
G_{eff}	Effective shear modulus of the adhesive, psi
G1, G1A, G2, G3, G5, G6, G7	Complex functions used to express stress Green's functions for cracked isotropic sheet, psi
G8, G9	Complex stress functions used to express stress Green's functions for an uncracked orthotropic sheet, psi
GD	Displacement Green's functions for a cracked isotropic sheet, in
GS	Stress Green's functions for a cracked isotropic sheet, psi
HD	Displacement Green's functionsfor an uncracked orthotropic sheet, in
HS	Stress Green's function for an uncracked orthotropic sheet, psi
I(z)	Complex root of $\sqrt{z^2 - a^2}$ defined by $\lim_{z \to \infty} \frac{I(z)}{z} = 1$, in
II(z)	Complex integral used in developing displacement Green's functions for a cracked isotropic sheet

J	Path independent integral used to determine the strain energy release rate
k_o	Constant used in Von Mises yield criterion
K_o	Constant for one-dimensional analysis
k_1	Stress intensity for mode I, psi-in$^{\frac{1}{2}}$
k_2	Stress intensity for mode II, psi-in$^{\frac{1}{2}}$
k_{1c}	Critical mode I stress intensity at failure, psi-in$^{\frac{1}{2}}$
k_f	Stress intensity factor
m	Ratio of the shear modulus and Young's modulus for the orthotropic sheet G_{xy}/E_y
M	Moment in beam column analysis, in-lb
n_1	Exponent for crack propagation equation for metal sheet
n_2	Exponent for debond propagation equation
n	Ratio of the Young's moduli of the orthotropic sheet, Ex/Ey
p_1, p_2	Complex constants for orthotropic stress analysis
$p(t)$	Normal stress acting on crack surface, psi
P	Axial load used in beam column analysis, lbs
q_1, q_2	Complex constants for orthotropic analysis
$q(t)$	Shear stress acting on crack surface, psi
r, Θ	Polar coordinates, in, deg
r_o	Small radius for contour integration, in
R	Ratio of minimum to maximum load in a load cycle
R_o	Large radius for contour integration, in
s	Remote stress applied to the reinforced system in the y-direction, psi

s_1, s_2	Complex roots from the governing equation for orthotropic sheets in plane stress or strain
S	Complex representation of point load acting in complex plane per sheet thickness lbs/in
t	Thickness of adherends or adhesive, in
u, v, w	Displacements in cartesian coordinates in the x, y, and z-directions respectively, in
U	Internal strain energy, in-lbs
V	Shear in beam, lbs
w_1, w_2	Complex variables for orthotropic analysis
W	External work, in-lbs
W_e	Strain energy density
x, y, z	Cartesian coordinates
x_0, y_0	Cartesian coordinates of point of load application in the complex plane, in
X, Y	Unit load components in the x and y-directions respectively, lbs
XA, XB, XC, XI	Complex functions used in the displacement Green's functions for a cracked isotropic sheet, in
XK	Complex function used as Green's function for stress intensities, psi-$in^{\frac{1}{2}}$
z	Complex variable for analysis of isotropic sheet
z_1, z_2	Complex variables for analysis of orthotropic sheet
α	Constant for shear lag analysis, in
β	Constant for shear lag analysis
γ	Shear strain in the adhesive

δ	Axial deformation, in
Δ	Operator to denote small change in quantities
ε	Strain
ζ	Complex variable for contour integration
$\Theta\Theta$	Rotation in beam
ν	Poisson's ratio
π	Constant 3.1415926535
σ	Stress, psi
σ_m	Stress in metal, psi
σ_c	Stress in composite, psi
T	Shear stress in the adhesive, psi
ϕ	Stress function for isotropic sheet
Φ	Derivative of stress functions for isotropic sheet, ϕ'
Φ_1, Φ_2	Stress functions for orthotropic sheet
ψ	Stress function for isotropic sheet
Ψ	Derivative of stress function for isotropic sheet, ψ'
ω	Stress function for isotropic sheet
Ω	Derivative of stress function for isotropic sheet, ω'
η	Constant for plane stress or strain used in complex variable formulation

Subscripts

ad	Adhesive
c	Composite adherend
m	Metal adherend
xy	Quantity in the x-direction due to a load in the y-direction

xx	Quantity in the x-direction due to a load in the x-direction
yx	Quantity in the y-direction due to a load in the x-direction
yy	Quantity in the y-direction due to a load in the y-direction

Superscripts

$\overline{\quad}$	Conjugate value, if $z = x + iy$ then $\overline{z} = x - iy$ and if $F(z) = A + iB$ then $\overline{F(z)} = A - iB$ and $\overline{F}(z) = \overline{F(\overline{z})}$.

CONVERSIONS FROM CUSTOMARY TO SI UNITS

FORCE

Pound force (lb) = 4.448 Newtons (N)

PRESSURE

Stress (psi) = 6894 Pascals (Pa)

DISTANCE

Inches (in.) = 0.0254 meters (m)

ENERGY

Foot-pound force (ft-lb) = 1.355 Joules (J)

TEMPERATURE

Fahrenheit (^{o}F) = 5/9 (t_F - 32) Celsius (^{o}C)

CHAPTER I

THE USE OF COMPOSITE REINFORCEMENT TO PREVENT FATIGUE FAILURE IN AIRCRAFT

A potential cause of aircraft crashes is fatigue failure. As shown by Hardrath (1971), most types of civil aircraft have experienced some form of fatigue problem. In addition Lowndes and Miller (1969) indicate that fatigue failures have frequently occurred in military aircraft. In some cases the fatigue failures led to loss of lives and the aircraft. In efforts to eliminate such failures, both government research laboratories and aircraft manufacturers have studied the fatigue failure process in depth. These studies showed that the rate at which the fatigue damage develops in metals is a function of the stress level in the structure and occurs in three stages: crack initiation, stable crack propagation, and unstable crack propagation (catastrophic failure). Although aircraft structures can be designed to have stresses low enough to prevent fatigue failures, the weight penalty would be enormous and would make the aircraft uneconomical to operate. Hence, a trade-off exists between low stresses and low weight, and weight efficient structures will almost always have stresses high enough to support fatigue damage accumulation.

Fatigue cracks initiate at local stress concentrations in the structure The local stress concentrations may be caused by poor

fatigue design, by manufacturing defects in the material, or by damage caused by the flight environment. Although methods can be employed to reduce the occurrence of fatigue crack initiation, the development of such cracks seems almost inevitable.

Once a crack initiates it grows at a stable rate until it reaches some predictable, critical length after which catastrophic failure follows. Fortunately, in aluminum aircraft structures the critical crack length is large and the crack is easy to detect long before it reaches a critical length. Consequently, fatigue cracks can be tolerated in an aircraft structure as long as the structure is inspected periodically to locate cracks before they become critical. Of course, once the crack is detected it must be repaired before it becomes critical. The repair can be made by either replacing the component or by repairing it in situ. Because replacing a component may involve high cost and keep the aircraft out of service for extended periods of time, repairing the component in situ is frequently very desirable.

Basically, a fatigue crack can be repaired by reducing the stress state in the vicinity of the crack tip. One method of reducing the stress state is to reinforce the crack with unidirectional composite (fibers are perpendicular to plane of crack). The composite reinforcement reduces the stress state near the crack tip by two mechanisms. First, adding the composite reinforcement lowers the overall stress in the cracked metal by increasing the cross-sectional area and by providing an alternate, stiffer load path by virtue of the high modulus of the composite. This reduction in stress can be easily

calculated by simple strength of materials theory and, hence, is easy to investigate. The second mechanism comes from the development of stresses between the metal and composite adherends. Several papers (Kula et al 1973, Ellis 1976, Johnston and Stratton 1975, Ratwani 1977) have shown that these interlaminar stresses have a profound effect on crack propagation. These interlaminar stresses reduce the stresses near the crack tip and, consequently, retard its growth. As will be shown later, the investigation of these interlaminar stresses requires a much more extensive analysis than that provided by strength of materials theory.

Consequently, a need exists for the development of a realistic fatigue analysis that incorporates the effects of the interlaminar stresses. Accordingly, the objective of this dissertation was to develop such an analysis and use it to study the effects of composite reinforcement on the fatigue life of cracked metallic structure.

To meet this objective the following approach was taken. First, in Chapter II the fatigue behavior of the constituents of the reinforced system was characterized. Next in Chapter III the fatigue behavior of the reinforced system was studied experimentally. Then, in Chapter IV with the use of the results of Chapters II and III and complex variable theory, a static analysis was developed that related applied loads, adherend thicknesses, debond size, and crack length to crack propagation rates. Next, in Chapter V the analysis was further developed to predict both debond and crack growth as a function of applied load cycles. The accuracy of the analysis was investigated in Chapter VI. Finally, in

Chapter VII the analysis was used to parametrically study crack propagation in reinforced systems.

Throughout the development of the analysis many items required detailed analytical or experimental investigation. These investigations were developed and discussed in several appendices.

CHAPTER II

FATIGUE BEHAVIOR OF THE REINFORCED SYSTEM CONSTITUENTS

The reinforced system that will be considered herein is composed of adherends made out of two dissimilar materials, an aluminum sheet and a composite sheet, that are bonded to each other with a relatively thin, room-temperature curing adhesive. This system is intended to model the repair of a cracked, aluminum aircraft component that is repaired by bonding a composite sheet to it. Each of the three constituents of the system - the metal, the composite, and the adhesive - exhibits different fatigue behavior and plays an important role in the fatigue behavior of the reinforced system. Consequently, to analyze the fatigue process in the system, the fatigue behavior of each of the constituents needs to be understood. In the following sections the fatigue behavior of each of the constituents will be discussed and analysis methods formulated.

Fatigue of Metals

As pointed out by Erodogan (1968), the fatigue process in metals occurs in three different stages: crack initiation, stable crack growth, and unstable crack growth (fracture). Current aircraft design methods focus on the latter two stages of the fatigue process by using a "Damage Tolerant Design Philosophy" (military specification

MIL-A-83444). This philosophy, as far as fatigue damage accumulation is concerned, admits that initial flaws such as cracks, exist in aircraft components that are fatigue critical, i.e. may fail under cyclic loading. But, the philosophy also assumes that these initial cracks grow stably and can be detected during periodic inspections before they reach a critical crack length. Once the damage is detected, it can be repaired. Hence, the validity of this philosophy rests on the accurate prediction of crack growth rate and critical crack length. Fracture mechanics theory can be used to determine both crack growth rate and critical crack lengths.

Fracture mechanics theory was conceived when Griffith (1921) related fracture to an energy balance as the crack extended. In 1957 Irwin related the stress state at the crack tip to fracture. A schematic of a crack tip and equations for the stresses very close to it (Sih and Liebowitz 1968) are shown on figure 1 (additional terms not shown in the equations have a negligible effect on the stress state near the crack tip). As may be seen from the equations, as the distance from the crack tip, r, approaches zero the stresses become infinite. Consequently, at the crack tip where the stresses are infinite a singularity exists.[1] The coefficients of the stress distributions, k_1 and k_2, are the stress intensity factors which are used extensively in fracture mechanics. The Mode I stress intensity designated by k_1 is associated with the stresses that deform the crack surfaces symmetrically with respect to the original plane of

---

[1] In reality infinite stresses cannot exist in the material and local yielding of the material occurs. This local yielding is ignored in linear elastic fracture mechanics.

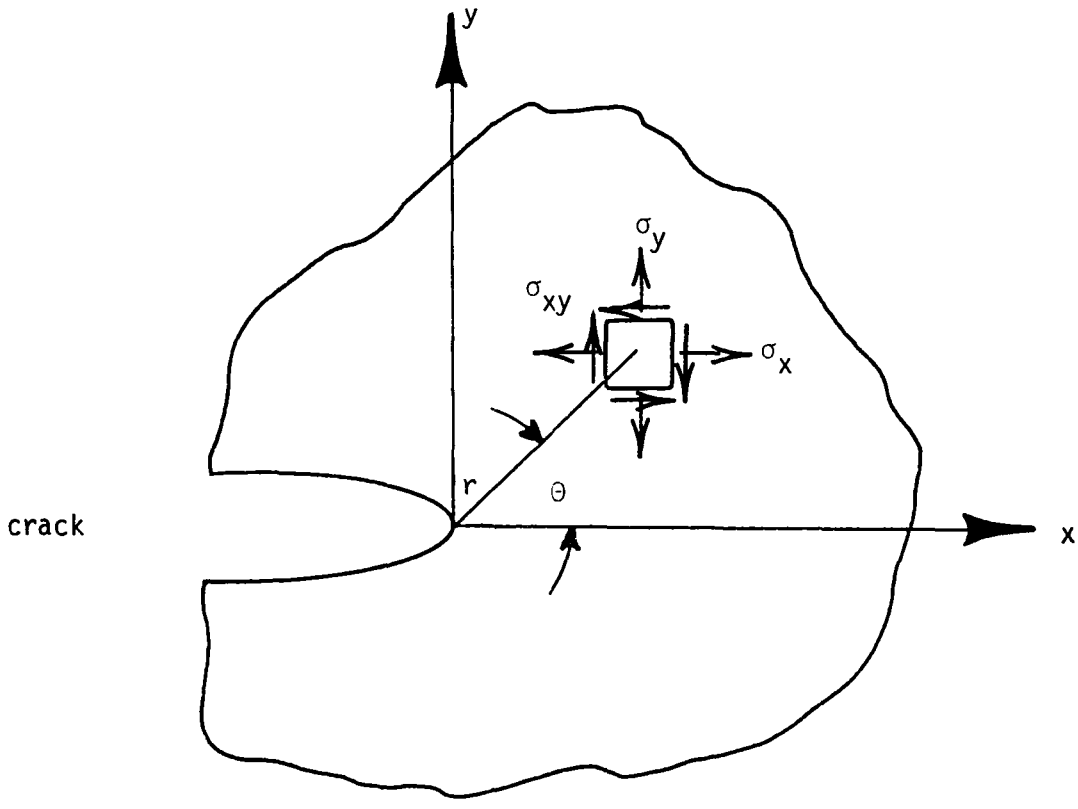

Symmetric loading (Mode I)

$$\sigma_x = \frac{k_1}{(2r)^{\frac{1}{2}}} \cos\frac{\Theta}{2}\left[1 - \sin\frac{\Theta}{2}\sin\frac{3\Theta}{2}\right]+\ldots$$

$$\sigma_y = \frac{k_1}{(2r)^{\frac{1}{2}}} \cos\frac{\Theta}{2}\left[1 + \sin\frac{\Theta}{2}\sin\frac{3\Theta}{2}\right]+\ldots$$

$$\sigma_{xy} = \frac{k_1}{(2r)^{\frac{1}{2}}} \cos\frac{\Theta}{2}\sin\frac{\Theta}{2}\cos\frac{3\Theta}{2}+\ldots$$

Skew-symmetric loading (Mode II)

$$\sigma_x = -\frac{k_2}{(2r)^{\frac{1}{2}}} \sin\frac{\Theta}{2}\left[2 + \cos\frac{\Theta}{2}\cos\frac{3\Theta}{2}\right]+\ldots$$

$$\sigma_y = \frac{k_2}{(2r)^{\frac{1}{2}}} \sin\frac{\Theta}{2}\cos\frac{\Theta}{2}\cos\frac{3\Theta}{2}+\ldots$$

$$\sigma_{xy} = \frac{k_2}{(2r)^{\frac{1}{2}}} \cos\frac{\Theta}{2}\left[1 - \sin\frac{\Theta}{2}\sin\frac{3\Theta}{2}\right]+\ldots$$

Fig. 1. Stress distribution near crack tip

the crack while the Mode II stress intensity designated by k_2 is associated with stresses that cause shear displacements between the crack surfaces. In 1960 Sanders showed that the stress intensities were related to the strain energy release as the crack extended. Hence, the stress state near the crack tip was related to the Griffith theory of fracture, and the foundation of fracture mechanics was formed.

The stress intensities can be determined from complex stress functions determined from the theory of elasticity (Sih and Liebowitz 1968) as

$$k_1 - ik_2 = 2\sqrt{2} \lim_{z \to a} \{\sqrt{z - a}\ \Phi(z)\} \tag{1}$$

where

$$z = x + iy \quad \text{and} \quad i = \sqrt{-1}$$

and x and y are the cartesian coordinates and $\Phi(z)$ is the complex stress function as developed by Muskhelishvili (1975) that satisfies the equations (plane strain or stress)

$$\sigma_x + \sigma_y = 2[\Phi(z) + \overline{\Phi(z)}] \tag{2}$$

$$2i\sigma_{xy} - \sigma_x + \sigma_y = 2[\bar{z}\Phi'(z) + \Psi(z)] \tag{3}$$

where σ_x, σ_y and σ_{xy} are the stresses in the cartesian coordinates and $\Psi(z)$ is another stress function. The two stress functions are

functions of both the loading conditions and the configuration of the body and will be discussed in detail in later chapters.

The stress intensities can be related to both crack propagation rates and critical crack lengths. On the basis of the Griffith theory of fracture, a critical value of the strain energy release can be found and hence, according to Sanders (1960) a critical value of the stress intensity can be found. For the material used in this study, 2024-T3 aluminum, Hudson (1969) showed that the critical value for k_{1C} is 56,000 psi-in$^{\frac{1}{2}}$. Hence, with the use of equation (1) and the appropriate stress functions, the fracture can be predicted.

Cyclic crack growth rates were related to the stress intensity by Paris (1961) by the empirical formula

$$da/dN = C(k_1)^4$$

where da/dN is the crack propagation rate, C is am empirical constant and k_1 indicates the stress intensity range during cyclic loading. Forman et al (1967) improved this equation by including the critical stress intensity k_{1C} and the stress ratio R, which is the ratio of the minimum to maximum stress in the loading cycle, in the empirical formula

$$da/dN = \frac{c_1(k_1)^{n_1}}{(1-R)k_{1C} - k_1} \qquad (4)$$

where c_1 and n_1 are empirical constants and $k_{1C} = 56{,}000$ psi-in$^{\frac{1}{2}}$.

For 2024-T3 aluminum Hudson (1969) showed that the constants c_1 and n_1 have the values

$$c_1 = 3.22 \times 10^{-14}$$

$$n_1 = 3.38$$

As the previous discussion implies, once the stress functions for a cracked body are known, the stress intensities can be calculated. With the stress intensities both the crack propagation rate and critical crack length can be predicted. The crack propagation rate and critical crack length can be used in a Damage Tolerant Design Philosophy to predict life of aircraft components. The life is predicted by first assuming that the structure contains cracks. The lengths of these cracks are assumed to be the largest crack detected in the structure or the largest crack which can be overlooked due to the resolution of the inspection technique. Then, by using the assumed or detected crack length and fracture mechanics theory, the number of load cycles to fracture can be predicted. On the basis of these calculations, inspection intervals are determined to assure that cracks can be detected and repaired before they reach a critical length.

Fatigue of Bonded Systems

To perform a realistic fatigue analysis of the reinforced system, the fatigue behavior of the adhesive in situ, herein called the bond, must be characterized. Several researchers have shown that the bond deteriorates when subjected to a cyclic load. Within this dissertation this deterioration will be called debonding. Hoffman and June

(1973) studied debonding by recording the debond propagation as a function of applied load cycles. They showed that a myriad of factors such as type of adhesive, adherend and adhesive thickness, method of curing, and aging all affect the debonding. Roderick et al (1976) showed that debonding could occur as failure within the adhesive as a cohesive failure, between the adhesive and an adherend as an adhesive failure, or in the composite material. Because of the variety of failure modes, the analysis of the debonding is difficult. The most progress in analysis of debonding appears to stem from the energy approach developed by Griffith (1921).

The first application of the energy approach appears to be by Rippling et al (1964) in the study of fracture toughness of bonded joints. Since Rippling's paper, Mostovoy and Ripling have published several other papers on fracture toughness of bonds: Mostovoy and Rippling 1966, Mostovoy et al 1967, Mostovoy and Rippling 1971. However, a correlation between the fracture energy and the stress state near the debond tip has not been made in the bonded systems. Wang et al (1976) showed that a primary reason for the lack of correlation appears to be the development of large regions of plastic yielding in the adhesive. Hence, linear elastic fracture mechanics based on small yield zones and stress intensities at a crack tip do not appear applicable to bonded systems.

However, by applying an energy approach, Roderick et al (1975) showed that the debond propagation rates can be correlated for specimens with different thickness adherends with a Paris (1961) type equation

$$db/dN = c_2(G)^{n_2} \qquad (5)$$

where both c_2 and n_2 are empirical constants for a specific bond system and G is the strain energy released as the debond extends.

As shown by Roderick et al (1976), the parameters c_2 and n_2 vary for different bonded systems. The bond system used in this dissertation was 2024-T3 aluminum bonded to unidirectional boron/epoxy with a room temperature curing adhesive, Shell EA-934. For this system the empirical constants were determined by methods discussed in Appendix A and were found as

$$c_2 = 3.158 \times 10^{-5}$$

$$n_2 = 3.616$$

With these constants, a value for the strain energy release rate, G, and equation (5), the debond growth rate can be predicted. The calculation of G for debonding in the reinforced system will be discussed in detail in Chapter V.

Fatigue of Composite Materials

The term "composite" may refer to a myriad of systems composed of a wide spectrum of different types of fibers and matrices. Furthermore, each system may have widely different fatigue characteristics depending upon the fiber orientations, stacking sequences, and loading conditions. Durchlaub and Freeman (1974) showed that fatigue damage in composites may occur perpendicular to, parallel to, or at an

angle to the loading axis depending upon the fiber orientation. Foye and Baker (1970) showed that the lives of composite laminates could vary as much as an order of magnitude by changing their stacking sequences. Reifsnider et al (1974) showed that changing the frequency of the applied cyclic load affects both the mode of failure and the fatigue life As evident from these observations, the fatigue behavior of composite materials is complex.

Currently the understanding of the fatigue process in composites appears primitive although some progress in developing an understanding has been made. As pointed out by Salkind (1973), fatigue failure in composites can occur in different failure modes such as matrix cracking, delamination, and fiber fracture. Also, evidence exists that suggests that the fatigue process is a result of primarily matrix deterioration (Roderick and Whitcomb 1977). If matrix deterioration is the primary cause of fatigue in composites, then the various failure modes could be explained in terms of different stress states in the matrix depending upon the fiber orientation and stacking sequences of a specific laminate. Hence, those laminates in which the matrix is highly stressed would most likely degrade under cyclic load while those laminates in which the matrix is lightly stressed would not.

Following this line of thought, composites in which the fibers transmit the load, fiber controlled composites, would have long fatigue lives while those in which the matrix transmits the load, matrix controlled composites, would have short lives. An example of a fiber controlled composite is a unidirectional laminate loaded along the axis. On the other hand, an example of a matrix controlled laminate is one

in which the fibers are at 45° angles to the loading axis. As shown by Durchlaub and Freeman (1974), the matrix controlled laminate does degrade rapidly under cyclic loading while the fiber controlled laminate does not.

Two basic approaches to predict the diverse fatigue behavior of composite materials are currently being developed by researchers. In the first approach, the laminate behavior is described by a statistical model (Halpin et al 1972) that relates the static strength and fatigue life distributions by assuming that the residual strength of the laminates degrades monotonically (Yang and Liu 1977). Because this method is based on experimental results, it can be applied easily. However, it does not apply to laminates whose residual strength does not decrease monotonically[2] with applied load cycles. Also, this method requires extensive testing every time the stacking sequence or fiber orientation changes.

The second approach as developed by McLaughlin et al (1975) couples basic fatigue data on the laminae level with a stress analysis to predict both the mode of fatigue failure and the fatigue lives of laminates. Because this approach is based on laminae data rather than laminate data, it can be used to predict the fatigue behavior of laminates with different stacking sequences and fiber orientations without extensive testing.[3] The major drawback to this approach is its

---

[2]Durchlaub and Freeman (1974) showed that the residual strength of notched laminates could increase after fatigue loading.

[3]The analysis originally proposed by McLaughlin et al did not consider interlaminar stresses and therefore could not account for changes in stacking sequences, but incorporation of interlaminar stresses into the analysis has been done and will be shown in a NASA contractors report released in 1978.

complexity in attempting to develop simple, realistic stress analyses and a failure criterion on the laminae level.

The state of the art of fatigue analysis, in the author's opinion, is still in the early stages of development and not yet capable of reliable life predictions for general laminates. As a consequence the fatigue behavior of the unidirectional boron/epoxy used in the present study cannot be described by relatively simple fatigue analyses as was the case for the cracked metal sheet and the bond system. Accordingly, the fatigue behavior will be determined solely by experimental data.

Shockey et al (1970) showed that unidirectional boron/epoxy laminates that were loaded along the fiber axis had an average ultimate tensile strength of 193 ksi; when these laminates were cycled under constant amplitude cyclic loading with R = 0.1, they retained 73 percent of their ultimate tensile strength after 10^7 applied load cycles. Consequently, in an attempt to prevent failure in the unidirectional boron/epoxy, stress along the fiber axis (based on laminate analysis) was kept below 140 ksi.

Having discussed the fatigue behavior of the constituents of the reinforced system in this chapter, the next chapter deals with the fatigue behavior of the constituents in situ in the reinforced system. Hence, the next chapter discusses fatigue tests of reinforced systems.

CHAPTER III

FATIGUE TESTS OF REINFORCED SYSTEMS

To determine the fatigue behavior of the reinforced system, two large panels were manufactured and tested. The panels shown on figure 2 were made of 8 x 24 inch sheets of 2024-T3 aluminum and unidirectional boron/epoxy. EA-934 room temperature curing adhesive was used to join the sheets with the bonding process described in Appendix A. The primary difference between the panels labeled A and B on figure 2 was the thickness of the metal and composite adherends. To simulate a crack, the metal adherend contained a through-the-thickness narrow slit 0.01 inch wide and 2 inches long. The slit, which was made by an electrical discharge process, was centered along the horizontal centerline of the panels. In both panels the fibers of the unidirectional composite run parallel to the longitudinal axis of the panels.

The panels were tested in a 300,000 pound load capacity servo-hydraulic fatigue machine. Both panels were tested under constant amplitude loading with R, the ratio of the minimum to maximum stress in the load cycle, equal to 0.01 at a test frequency of 2.5 Hz.[4] For the fatigue tests of both panels the distance between test machine grips was 16 inches. The maximum loads applied to each panel

---

[4]The test frequency was limited to 2.5 Hz instead of the 10 Hz used to characterize the debond behavior in Appendix A because of test machine limitations.

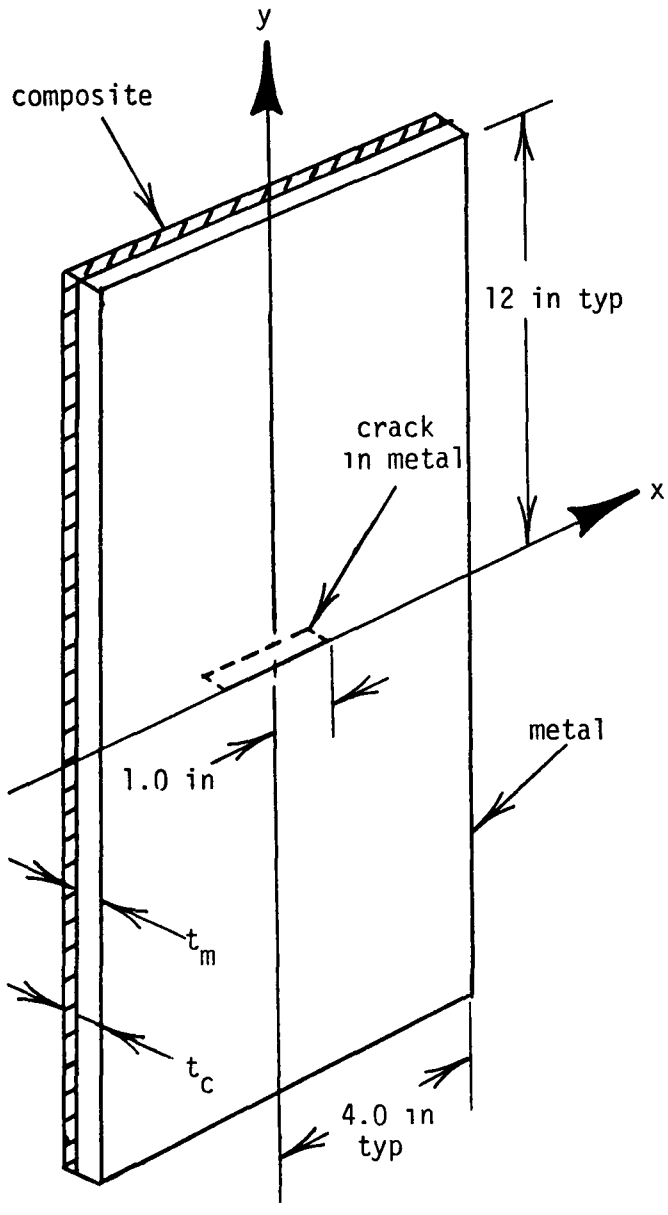

Panel	thickness metal t_m	thickness composite t_c
A	0.156 in	0.028 in
B	0.051 in	0.048 in

Fig. 2. Panel configuration

during the fatigue tests and the corresponding stresses in the adherends calculated from membrane laminate theory (see Appendix C) are shown below.

Panel	Maximum Load lbs	Stress, psi metal	composite
A	37,600	19,600	58,600
B	22,500	14,600	43,100

During the fatigue tests, crack lengths were measured periodically with an optical microscope. Table 1 shows the measured crack lengths and applied load cycles for both tests. The crack lengths are plotted against the applied load cycles on figure 3. Note that on the figure the abscissa is logarithmic and the ordinate starts at the initial half-crack length of $a = 1.0$ inch. The crack propagation rates for the panels are the slopes of the curves shown on figure 3. These rates are tabulated in Table 1 and plotted against the half-crack length on figure 4. As evident from figure 4, the crack growth rate is about two orders of magnitude larger in Panel A than in Panel B.

The crack propagation rates in these panels is a function of debonding between the adherends. If the adherends were completely debonded the crack propagation rate would be much larger than if no debonding occurred. To investigate the effect of debond size on crack propagation rate, the test panels were examined with an ultrasonic C-scan (details of the C-scan method are discussed in detail by McMaster 1963) after the half-crack length grew to 1.0 inch. Figure 5 shows the C-scans of the panels. On the figure the dark parts of the

TABLE 1

CRACK LENGTHS AND CRACK PROPAGATION RATES

	Panel A		Panel B	
half-crack length a, in	cycles *N	crack propagation rate da/dN x 10^{-5}	cycles *N	crack propagation rate da/dN x 10^{-5}
1.05			44,800	
				0.236
1.10	1,570		65,940	
				0.312
1.15		7.57	81,975	
				0.217
1.20	3,220		105,000	
				0.33
1.25		9.02	120,130	
				0.369
1.30	4,440		133,675	
				0.311
1.35		10.8	149,740	
				0.328
1.40	5,540		164,980	
				0.339
1.45		11.6	179,695	
				0.321
1.50	6,790		195,250	
				0.277
1.55		12.0	213,310	
				0.299
1.60	7,790		230,025	
				0.275
1.65		12.2	248,180	
1.70	8,690		. . . .	
1.75		13.0	279,795	
				0.295
1.80	9,690		296,765	
				0.323
1.85		13.0	312,260	
				0.339
1.90	10,680		326,990	
				0.312
1.95			342,990	
2.00			. . . .	

*N - Instead of listing the number of cycles that caused crack growth at both crack tips, the average number of cycles is given.

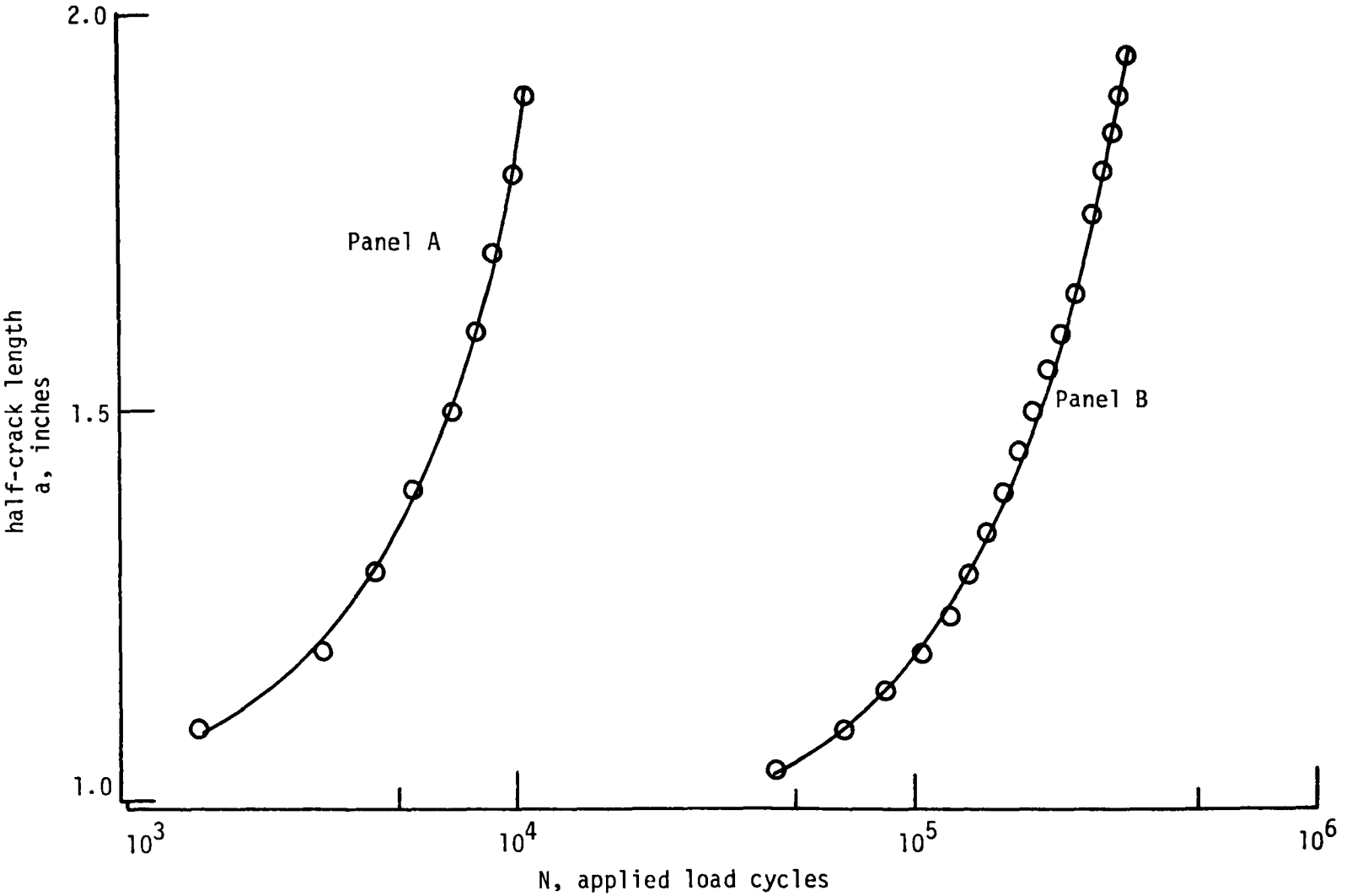

Fig. 3. Crack growth versus applied load cycles

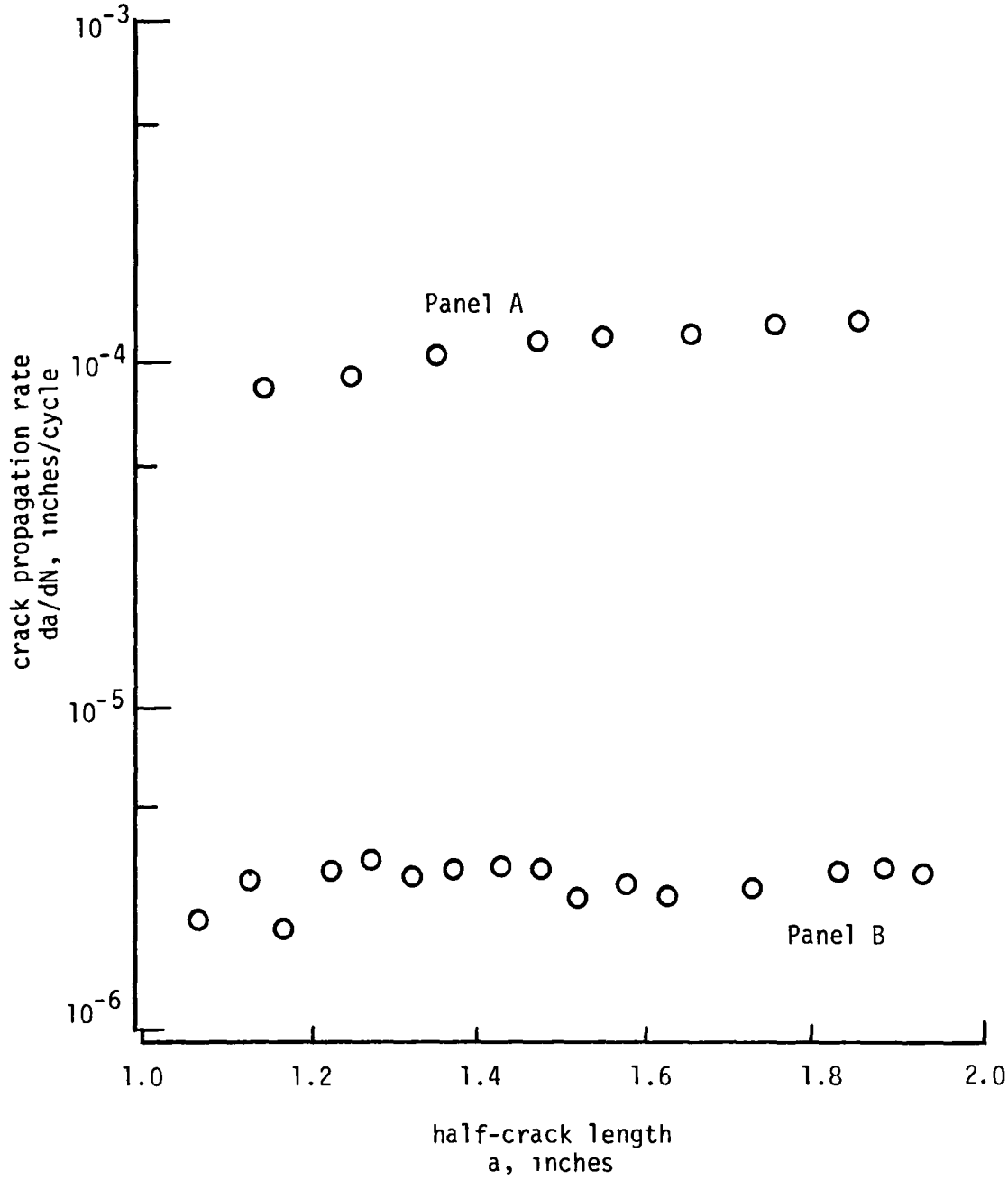

Fig. 4. Experimental crack propagation rates

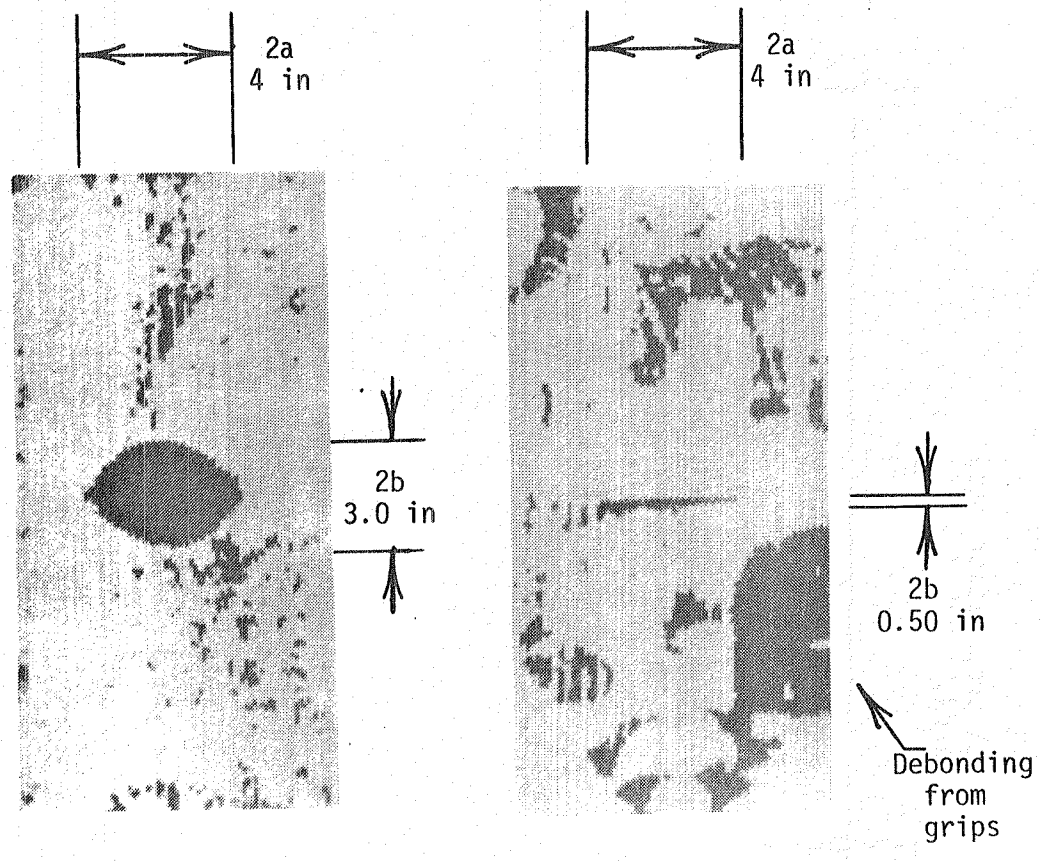

Specimen A

$F = \frac{a}{b} = 0.75$

Specimen B

$F = \frac{a}{b} = 0.125$

Fig. 5. Ultrasonic C-scans of fatigued specimens

C-scans are areas where debonding has occurred. As evident from the figure debonding occurred over an elliptical area. Ratwani (1977) has observed similar elliptical debonds in metal laminates. The major axes of the elliptical debonds were nearly equal to the crack length in the metal adherend of the panels. As measured from figure 5 the minor axes of the debonds were 3.0 inches and 0.50 inch for Panels A and B respectively. However, when the C-scans shown on figure 5 were made, they were distorted along the longitudinal axes of the panels. By taking into account this distortion, the minor axes of Panels A and B were found to be 4.0 and 0.67 inches respectively. With these corrected values of debond length along the minor axes, the ratios of minor to major axes of the debonds, $F = b/a$, were found as 1.0 and 0.14 for Panels A and B respectively.

The experiments discussed in this chapter showed that the fatigue in reinforced systems occurs as collinear crack growth and debond growth over an approximately elliptical area. In Chapters IV and V an analysis will be developed that can model this observed behavior. In Chapter VI the analysis will be verified by comparing the experimental results of this chapter with results of the analysis.

CHAPTER IV

STRESS ANALYSIS

As shown in the previous chapter, under cyclic loads the reinforced system exhibits both crack and debond growth. Intuitively, the rate at which the debond and crack propagates is a function of the stress state and level in the system. Consequently, to predict these rates a realistic stress analysis is required. For the stress analysis to be realistic it must predict stresses in the adhesive as well as in the adherends of the system. Because adhesives typically exhibit nonlinear behavior (Hughes and Rutherford 1968), the stress analysis must include nonlinear behavior of the adhesive. The first step in development of a realistic, nonlinear, elastic stress analysis is the formulation of a linear elastic stress analysis.

Formulation of Linear Elastic Solution

To formulate an elastic solution, the reinforced system shown in figure 6 was considered. As shown in figure 6, the system consists of a cracked metal sheet bonded to a composite sheet with an elliptical debond between the sheets. The system was subjected to a remote stress, s. A rigorous stress analysis of this system requires a three-dimensional formulation. Although a general, exact solution is not available, finite element or finite difference numerical methods

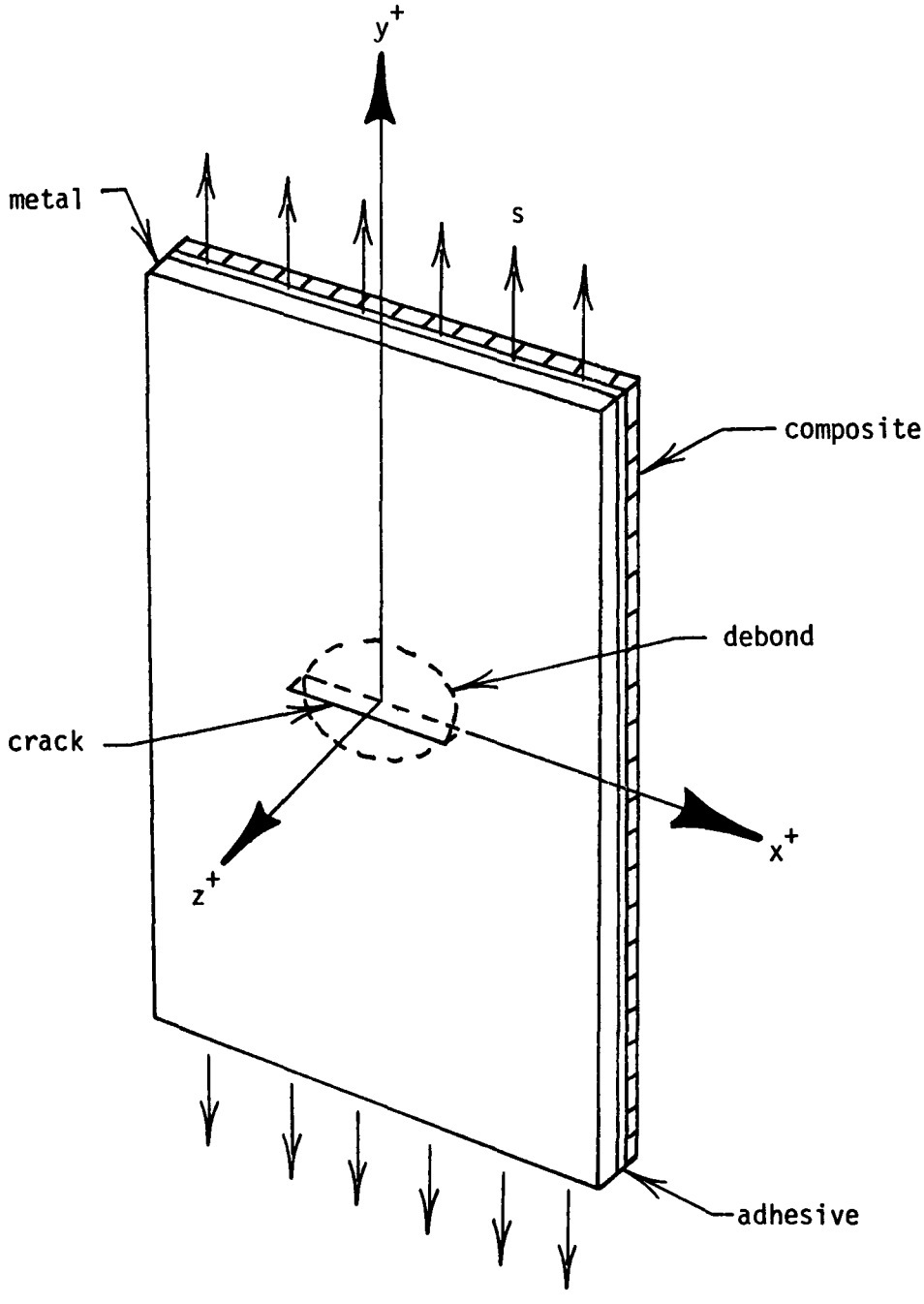

Fig. 6. System to be analyzed

can be employed to obtain a tractable solution. However, these solutions are not efficient for analyzing reinforced systems in which the crack length and debond area are continually changing. An alternate, simple analysis can be developed by assuming that the adherends are in plane stress while the adhesive is in pure shear. These assumptions were first used in an analysis by Volkerson in 1934.

The validity of these assumptions for analysis of the reinforced system shown in figure 6 was investigated in detail in Appendix B. As shown in Appendix B with a simple example, the assumption can lead to errors as much as 100 percent in the calculated adhesive stresses as compared to more rigorous finite element solutions. Evidently, significant shearing deformation occurs in the adherends of the reinforced system. The presence of the adherend shearing deformation violates Volkerson's assumptions, but as shown in Appendix B an effective shear modulus, G_{eff}, can be determined and used with the assumptions to calculate adhesive shearing stresses within a few percent of the finite element results.

Arin and Erodogan (1972) used Volkerson's assumptions with complex variable elasticity theory developed by Muskhelishvili (1953) and Lekhnitski (1956) to analyze a system similar to that shown in figure 6. The linear elastic stress analysis developed herein basically follows the concepts used by Arin and Erodogan, but differs in the formulation of the Green's functions used in the elasticity solution, the method of numerical integration of the Green's functions, and the domain of integration. To develop the stress analysis, the reinforced system is free bodied as shown in figure 7 (adhesive layer not shown)

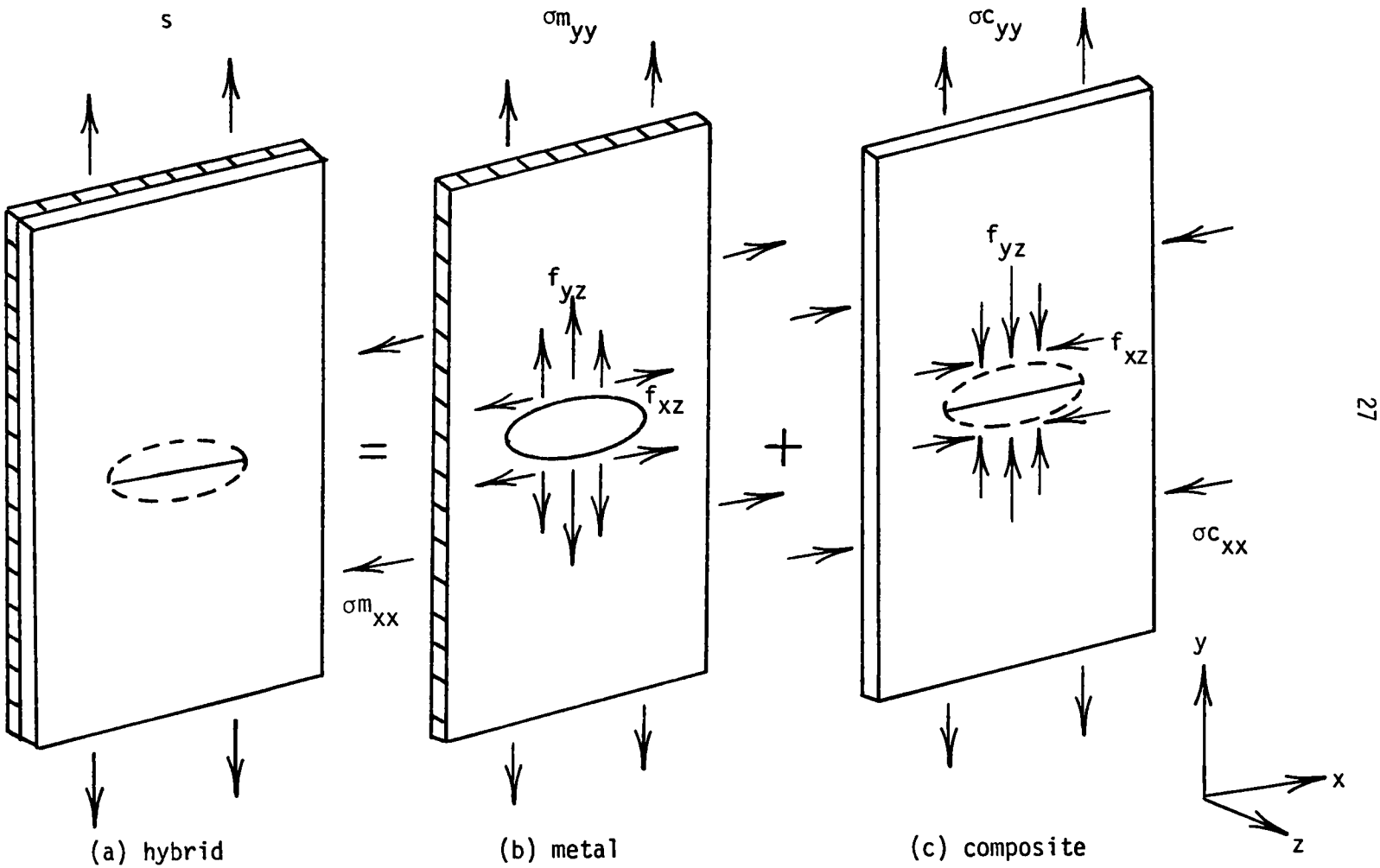

Fig. 7. Inplane and interlaminar stresses in the reinforced system

using Volkerson's assumptions. In the figure the remote stress, s, refers to the applied load over the total cross sectional area of the reinforced system. By the use of laminate theory as described in Appendix C, the inplane stresses σ_{ym}, σ_{yc}, σ_{xm}, and σ_{xc} (where the first subscript refers to stress direction and the second subscript refers to the metal or composite adherend) can be easily calculated. On figure 7, f_{yz} and f_{xz} indicate shear stresses in the adhesive layer. Throughout this dissertation the adhesive shear stresses which will be assumed to act as body forces on the adherends will be frequently called interlaminar stresses. To form a governing equation, these interlaminar stresses were related to the displacement of the adherends in the following manner.

First, the shear strain in the adhesive layer was related to the displacement in the adherends by the relations

$$\gamma_{xz} = \frac{u_m - u_c}{t_{ad}} \quad , \qquad \gamma_{yz} = \frac{v_m - v_c}{t_{ad}} \tag{6}$$

where t_{ad} is the thickness of the adhesive, u and v refer to displacements in the x and y direction respectively, and the subscripts m and c refer to the metal and composite adherends respectively. Next, Hook's law was used to relate the shearing strain in the adhesive to the interlaminar stresses as

$$\tau = G\gamma \tag{7}$$

Then, by the use of the effective shear modulus and equations (6) and (7) the interlaminar stresses can be related to the adherend displacements as

$$f_{xz} = \frac{G_{eff}}{t_{ad}} \{u_m - u_c\}, \qquad f_{zy} = \frac{G_{eff}}{t_{ad}} \{v_m - v_c\} \tag{8}$$

Equation (8) can be written for several different points in the reinforced system to form a system of simultaneous equations. These simultaneous equations are developed in detail in subsequent sections of this chapter.

The displacements, u and v, in the adherends were related to the inplane adherend stresses and the interlaminar stresses by several functions F_1 - F_8 as

$$\begin{aligned} u_m &= F_1(\sigma m_{xx}, \sigma m_{yy}) + F_5(f_{xz}, f_{yz}) \\ v_m &= F_2(\sigma m_{xx}, \sigma m_{yy}) + F_6(f_{xz}, f_{yz}) \\ u_c &= F_3(\sigma c_{xx}, \sigma c_{yy}) + F_7(f_{xz}, f_{yz}) \\ v_c &= F_4(\sigma c_{xx}, \sigma c_{yy}) + F_8(f_{xz}, f_{yz}) \end{aligned} \tag{9}$$

The displacements, F_1 and F_2, in the metal adherend due to the remote stress were calculated in terms of two stress functions $\phi(z)$ and $\omega(z)$ (Muskhelishvili 1975) by the equation

$$2G(u_m + iv_m) = \eta\phi(z) - \omega(\bar{z}) - (z - \bar{z})\overline{\Phi(z)} \tag{10}$$

where $\eta = \dfrac{3 - \nu}{1 + \nu}$ for plane stress, $i = \sqrt{-1}$, $z = x + iy$, the bar over a function or variable denotes the complex conjugate, ν is Poisson's ratio and

$$\phi(z) = \frac{\sigma m_{yy}}{2}\sqrt{z^2 - a^2} - \frac{z}{2}\left\{\frac{\sigma m_{yy}}{2} - \frac{\sigma m_{xx}}{2}\right\} \tag{11}$$

$$\omega(z) = \frac{\sigma m_{yy}}{2}\sqrt{z^2 - a^2} + \frac{z}{2}\left\{\frac{\sigma m_{yy}}{2} - \frac{\sigma m_{xx}}{2}\right\} \tag{12}$$

$$\Phi(z) = \frac{d\phi(z)}{dz} = \frac{\sigma m_{yy}}{2}\left\{\frac{z}{\sqrt{z^2 - a^2}}\right\} - \frac{1}{2}\left\{\frac{\sigma m_{yy}}{2} - \frac{\sigma m_{xx}}{2}\right\} \tag{13}$$

In equations (11) through (13) "a" denotes half the crack length in the metal sheet. With the use of equation (10), the functions F_1 and F_2 were found to be

$$F_1(\sigma m_{xx},\sigma m_{yy}) = \text{Real}\left\{\frac{\eta\phi(z) - \omega(z) - (z - \bar{z})\overline{\Phi(z)}}{2G}\right\}$$

$$F_2(\sigma m_{xx},\sigma m_{yy}) = \text{Img}\left\{\frac{\eta\phi(z) - \omega(z) - (z - \bar{z})\overline{\Phi(z)}}{2G}\right\} \qquad (14)$$

The displacements, F_3 and F_4, in the composite sheet due to the remote stress were found as follows. First, the constitutive equations for an orthotropic material were used to relate strainsto stresses (Lekhnitskii 1968) as

$$\varepsilon_x = \frac{\sigma c_{xx}}{E_x} - \frac{\nu_{yx}}{E_y}\sigma c_{yy}, \quad \varepsilon_y = -\frac{\nu_{xy}}{E_x}\sigma c_{xx} + \frac{\sigma}{E_y}\sigma c_{yy} \qquad (15)$$

where E_x and E_y are the moduli of elasticity in the x and y directions respectively, and ν_{xy} and ν_{yx} are Poisson's ratios. Then with the definition of strains as $\varepsilon_x = \frac{\partial u}{\partial x}$ and $\varepsilon_y = \frac{\partial v}{\partial y}$

equations (15) were integrated to find displacements as

$$u = F_3(\sigma c_{xx},\sigma c_{yy}) = \left\{\frac{\sigma c_{xx}}{E_x} - \frac{\nu_{yx}}{E_y}\sigma c_{yy}\right\} x + h1(y)$$

$$v = F_4(\sigma c_{xx},\sigma c_{yy}) = \left\{-\frac{\nu_{xy}}{E_x}\sigma c_{xx} + \frac{\sigma c_{yy}}{E_y}\right\} y + h2(x) \qquad (16)$$

where $h1(y)$ and $h2(x)$ are arbitrary functions which were set to zero because of symmetry considerations.

The displacements, F_5 and F_6, in the metal adherend caused by the interlaminar stresses were calculated by assuming that the interlaminar stresses acted as body forces on the adherends. With this assumption, the displacements were calculated using Green's functions in surface integrals as

$$F_1(f_{xz},f_{yz}) = aa_{xx} + aa_{xy}$$
$$F_2(f_{xz},f_{yz}) = aa_{yx} + aa_{yy} \tag{17}$$

where

$$aa_{xx} = \iint_S GD_{xx}(z,z_o)[-f_{xz}(z_o)]dx_o dy_o$$
$$aa_{xy} = \iint_S GD_{xy}(z,z_o)[-f_{yz}(z_o)]dx_o dy_o$$
$$aa_{yx} = \iint_S GD_{yx}(z,z_o)[-f_{xz}(z_o)]dx_o dy_o \tag{18}$$
$$aa_{yy} = \iint_S GD_{yy}(z,z_o)[-f_{yz}(z_o)]dx_o dy_o$$

and z_o is the location of a point load (see Appendix D) and GD_{xx}, GD_{xy}, GD_{yx}, and GD_{yy} are the Green's functions which were discussed and derived in Appendix D and found as

$$GD_{xx} = c_0\{\text{Real}(g(z,z_0) + g(z,\bar{z}_0))\}$$

$$GD_{xy} = c_0\{\text{Real}(\imath\{g(z,z_0) - g(z,\bar{z}_0)\})\}$$

$$GD_{yx} = c_0\{\text{Img}(g(z,z_0) + g(z,\bar{z}_0))\} \qquad (19)$$

$$GD_{yy} = c_0\{\text{Img}(\imath(g(z,z_0) - g(z,\bar{z}_0))\}$$

where

$$g(z,z_0) = \eta[\text{Real}\{XA(z,z_0)\} - XC(z,z_0)]$$

$$+ 0.5[\eta^2 XB(z,\bar{z}_0) + \overline{XB(z,\bar{z}_0)}] + XC(\bar{z},z_0)$$

$$+ 2\,\frac{zz_0 - \bar{z}_0\bar{z}}{\bar{z} - z_0} + (z - \bar{z})B(\bar{z},z_0)$$

with

$$XA(z,z_0) = -\,\text{Log}\left\{-\,\frac{zz_0 - a^2 - I(z_0)I(z)}{zz_0 + a^2 - I(z_0)I(z)}\right\}$$

$$XB(z,z_0) = \text{Log}\left\{\frac{zz_0 - a^2 - I(z_0)I(z)}{zz_0 + a^2 - I(z_0)I(z)}\left[\frac{z + z_0}{z_0 - z}\right]^2\right\}$$

$$XC(z,z_0) = \frac{z_0 - \bar{z}_0}{z^2 - z_0^2}\left\{z - z_0\,\frac{I(z)}{I(\bar{z}_0)}\right\}$$

$$B(z,z_0) = \frac{1}{2}\left\{\frac{-4z_0}{z^2 - z_0} + \frac{2\eta\bar{z}_0}{z^2 - \bar{z}_0^2} + \frac{z - \bar{z}_0}{(z - z_0)^2} - \frac{z + \bar{z}_0}{(z + z_0)^2}\right\}$$

$$+ \frac{z_0 - \bar{z}_0}{2I(z_0)I(z)}\left\{\frac{a^2 - zz_0}{(z - z_0)^2} - \frac{a + zz_0}{(z + z_0)^2}\right\}$$

$$- \frac{z}{I(z)}\left\{\frac{I(z_0)}{z_0^2 - z^2} - \eta\frac{I(\bar{z}_0)}{\bar{z}_0^2 - z^2}\right\}$$

and

$$I(z) = \sqrt{z^2 - a^2} \qquad c_0 = \frac{1}{4Gt_m\pi(1 + \eta)}$$

The domain of integration used in equation (18) will be discussed in a later section.

The displacements, $F_7(f_{xz},f_{yz})$ and $F_8(f_{xz},f_{yz})$, in the composite adherend caused by the interlaminar stresses were found with an approach similar to that used for the metal adherend. The functions were written as

$$F_7(f_{xz},f_{yz}) = bb_{xx} + bb_{xy}$$

$$F_8(f_{xz},f_{yz}) = bb_{yx} + bb_{yy} \tag{20}$$

where

$$bb_{xx} = \iint HD_{xx}(z_k,w_k)f_{xz}(w_k)dx_o dy_o$$

$$bb_{xy} = \iint HD_{xy}(z_k,w_k)f_{yz}(w_k)dx_o dy_o$$

$$bb_{yx} = \iint HD_{yx}(z_k,w_k)f_{xz}(w_k)dx_o dy_o \tag{21}$$

$$bb_{yy} = \iint HD_{yy}(z_k,w_k)f_{yz}(w_k)dx_o dy_o$$

$$k = 1,2$$

and HD_{xx}, HD_{xy}, HD_{yx}, and HD_{yy} are the Green's functionsfor the composite adherend derived in Appendix D and found to be

$$HD_{xx} = 2Real\{p_1 C11g_1(z_1,w_1) + p_2 C21g_1(z_2,w_2)\}$$

$$HD_{xy} = 2Real\{i[p_1 C12g_2(z_1,w_1) + p_2 C22g_2(z_2,w_2)]\}$$

$$HD_{yx} = 2Real\{q_1 C11g_1(z_1,w_1) + q_2 C21g_1(z_2,w_2)\} \tag{22}$$

$$HD_{yy} = 2Real[i[q_1 C21g_2(z_1,w_1) + q_2 C22g_2(z_2,w_2)]]$$

$$z_1 = x + s_1 y, \quad z_2 = x + s_2 y, \quad w_1 = x_0 + s_1 y_0,$$

$$w_2 = x_0 + s_2 y_0$$

where s_1 and s_2 are complex numbers which are not complex conjugates of each other and are roots of the equation (Lekhnitskii 1968)

$$s^4 + \left\{ \frac{E_x}{G_{xy}} - 2\nu_{xy} \right\} s^2 + \frac{E_x}{E_y} = 0$$

and

$$C11 = \frac{s_1(s_2^2 \nu_{xy} + 1)}{4\pi t_c(s_1^2 - s_2^2)} \qquad C12 = \frac{s_2^2 + \nu_{xy}}{4\pi t_c(s_1^2 - s_2^2)}$$

$$C21 = \frac{s_1(s_2^2 \nu_{yx} + 1)}{4\pi t_c(s_1^2 - s_2^2)} \qquad C22 = -\frac{s^2 + \nu_{xy}}{4\pi t_c(s_1^2 - s_2^2)}$$

$$p_1 = \frac{1}{E_x}(s_1^2 - \nu_{xy}) \qquad p_2 = \frac{1}{E_x}(s_2^2 - \nu_{xy})$$

$$q_1 = \frac{1}{s_1 E_y}(1 - \nu_{yx} s_1^2) \qquad q_2 = \frac{1}{s_2 E_y}(1 - \nu_{yx} s_2^2)$$

Substituting equations (14), (16), (17), and (20) into equation (9) and that result into equation (8) yields the governing equation that was used to formulate a system of simultaneous equations.

Numerical Solution

To solve for the unknown stresses f_{xz} and f_{yz}, the domain of integration in equations (18) and (21) was separated into three regions as shown on figure 8. Region A on the figure represents the portion of the domain where debonding has occurred. In this region the interlaminar stresses are zero. Region B on the figure represents the portion of the domain where significant interlaminar stresses exist. As shown on the figure, this region is divided into smaller elements. Region C on the figure represents a portion of the domain where the interlaminar stresses are small and can be neglected. The size of each of these regions will be discussed further in Chapter VI where convergence of the system is investigated.

The next step in the formulation of the simultaneous equations was to assume that the interlaminar stresses were constant over each element of region B. With this assumption, the displacements caused by the interlaminar stresses, equations (17) and (20), were written as

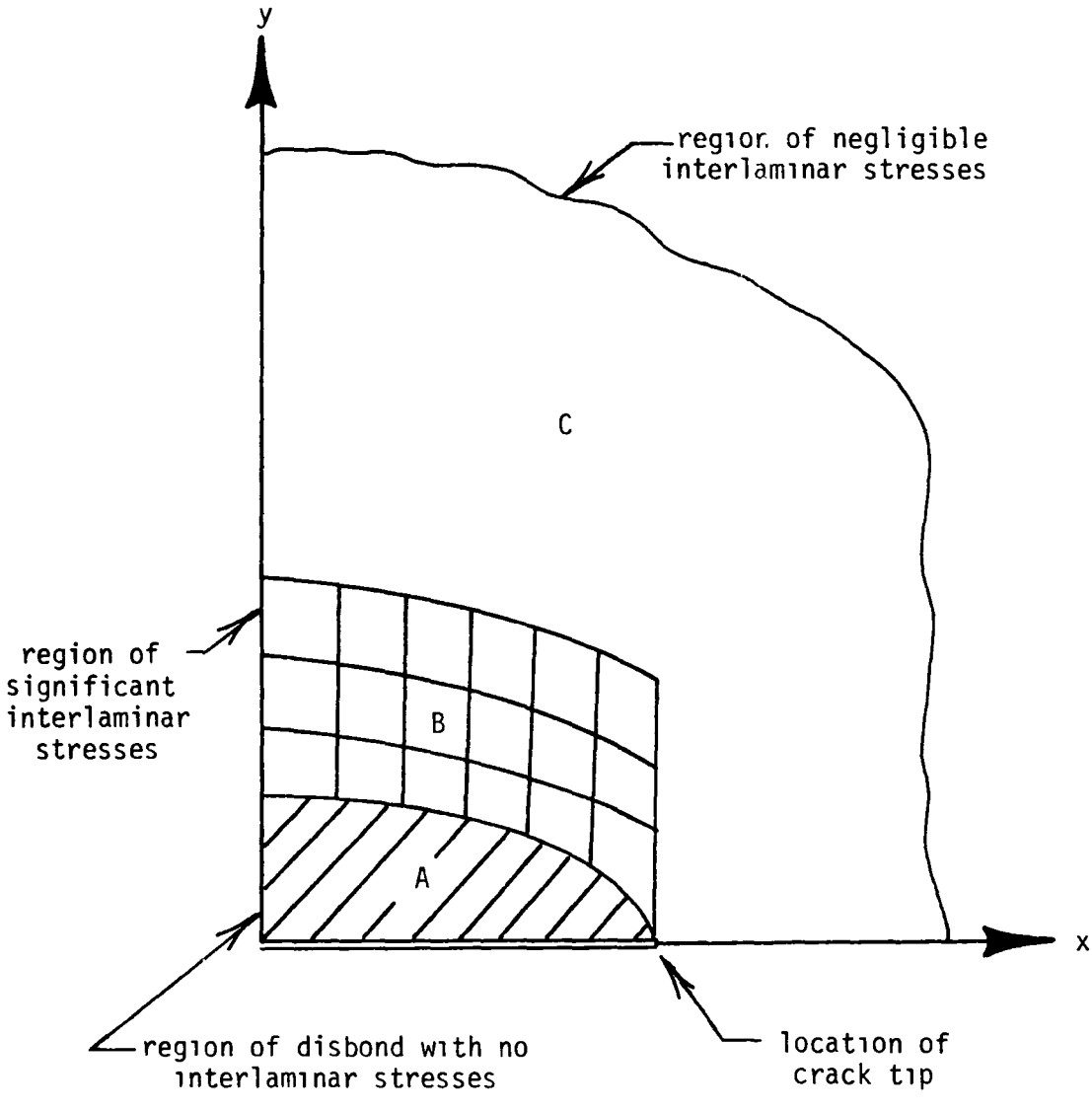

Fig. 8. Domain of integration

$$F_5(i) = \sum_{J=1}^{n} AA_{xx}(i,j)[-f_{xz}(j)] + AA_{xy}(i,j)[-f_{yz}(j)]$$

$$F_6(i) = \sum_{J=1}^{n} AA_{yx}(i,J)[-f_{yz}(j)] + AA_{yy}(i,J)[-f_{yz}(j)]$$

$$F_7(i) = \sum_{J=1}^{n} BB_{xy}(i,J)[-f_{xz}(J)] + BB_{xy}(i,J)[f_{yz}(j)] \qquad (23)$$

$$F_8(i) = \sum_{J=1}^{n} BB_{yx}(i,J)[f_{xz}(j)] + BB_{yy}(i,J)[f_{yz}(J)]$$

where n is the number of elements in region B and

$$AA_{xx}(i,j) = \iint GD_{xx}(z_i,z_o)dx_o dy_o$$

$$AA_{xy}(i,j) = \iint GD_{xy}(z_1,z_o)dx_o dy_o$$

$$AA_{yx}(i,j) = \iint GD_{yx}(z_1,z_o)dx_o dy_o$$

$$AA_{yy}(i,J) = \iint GD_{yy}(z_i,z_o)dx_o dy_o \qquad (24)$$

$$BB_{xx}(i,J) = \iint HD_{xx}(z_{k1},w_k)dx_o dy_o$$

$$BB_{xy}(i,J) = \iint HD_{xy}(z_{k1},w_k)dx_o dy_o$$

$$BB_{yx}(i,J) = \iint HD_{yx}(z_{ki},w_k)dx_o dy_o$$

$$BB_{yy}(i,j) = \iint HD_{yy}(z_{k1},w_k)dx_o dy_o \qquad k = 1,2$$

where the i subscript indicates the point in the x-y plane, z, where the governing equations (equations (8)) were evaluated. The j subscript when used in the coefficient of the interlaminar stresses, f_{xz} and f_{yz}, indicates the location of the centroid of the element over which the interlaminar stresses act while the j subscript used in the interlaminar stresses indicates the value of these stresses acting on element j. The integrals in equations (24) were evaluated numerically; the method of integration will be discussed in Chapter VI.

Substituting equation (14) and (23) in equations (9) and (8) and evaluating the result at the centroid of each element of region B lead to a system of 2n simultaneous linear equations where n is the number of elements in region B as

$$\begin{bmatrix} AA_{xx}(i,j) + BB_{xx}(i,j) & AA_{xy}(i,j) + BB_{xy}(i,j) \\ AA_{yx}(i,j) + BB_{yx}(i,j) & AA_{yy}(i,j) + BB_{yy}(i,j) \end{bmatrix} + \frac{t_{ad}}{G_{eff}} \begin{bmatrix} 1 & 0 \\ 0 & 1 \end{bmatrix} = \begin{bmatrix} F_1(i) - F_3(i) \\ F_2(i) - F_4(i) \end{bmatrix} \tag{25}$$

Using Gaussian elimination, this system of linear simultaneous equations was solved and yielded values of the unknown interlaminar stresses $f_{xz}(j)$ and $f_{yz}(j)$.

Nonlinear Solution

As shown in Appendix B, the adhesive used in the reinforced system can exhibit nonlinear stress strain behavior. As shown in the appendix, the tensile stress strain curve for the adhesive can be approximated by a bilinear stress strain curve with a change of slope occurring at about 4200 psi. Because the adhesive in the reinforced system is assumed to be in a state of pure shear, the data from the tensile stress strain curve must be related to the adhesive in a pure shear state. To develop this relationship, a yielding criterion is required.

For simplicity the criterion developed by Von Mises and given by Hill (1951) as

$$(\sigma_{xx} - \sigma_{yy})^2 + (\sigma_{yy} - \sigma_{zz})^2 + (\sigma_{zz} - \sigma_{xx})^2 + 6(\sigma^2_{yz} + \sigma^2_{zx} + \sigma^2_{xy}) = 6k_o^2 \tag{26}$$

where σ is the stress at yielding and k_o is a constant, was used to estimate when the adhesive in the reinforced system would exhibit nonlinear behavior.[5] For pure tension, as was the case in the bulk property test described in Appendix B, equation (26) reduces to

---

[5]Several yield criteria, of which Von Mises' is one of the most popular, are available in the literature.

$$2\sigma^2_{yy} = 6k_o^2 \tag{27}$$

For the adhesive in the reinforced system the only stresses present, according to the Volkerson assumptions, are σ_{yz} and σ_{xz}. Hence, in this case equation (26) reduces to

$$(\sigma^2_{yz} + \sigma^2_{xz}) = k_o^2 \tag{28}$$

Combining equations (27) and (28) by eliminating k_o yields a relation between tensile and shear yielding as

$$\sigma^2_{yz} + \sigma^2_{xz} = \sigma^2_{yy}/3 \tag{29}$$

For the bulk property tensile tests σ_{yy} was found approximately at 4200 psi. With this value in equation (29) and the notation for interlaminar stresses in the reinforced system an inequality was developed as

$$f^2_{yz} + f^2_{xz} \geq 5.88 \times 10^6 \tag{30}$$

Equation (30) was used to estimate the initiation of nonlinear behavior of the adhesive in the reinforced system by using f_{yz} and f_{xz} from the solution of equation (25). As will be shown in Chapter VII, equation (30) predicts that nonlinear behavior of the adhesive will occur in many reinforced systems. The adhesive nonlinearity manifests

itself in equation (25) as changes in G_{eff} with the magnitude of applied load. As shown in Appendix B, the G_{eff} for the adhesive can be either 65,000 psi or 36,000 psi. The value G_{eff} takes in the reinforced system can be determined from equation (30). If equation (30) is true then G_{eff} = 36,000 psi while if equation (30) is false G_{eff} = 65,000 psi.

By the use of inequality (30) and equation (25), the applied stress at which G_{eff} of the adhesive changes in the reinforced system was predicted with the following approach. As shown by equations (14) and (16) the right hand side of equation (25) is a function of the applied stress, s (σm_{xx}, σm_{yy}, σc_{xx}, σc_{yy} are linear functions of s). Hence, the solution of equation (25) was written in terms of the unit solution and the applied stress, s, as

$$f_{xz}(j) = s f_{xz}(j)_{unit}, \qquad f_{yz}(j) = s f_{yz}(j)_{unit} \tag{31}$$

where s is the remote applied stress and $f_{xz}(j)_{unit}$ and $f_{yz}(j)_{unit}$ are the solutions of equation (25) with an applied stress of s = 1. Substituting equations (31) into equation (30) and solving for s for each of the elements of region B, lead to values of the remote stress s(j) which cause a change in G_{eff} for element j as

$$s(j) = \sqrt{\frac{5.88 \times 10^6}{(f_{xz}(j)_{unit})^2 + (f_{yz}(j)_{unit})^2}} \tag{37}$$

The smallest value of $s(j)$ for n elements of region B is the value of the applied stress, $s^{(1)}$, which causes a change in G_{eff} in element k. At this value of $s^{(1)}$ all elements except element k have $G_{eff} = 65{,}000$, while element k has $G_{eff} = 36{,}000$.

If the value of $s^{(1)}$ is greater than the maximum remote applied stress, s_{max}, then the solution is completely elastic and from equation (31) the interlaminar stresses in the system are given as

$$f_{xz}(J) = s_{max} f_{xz}(J)_{unit}$$
$$f_{yz}(j) = s_{max} f_{yz}(j)_{unit} \tag{33}$$

However, if $s^{(1)}$ is less than s_{max} then yielding has occurred.[6] At the yield point the stress in all of the elements is given by

$$g_{xz}^{(1)}(J) = s^{(1)} f_{xz}(J)_{unit(1)}$$
$$g_{yz}^{(1)}(J) = s^{(1)} f_{yz}(j)_{unit(1)} \tag{34}$$

where the unit(1) indicates that the unit stresses were obtained from an elastic solution where all had the same shear modulus of $G_{eff} =$

---

[6] Yielding refers to a change in G_{eff} in the adhesive of the reinforced system.

65,000 psi. Once yielding has occurred in element k the shear modulus of element k takes on the secondary value $G_{eff} = 36{,}000$.

Consequently, for the next increment of applied stress the governing equations (25) must be modified as

$$\left[[A] + \frac{t_{ad}}{G_{eff}} \begin{bmatrix} 1 & & & 0 \\ & \ddots & & \\ & & 1 & \\ & & \frac{G_{eff}}{G2_{eff}} & \\ 0 & & & 1 \end{bmatrix} \right] \begin{bmatrix} f_{xz} \\ \\ f_{yz} \\ \\ \end{bmatrix} = \begin{bmatrix} F_{unit} \\ \\ \end{bmatrix} \qquad (35)$$

where

$$[A] = \begin{bmatrix} AA_{xx}(i,j) + BB_{xx}(i,j) & AA_{xy}(i,j) + BB_{xy}(i,j) \\ \\ AA_{yx}(i,j) + BB_{yx}(i,j) & AA_{yy}(i,j) + BB_{yy}(i,j) \end{bmatrix}$$

Equation (35) was then used to find a new unit solution after element k had yielded. The new unit values, $f_{xz}(j)_{unit(2)}$ and $f_{yz}(i)_{unit(2)}$, were then used in equation (31) and added to equations (34) to give the stress in each element after the second load increment as

$$\begin{aligned} f_{xz}(j) &= g_{xz}^{(1)}(j) + s^{(1)} f_{xz}(j)_{unit(2)} \\ f_{yz}(j) &= g_{yz}^{(1)}(j) + s^{(1)} f_{yz}(j)_{unit(2)} \end{aligned} \qquad (36)$$

Substituting equations (36) into equation (30) and solving for $s^{(2)}$ yields the value of $s^{(2)}$ that causesthe next element to yield as

$$s^{(2)} = \frac{-B_o + \sqrt{B_o^2 - 4A_oC_o}}{2A_o} \tag{37}$$

where

$$A_o = \left\{f_{xz}(J)_{unit(2)}\right\}^2 + \left\{f_{yz}(J)_{unit(2)}\right\}^2$$

$$B_o = 2\left\{g_{xz}^{(1)}(J)f_{xz}(j)_{unit(2)} + g_{yz}^{(1)}(J)f_{yz}(j)_{unit(2)}\right\}$$

$$C_o = \left\{g_{xz}^{(1)}(j)\right\}^2 + \left\{g_{yz}^{(1)}(j)\right\}^2 - \sigma^2{}_{yy}/3$$

If the value of $s^{(2)} > s_{max}$ then the stresses after the section increment of load are given by

$$g_{xz}^{(2)}(J) = (s_{max} - s^{(1)})\ f_{xz}(j)_{unit(2)} + g_{xz}^{(1)}(j)$$

$$g_{yz}^{(2)}(J) = (s_{max} - s^{(1)})\ f_{yz}(j)_{unit(2)} + g_{yz}^{(1)}(J) \tag{38}$$

and the total number of load increments is 2. But if $s^{(2)}$ is less than s_{max} then the stresses after the second load increment are given by

$$g_{xz}^{(2)}(j) = s^{(2)} f_{xz}(j)_{unit(2)} + g_{xz}^{(1)}(j)$$
$$g_{yz}^{(2)}(j) = s^{(2)} f_{yz}(j)_{unit(2)} + g_{yz}^{(1)}(j) \qquad (38)$$

The entire process is repeated until the sum of all the load increments equals s_{max}. The final value of the interlaminar stresses are the final values of $g_{xz}(j)$ and $g_{yz}(j)$ given as

$$f_{xz}(j) = g_{xz}^{(m)}(j)$$
$$f_{yz}(j) = g_{yz}^{(m)}(j) \qquad (40)$$

where m is the total number of load increments.

To obtain the final values for the interlaminar stresses, equation (40), the system of simultaneous equations (equations (35)) must be solved for each load increment. To minimize computational effort, a Gauss Siedel method discussed by McCracken and Dorn (1968) was used to solve equation (35) after the first unit vector was found by Gaussian elimination. By the use of unit vectors, $f_{xz}(j)_{unit(k)}$ and $f_{yz}(j)_{unit(k)}$, of the k iteration as initial estimates for the $k + 1$ unit vectors, the Gauss Siedel method rapidly converges. Consequently, the method is very efficient in solving for the unit stresses in successive load increments.

In this chapter an analysis was developed to determine interlaminar stresses in the reinforced system. In the next chapter these interlaminar stresses will be used to determine crack and debond growth rates in the reinforced system. The accuracy of the analysis will be discussed in Chapter VI.

CHAPTER V

FATIGUE ANALYSIS

As shown in Chapter II, fatigue damage in the reinforced system occurred as crack and debond growth. Accordingly, an adequate fatigue analysis should predict both types of growth. To the author's knowledge, the only analysis to date that attempts to model this behavior was developed by Ratwani (1977). Ratwani (1977) analyzes crack and debond growth in a cracked metal sheet reinforced with an uncracked metal sheet by using the elastic analysis developed by Erdogan and Arin (1972) and a maximum strain criterion to predict debond growth. In contrast, herein, the nonlinear elastic stress analysis developed in the previous chapter was coupled with a debond propagation equation based on calculated strain energy release rates.

Crack Growth Rate

To use the crack propagation equation (equation (4)), the stress intensity must be determined. The stress intensity can be related to the two stress distributions discussed in Chapter IV: the remote inplane stresses in the reinforced system and the interlaminar shear stresses which act near the debond front. The stress intensity can be found by superimposing the stress intensities from the two stress distributions.

The stress intensity produced by the remote stresses can be calculated by substituting the stress function, $\Phi(z)$, for this loading case (equation (13)) into equation (1) which related the stress function to the stress intensity as

$$k_1 - ik_2 = 2\sqrt{2} \lim_{z \to a} \left\{ \sqrt{z - a} \left\{ \frac{\sigma m_{yy}}{2} \frac{z}{z^2 - a^2} \right\} - \frac{1}{2} \left\{ \frac{\sigma m_{yy}}{2} - \frac{\sigma m_{xx}}{2} \right\} \right\} \tag{41}$$

which results in

$$k_1 = \sigma m_{yy} \sqrt{a}$$

$$k_2 = 0 \tag{42}$$

The stress intensity produced by the interlaminar shearing stresses, $f_{xz}(j)$ and $f_{yz}(j)$, was found in the following manner. First, the stress intensity for four point loads acting on a cracked sheet was found by substituting the stress function

$$\Phi(z,z_0) = SB(z,z_0) + \overline{SB}(z,\bar{z}_0) \tag{D.43}$$

derived in Appendix D into equation (1) to yield

$$k_1 - ik_2 = 2\sqrt{2} \lim_{z \to a} \left\{ \sqrt{z - a} \left[SB(z,z_0) + \overline{SB}(z,\overline{z}_0) \right] \right\} \qquad (43)$$

Taking the limit of equation (43) and combining coefficients of the X and Y load components results in

$$k_1 - ik_2 = X[XK(z_0) + XK(\overline{z}_0)]$$

$$+ iY[XK(z_0) - XK(\overline{z}_0)]$$

which leads to

$$k_1 = 2\text{Real}[XK(z_0)]X - 2\text{Img}[XK(z_0)]Y$$

$$k_2 = 0 \qquad (44)$$

where

$$XK(z_0) = \frac{\sqrt{a}}{\pi(1+\eta)t_m} \left\{ \frac{z_0\overline{z}_0 - zz_0^2 + a^2}{(z_0^2 - a^2)I(z_0)} + \frac{\eta I(\overline{z}_0)}{\overline{z}_0^2 - a^2} \right\} \qquad (45)$$

Then, with the use of the coefficient of the X and Y load components as Green's functions for the stress intensities, the stress

intensity caused by the interlaminar stress, $f_{xz}(j)$ and $f_{yz}(j)$, can be found as

$$k_1 = 2 \sum_{i=1}^{n} [f_{xz}(j) \iint \text{Real } XK(z_o)\, dx_o dy_o + f_{yz}(j) \iint \text{Img}(XK(\bar{z}_o) dx_o dy_o] \tag{46}$$

The domain of integration for equation (46) is, of course, the same as was discussed in the previous chapter. The method of integration will be discussed in the next chapter.

Debond Growth Rate

To use the debond propagation equation (equation (5)), the strain energy release rate must be determined for points along the debond front. A rigorous determination of the strain energy release rate is difficult and beyond the scope of this effort. However, an approximate solution is developed in the following paragraphs.

A freebody of a strip was taken from the longitudinal centerline of the reinforced system as shown in figure 9. The strain energy release rate for the strip was approximately calculated with the J integral developed by Rice and given in Liebowitz (1968) as

$$G = J = \int_\Gamma \left(\frac{1}{2}\ \sigma_{ij}\varepsilon_{ij} dz - t_i \frac{\partial u_1}{\partial y}\, ds\right) \tag{47}$$

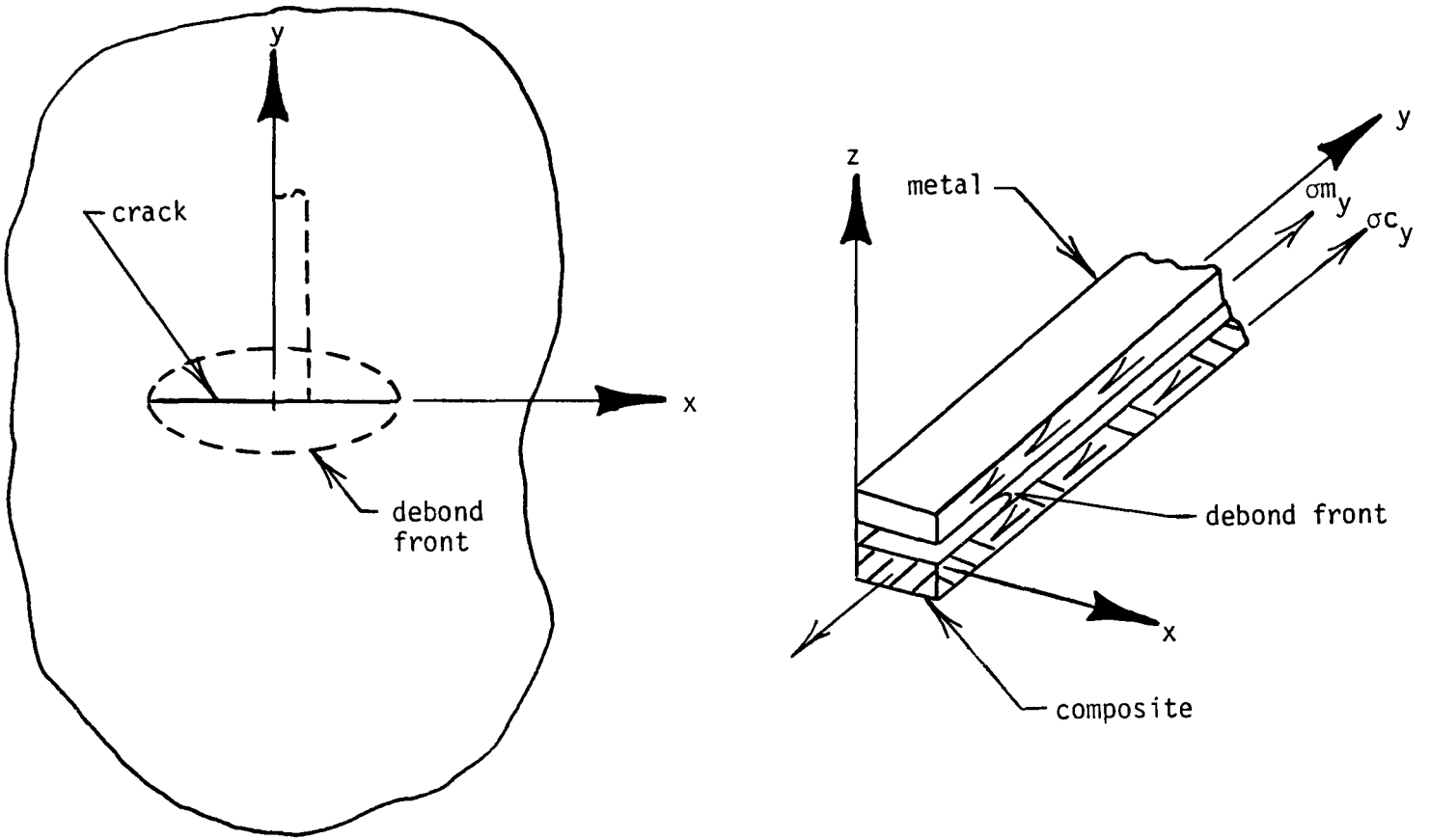

Fig. 9. Freebody for determination of G along debond front

where σ_{ij} is the stress, ε_{ij} is the strain, T_i is the surface traction, u_i is the displacement and Γ is any contour that contains the debond front and does not pass through a plastic region of material. Equation (47) can be written in terms of cartesian coordinates as (Yoder and Griffis 1974)

$$G = \int_{\Gamma} \left\{ W_e - \sigma_{yy} \frac{\partial v}{\partial y} - \sigma_{yz} \frac{\partial w}{\partial y} \right\} dz + \left\{ \sigma_{yz} \frac{\partial v}{\partial y} + \sigma_{zz} \frac{\partial w}{\partial y} \right\} dy \tag{48}$$

where W_e is the strain energy density and v and w are displacements in y and z directions respectively.

To apply integral (47) to the freebody shown in figure 9, a path of integration shown in figure 10 was used to analyze the energy release rate. The path surrounds the debond front on which no stresses or traction act, follows the bond line in the metal adherend on which the interlaminar stresses act, crosses the adhesive which is assumed to have insigificant stresses, and follows the bond line in the composite adherend on which the interlaminar stresses act. The $\frac{\partial v_n}{\partial y}$ is the strain in the metal adherend, and the $\frac{\partial v_c}{\partial y}$ is the strain in the composite adherend. With the use of this contour, the value of G from equation (48) can be written in terms of the interlaminar stresses, f_{xz} and f_{yz}, and the strain in the adherends, ε_{my} and ε_{cy}, as

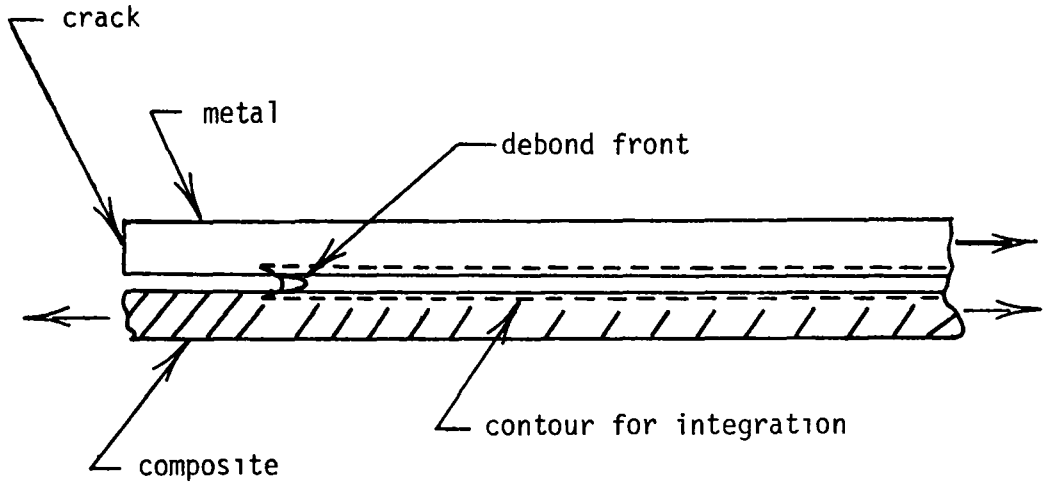

Fig. 10. Contour for determination of G for strip

$$G = \int f_{yz}(\varepsilon_{cy} - \varepsilon_{my})dy \tag{49}$$

With the use of discrete values of the interlaminar stresses and strains in the adherends, the strain energy release rate G can be approximated as

$$G = \sum_{i=1}^{p} t_y(i) f_{yz}(i)\{\varepsilon_{cy}(i) - \varepsilon_{my}(i)\} \tag{50}$$

where t_y represents the length of the discrete elements, i the index for the elements in the strip, and p the number of elements in the strip.

The interlaminar stresses, $f_{yz}(k)$, were determined from equation (40). However, the strains in the adherends still need to be determined. The strains in the adherends were determined from the stresses in the adherends according to laminate theory as shown in Appendix C as

$$\begin{bmatrix} \varepsilon_x \\ \varepsilon_y \\ \varepsilon_{xy} \end{bmatrix} = \begin{bmatrix} \quad \end{bmatrix}^{-1} \begin{bmatrix} \sigma_x \\ \sigma_y \\ \sigma_{xy} \end{bmatrix} \qquad \begin{bmatrix} \varepsilon_x \\ \varepsilon_y \\ \varepsilon_{xy} \end{bmatrix} = \begin{bmatrix} \quad \end{bmatrix}^{-1} \begin{bmatrix} \sigma_x \\ \sigma_y \\ \sigma_{xy} \end{bmatrix}$$

metal composite

(51)

where matrices C and D are given by equations (C.4) and (C.5) of Appendix C.

Before equation (51) was used to calculate the strain in the adherends, the stresses in the adherends were determined.

As shown by Muskelishvili (1975) the stresses in the metal adherend can be expressed in terms of two functions, $\Phi(z)$ and $\Omega(z)$, as

$$\sigma_x = \text{Real}\{3\Phi(z) - \Omega(\bar{z}) - (z - \bar{z})\overline{\Phi'(z)}\} \tag{52}$$

$$\sigma_y = \text{Real}\{\Phi(z) + \Omega(\bar{z}) + (z - \bar{z})\overline{\Phi'(z)}\} \tag{53}$$

$$\sigma_{xy} = \text{Imag}\{\Phi(z) + \Omega(\bar{z}) + (z - \bar{z})\overline{\Phi'(z)}\} \tag{54}$$

Equations (52) - (54) were used to determine the stresses in the metal adherends caused by both inplane remote stresses and interlaminar stresses.

For remote inplane stresses, $\Phi(z)$ is given by equation (13) as

$$\Phi(z) = \frac{\sigma m_{yy}}{2}\left\{\frac{z}{\sqrt{z^2 - a^2}}\right\} - \frac{1}{4}\,[\sigma m_{yy} - \sigma m_{xx}] \tag{13}$$

$\Phi'(z)$ was found by taking the derivative of $\Phi(z)$ as

$$\Phi'(z) = -\frac{\sigma m_{yy}}{2}\,\frac{a^2}{(z^2 - a^2)^{3/2}} \tag{55}$$

and $\Omega(z)$ was found by differentiating equation (12) as

$$\Omega(z) = \frac{\sigma m_{yy}}{2}\left\{\frac{z}{\sqrt{z^2 - a^2}}\right\} + \frac{1}{2}\left\{\frac{\sigma m_{yy}}{2} - \frac{\sigma m_{xx}}{2}\right\} \tag{56}$$

For the interlaminar stresses, $\Phi(z)$ and $\Psi(z)$ were determined and substituted in equations (52) - (54) (see Appendix D). The result, stress in the metal caused by interlaminar stresses, was found as

$$\sigma_x = -\sum_{j=1}^{n} \iint\{GS_{xx}f_{xz}(j) + GS_{xy}f_{yz}(j)\}dx_o dy_o \tag{57}$$

$$\sigma_y = -\sum_{j=1}^{n} \iint\{GS_{yx}f_{xz}(j) + GS_{yy}f_{yz}(j)\}dx_o dy_o \tag{58}$$

$$\sigma_{xy} = -\sum_{j=1}^{n} \iint\{GS_{(xy)x}f_{xz}(j) + GS_{(xy)y}f_{yz}(j)\}dx_o dy_o \tag{59}$$

where GS_{xx}, GS_{xy}, GS_{yx}, GS_{yy}, $GS_{(xy)x}$, and $GS_{(xy)y}$ are the Green's functions for stresses given in Appendix D by equations (D.68) through (D.73) respectively. The domain of integration in equations (57) - (59) is the area of an element shown in region B of figure 8 where j denotes the particular element.

Adding equations (52) - (52) and (57) - (59) yielded the stress in the metal adherend of the reinforced system. This result was then used in equation (51) to calculate the strain in the metal adherend.

The inplane stresses in the orthotropic adherend caused by the remote stresses were calculated with simple laminate theory as shown in Appendix C.

The inplane stresses in the orthotropic adherend caused by the interlaminar stresses were found in Appendix F as

$$\sigma_x = \sum_{j=1}^{n} \iint \{HS_{xx} f_{xz}(j) + HS_{xy} f_{yz}(j)\} dx_o dy_o \tag{60}$$

$$\sigma_y = \sum_{j=1}^{n} \iint \{HS_{yx} f_{xz}(j) + HS_{yy} f_{yz}(j)\} dx_o dy_o \tag{61}$$

$$\sigma_{xy} = \sum_{j=1}^{n} \iint \{HS_{(xy)x} f_{xz}(j) + HS_{(xy)y} f_{yz}(j)\} dx_o dy_o \tag{62}$$

where HS_{xx}, HS_{xy}, HS_{yx}, HS_{yy}, $HS_{(xy)x}$, and $HS_{(xy)y}$ are the Green's functions for an orthotropic solid sheet given in Appendix E by equations (E.23) - (E.28).

Adding the inplane stresses in the orthotropic adherend caused by the remote stresses and the interlaminar stresses and substituting the result into equation (51) yielded the strains in the orthotropic adherend.

With the strains in the adherends, equation (50) was used to calculate the strain energy release rate for the debond along the longitudinal axis of the reinforced system.

As indicated in Chapter III, the shape of the debond throughout the cyclic tests can be approximated by an ellipse. The equation for a general ellipse is given as

$$y = b[1 - (\frac{x}{a})^2]^{(\frac{1}{2})} \tag{63}$$

where a is half the crack length and b is the debond length measured along the y-axis from the center of the crack. With the use of equation (63) the overall debond shape was predicted by calculating the half crack length, a, from equation (4) using the stress intensity calculated from equation (45) and calculating the debond length, b, from equation (5) using the strain energy release rate calculated from equation (50).

Prediction of Crack and Debond Growth

The analysis developed in this dissertation was programmed on a CDC 6600 computer at NASA-LRC. A discussion of the program, a sample analysis, and a program listing are given in Appendix F. A flow chart of key elements of the program is shown in figure 11.

In the next chapter the accuracy of the analysis is investigated by comparing results of the calculations from the analysis with experimental results generated in Chapter III.

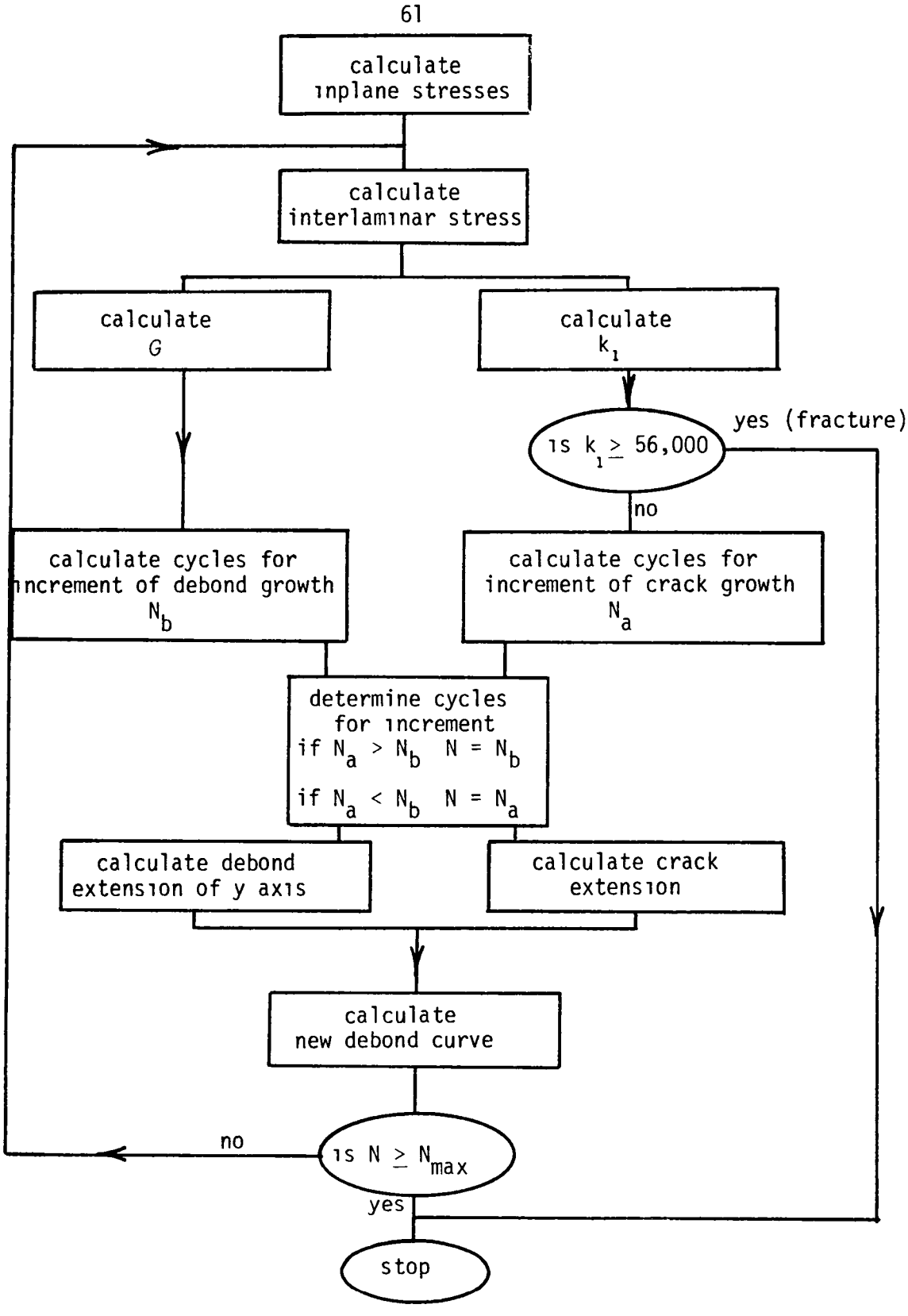

Fig. 11. Flow chart for fatigue analysis

CHAPTER VI

ASSESSMENT OF ACCURACY

Before the analysis developed in the previous chapters was used to study the fatigue behavior of the reinforced systems, the accuracy of the analysis was assessed. This assessment was based on analytical convergence studies and studies comparing analytical results with experimental results obtained in Chapter III.

Numerical Integration

A key item in the analysis was the method of integration of the Green's functions. In theory the Green's functions for both stress and displacement require integration over an infinite domain. Because the functions are complicated, a closed form integration is difficult if not impossible to perform. Consequently, a numerical solution was employed. Two key items in this numerical integration were the domain of integration and the method of numerical integration.

As shown on figure 8, the infinite domain of integration was divided into three regions: A, B, and C. Only region B has significant interlaminar shear stresses which need be integrated. To perform the integration region B was divided into elements as shown on figure 8. Each of these elements was bounded by the curves

$$x = x_1 \qquad x = x_2$$

$$y_1 = f_1(x) \quad y_2 = f_2(x) \tag{64}$$

where the functions f_1 and f_2 are the form of equation (63) and reflect the debond shape. For example, the bounding curves for elements along the debond front are given as

$$y_1(x) = b\left\{1 - \left[\frac{x}{a}\right]^2\right\}^{1/2}$$

$$y_2(x) = (b + db)\left\{1 - \left[\frac{x}{a + da}\right]^2\right\}^{1/2} \tag{65}$$

where a and b are the half crack length and the debond height respectively and da and db represent fractions of a and b.

The numerical method of integration used for each element of the region B was a two-dimensional Simpson's integration. Simpson's integration was used so that several of the Green's functions given by equations (19), (22), (D.68) - (D.73), and (E.23) - (E.28) could be integrated simultaniously by using common values of the complex functions. In each element the interlaminar stresses were assumed to be constant and the Green's functions were integrated by using 9 or 18 integration points. Nine integration points were used when the domain of integration did not contain a singularity while 18 points were used when a singularity existed within the element.

In the latter case the domain of the element was divided into three regions: two of which were analytic and the third, which contained the singularity, was nonanalytic. The two analytic regions were integrated with the nine point Simpson's integration scheme. The nonanalytic region was integrated by separating the Green's functions into products of analytic and nonanalytic functions. The analytical portions were expanded in a Taylor series and only the first terms, which were constants, were retained. The singular portion was integrated analytically in the principal value sense (Hilderbrand 1950). The product of the first term of the Taylor series and the principal value resulted in an approximate integral value in the nonanalytic region. In general the value of the integral in the nonanalytic region of the element was small in comparison with values in the two analytic regions.

The size of region B shown in figure 8 was determined iteratively by starting with a small region and increasing its size until no changes occurred in the interlaminar stresses, stress intensity or strain energy release rate. As an example, Panel B (under a load of 22,500 pounds) discussed in Chapter III was modeled as shown in figure 12 with an initial crack length of one inch and no debond (b = 0). As shown in the figure, region B was assumed to be nearly rectangular with n_x elements along the x-axis and n_y elements along the y-axis. The elements have a width of 0.25 inch and a height of 0.20 inch. The analysis was performed for values of n_x ranging from four to six and values of n_y ranging from one to six. Test conditions for each of these possible combinations were notated as

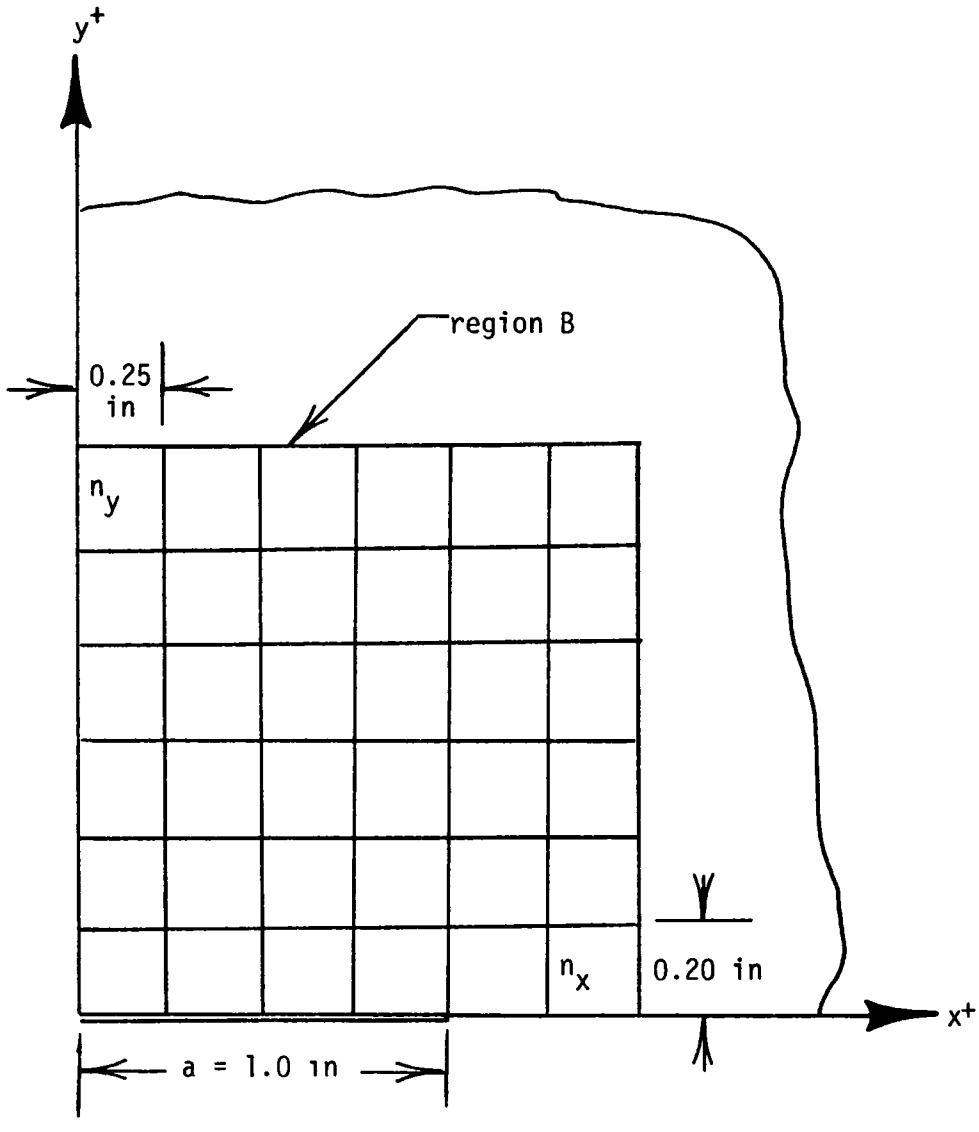

Fig. 12. Domain B for convergence analysis

n_y	n_x		
	4	5	6
	conditions		
1	1	7	13
2	2	8	14
3	3	9	15
4	4	10	16
5	5	11	17
6	6	12	18

Figure 13 shows the values of interlaminar stresses along the longitudinal centerline for the different conditions. As evident from the figure, values of the interlaminar stresses have converged for values of $n_x = 4$ and $n_y = 3$. Also both the stress intensities and the strain energy release rates have converged for these values. Thus, for this sample case the domain of region B is about 1 x 0.6 inch. Similar analyses showed that the length of the domain of region B along the x-axis is typically the length of the crack. However, as the adherend thickness or shear modulus of the adhesive changes, the extent of region B in the y-direction also changes.

With the use of the one-dimensional analysis discussed in Appendix B, the extent of region B in the y-direction was estimated for different adherend thicknesses and adhesive moduli in the following manner. A strip was taken from along the longitudinal centerline of the

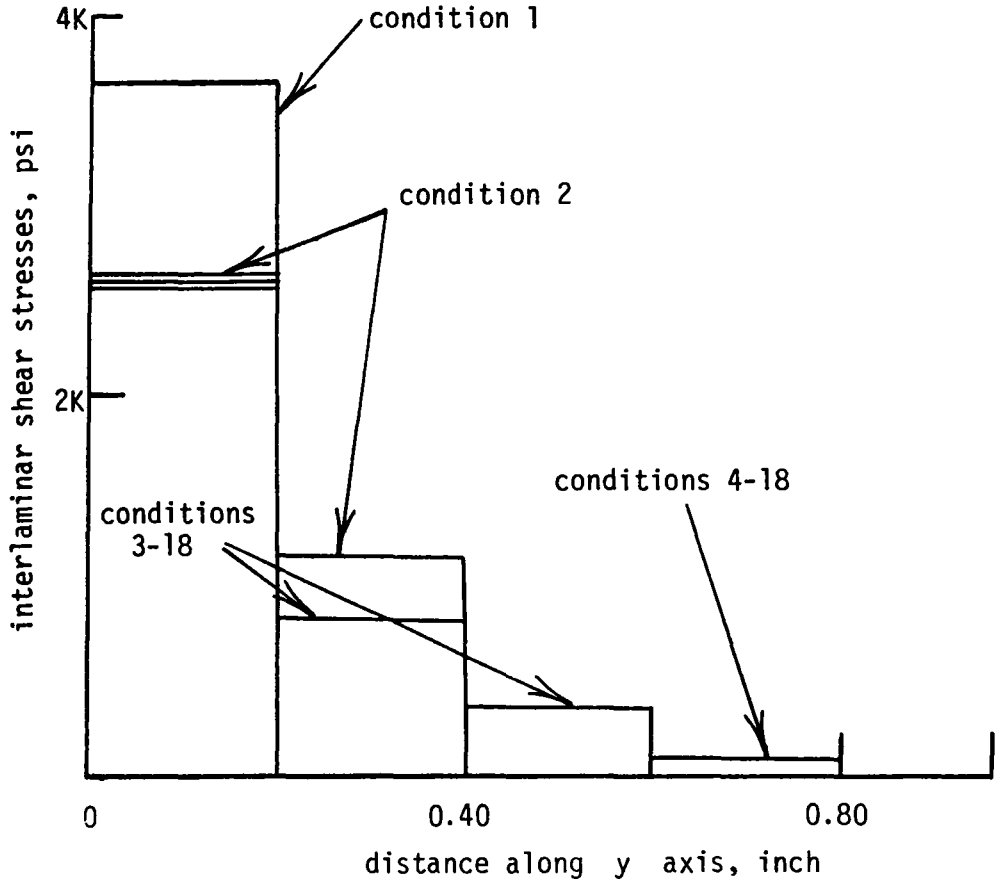

Fig. 13. Convergence of interlaminar shear stresses

reinforced system as shown in figure 9. Because of the crack the load in this strip must be transferred either to the adjacent metal via inplane shear stresses or to the composite via interlaminar stresses. If all the load were transferred via the interlaminar stresses, the interlaminar stresses could be higher and extend over a greater area than if the inplane stresses were considered. Consequently, the boundary of the interlaminar stress region calculated from the one-dimensional analysis, which only considers interlaminar stresses, would be an upper bound.

From the one-dimensional analysis the shearing stresses are found by equation (B-12) as

$$\tau(y) = K_o e^{-\sqrt{\alpha}y} \tag{B.12}$$

where

$$\alpha = \frac{G_{ad}}{t_{ad}} \left\{ \frac{1}{t_m E_m} + \frac{1}{t_c E_c} \right\} \qquad K_o = \frac{s\hat{\sigma}_{ad}}{t_{ad} E_2 \sqrt{\alpha}}$$

Examination of equation (B.12) revealed that the $\tau(y)$ is a maximum at $y = 0$. The shear stresses were assumed to be negligible when they were smaller than 5 percent of the maximum value. In equation form, the relationship between y and 95 percent of the maximum interlaminar shear stress was expressed as

$$0.05\ K_o = K_o e^{-\sqrt{\alpha}y}$$

Solving for y led to

$$y = -\frac{\ln(0.05)}{\sqrt{\alpha}} \tag{66}$$

the distance at which the shear stresses are 95 percent of their maximum value. As evident from equation (66) the y distance is a function of the thicknesses and material properties of the adherends and the adhesive. For the adhesive used in the reinforced system of Panels A and B two effective shear moduli were found as 65,000 psi prior to yielding and 26,100 psi after yielding (see Appendix B). With the use of the latter of these two values to give a conservative bounds, the y distance for region B of Panel B (see figure 2) as calculated by equation (66) was found as $y = 0.60$ in. The estimated value agrees well with convergence study results shown on figure 13. The same logic applies to both bonded ($b = 0$) and debonded systems ($b > 0$). Consequently, the domain of region B used in the integration of the Green's functions was determined by the crack length and equation (66).

Once the domain of region B was determined, the effect of mesh refinement within region B was investigated. Figure 14 shows a comparison of interlaminar stresses calculated (again for Panel B) using two different mesh sizes in region B. As evident from the figure,

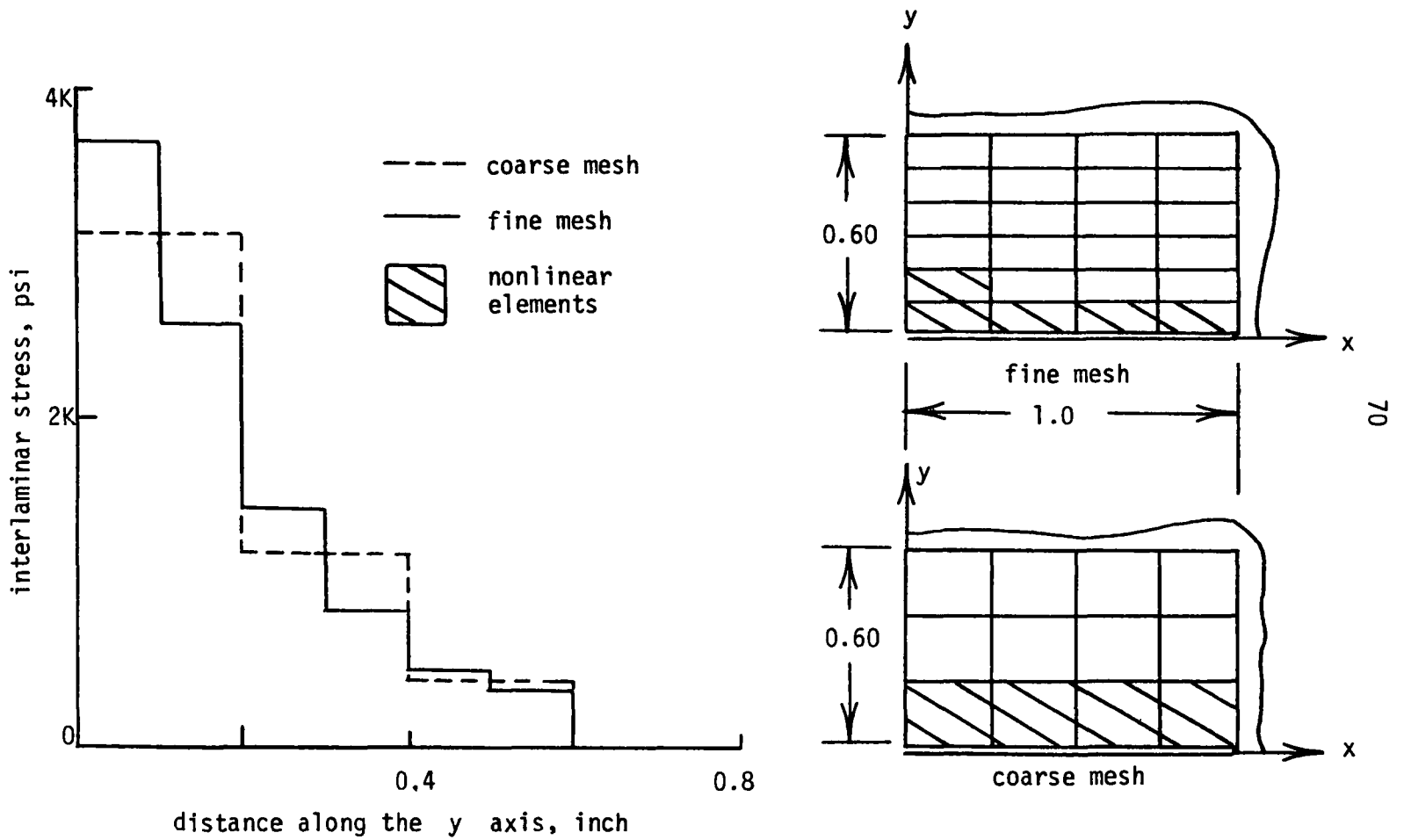

Fig. 14. The effect of mesh size on interlaminar stresses

the interlaminar stresses calculated with the fine mesh can deviate as much as 16 percent from stresses calculated with the coarse mesh. The stress intensities and strain energy release rates calculated using the two different meshes were found as

	k_1	G
coarse mesh	0.281	1.29
fine mesh	0.280	1.36

The values of k_1 and G are not nearly as sensitive to changes in mesh size as the interlaminar stresses were. The reason for the insensitivity is most likely because both k_1 and G are obtained by integration schemes that smooth out the effect of local approximations in the interlaminar stresses. Consequently, the grid can be rather coarse and still accurately predict both k_1 and G. In contrast the values of the interlaminar stresses require a finer mesh for accurate values. Because k_1 and G are used to predict the fatigue behavior of the reinforced system, a relatively coarse mesh was used in the analysis without loss of accuracy.

Accuracy of the Analysis

To ascertain the accuracy of the analysis, calculated values of stresses in the adherends, the stress intensities, and the crack propagation rates and debond sizes were compared to experimental results on Panels A and B shown in Chapter III. To compare calculated and experimental values of stresses in the adherends and stress

intensities, Panels A and B were modeled when the half crack length, a, reached 2 inches as shown on figure 15. The debond sizes were obtained from the C-scans of the specimens shown on figure 5. The height of the grid from the edge of the debond was determined from equation (66). The crosshatched elements on the figure indicate elements in which the adhesive has changed modulus (yielded) during each applied load cycle. The effect of the modulus change on k_1 and G will be discussed in the next chapter.

The values of the crack growth rate for Panels A and B were calculated for a half-crack length of 2 inches, the debond sizes observed in figure 5, and the applied loads shown on page 18. The calculated values and the experimental values, from Chapter II, of the crack propagation rates are

Panel	da/dN, in/cycle calculated	experimental
A	2.85×10^{-4}	1.30×10^{-4}
B	2.26×10^{-4}	3.12×10^{-4}

The difference between the calculated and experimental rates are within the scatter of the predicted rates for unreinforced metal sheets (Figge and Newman 1967). Hence, the analysis accurately predicts the crack growth rate if the crack length and debond are known.

As a further check, the analysis was used to predict the crack growth in Panels A and B. Figure 16 shows the calculated and

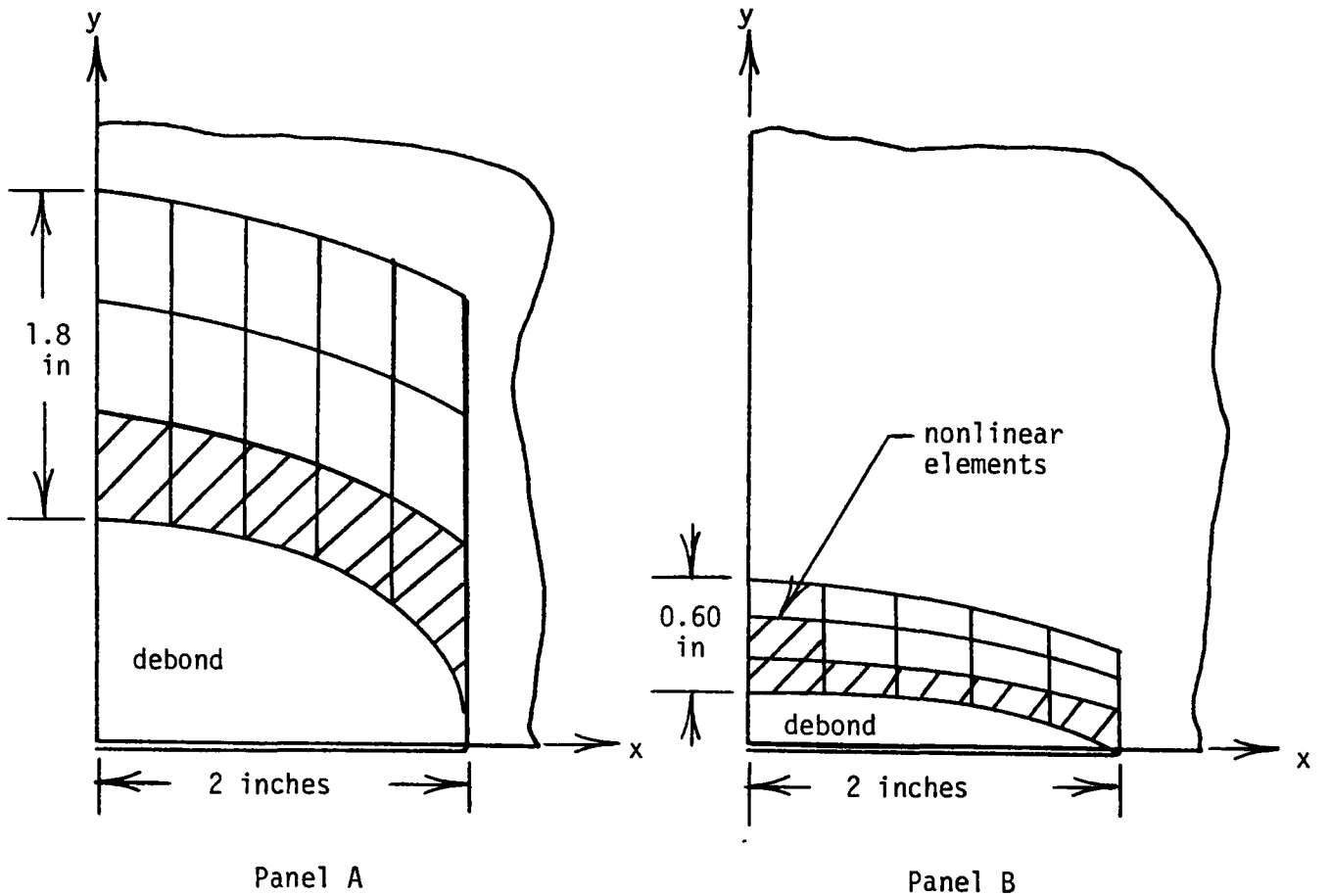

Fig. 15. Mesh for analysis of Panels A and B

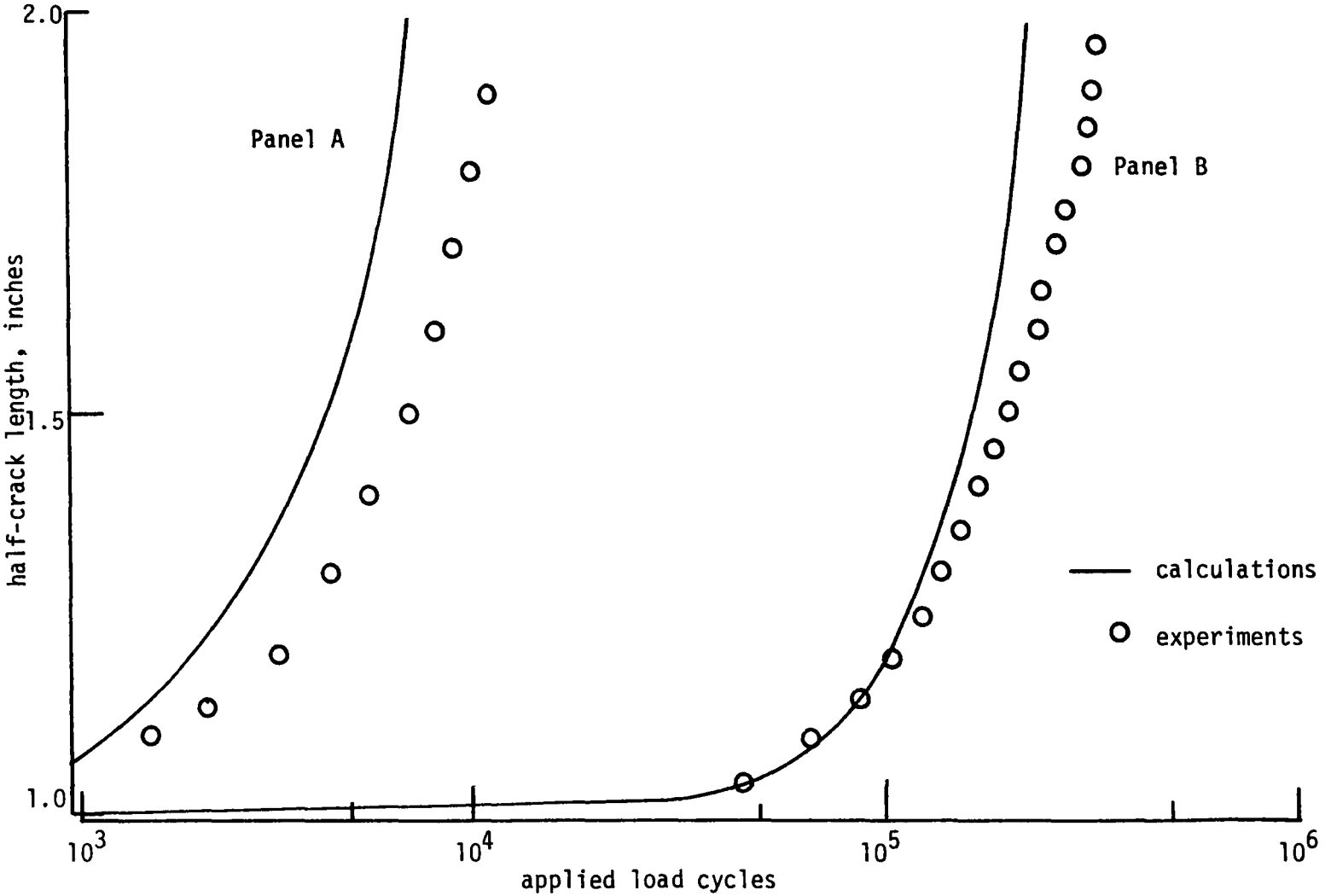

Fig. 16. Experimental and calculated crack lengths as a function of applied load cycles

experimental half-crack lengths plotted against the number of applied load cycles. For both panels the analysis gave a conservative prediction of the crack growth. The calculated and experimental half-crack lengths agree within a factor of 2. This deviation is within the scatter of crack length prediction of unreinforced metals. Hence, the analysis appears to accurately predict the crack length as a function of applied load cycles.

On figure 17 the calculated and experimental crack propagation rates were plotted against the half-crack length. The calculated crack propagation rates were within a factor of 2 of the experimental rates. The largest error occurred in Panel B for a half-crack length of 2 inches.

The calculated crack lengths and crack propagation rates shown on figures 16 and 17 are a function of debond growth. On figure 18 the debond aspect ratio, b/a, was plotted against the half-crack length for the two panels. The symbols on the figure indicate values of the debond aspect ratio obtained experimentally (see figure 10). As evident on the figure, the calculations indicated that the debond aspect ratio increases rapidly, especially for Panel A, before the half-crack length reaches 0.2 inch. Hence, the debond grows before the crack does.

Of the two panels, Panel A exhibits the largest debond growth, and at a half-crack length of 2 inches the predicted debond aspect ratio was determined experimentally. For Panel B, the analysis predicted a debond aspect ratio of 0.45 at a half-crack length of 2 inches. In contrast,

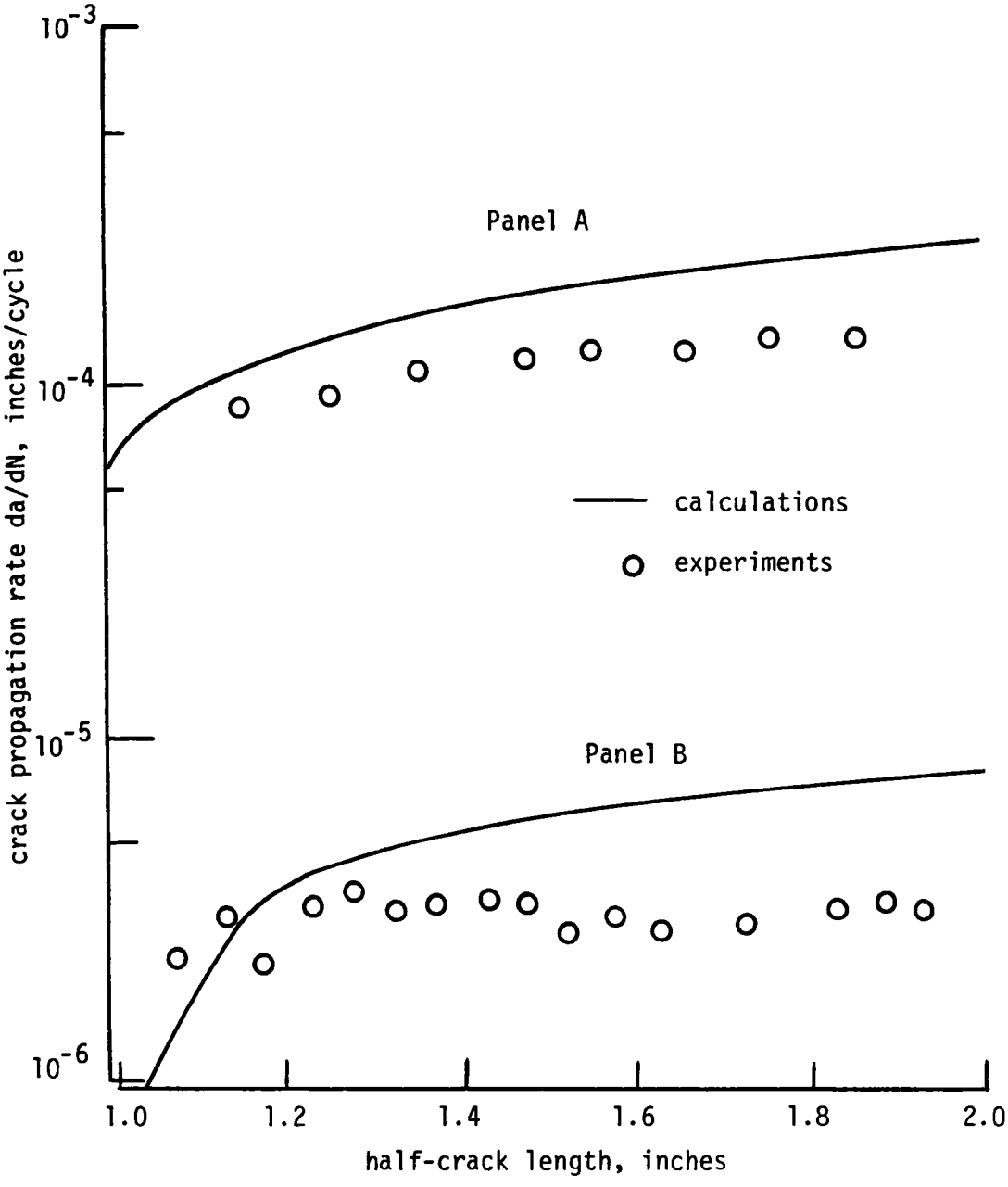

Fig. 17. Experimental and calculated crack propagation rates

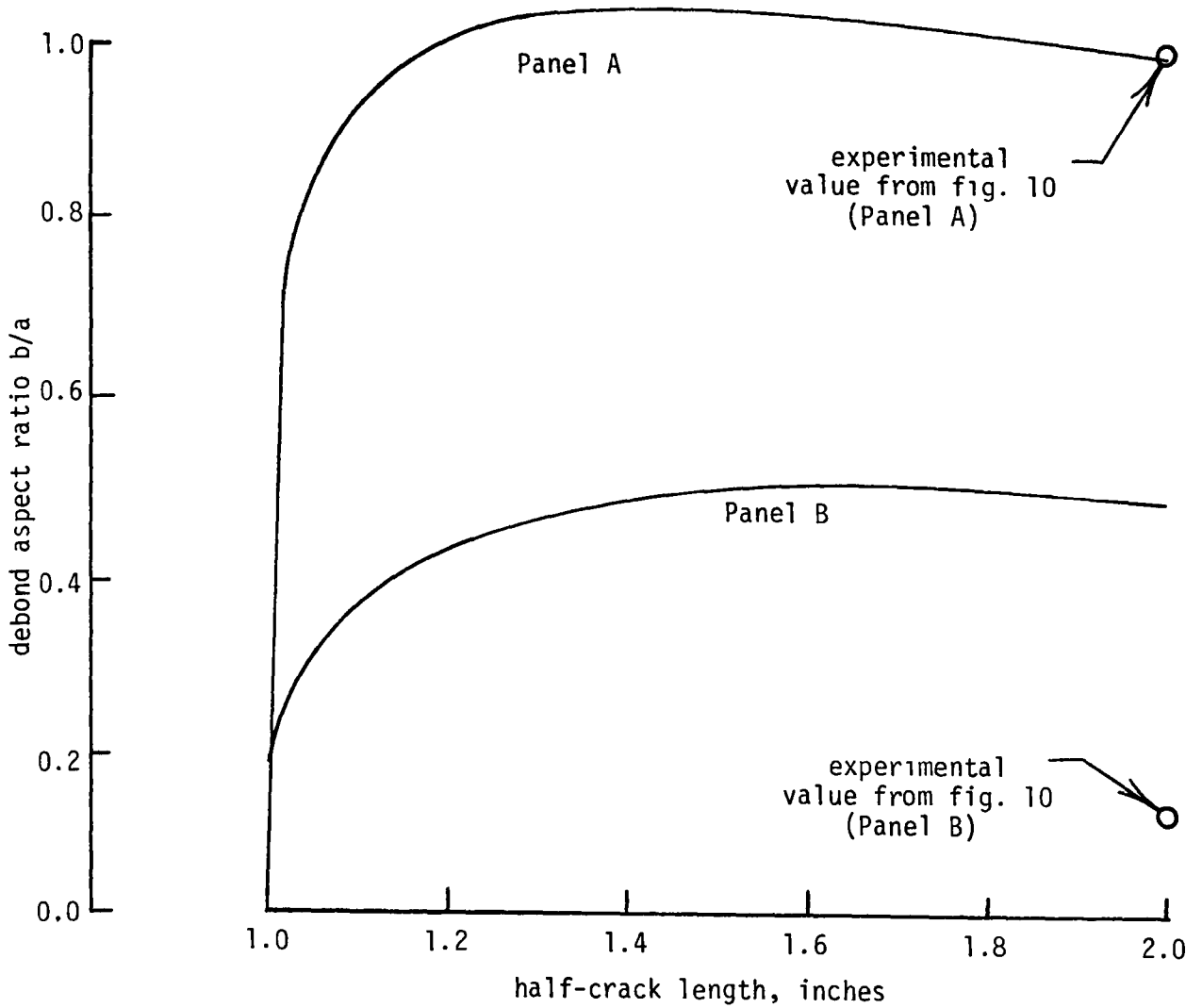

Fig. 18. Debond aspect ratio versus crack length

the debond aspect ratio obtained experimentally was about 0.14. The discrepancy between the calculated and experimental values may be linked to the magnitude of strain energy release rate as the debond propagates in Panel B. Values of G in Panel B ranged from 0.63 in-lbs/in at a half-crack length of 1 inch to 0.53 in-lb/in at a half-crack length of 2 inches (in contrast G values for Panel A ranged from 6.0 to 2.45 in-lbs/in). The values of G for Panel B were below values of G used to determine the empirical constants in equation (5). A few exploratory tests of the type performed in Appendix A revealed that a threshold value of G may exist. Below this threshold value debonding does not occur. Although proving the existence of a threshold was beyond the scope of this dissertation, if it does exist the analysis of Panel B would predict a debond aspect ratio much closer to the experimental value.

The comparison between calculated and experimental values of predicted crack length, crack propagation rate and debond aspect ratio shown on figures 16 through 18 showed that the analysis has potential to predict crack growth in metals reinforced with composite materials. However, a true assessment of the accuracy of the analysis can be made only after a more extensive data base is developed.

CHAPTER VII

PARAMETRIC STUDIES ON CRACK AND DEBOND GROWTH

To give insight about crack and debond growth in reinforced systems, the analysis was performed for reinforced systems with several different adherend thicknesses, debond sizes, and crack lengths. The metal adherend thicknesses studied were 0.05, 0.10, and 0.15 inch; the composite adherend thicknesses were 0.025, 0.05, and 0.075; the half-crack lengths were 0.5, 1.0, 1.5 inches; and the aspect ratios of the debond areas were 0.001, 0.5, and 1.0. For the various combinations of adherend thicknesses, crack lengths, and debond aspect ratios, the stress intensities, strain energy release rates, and remote stress that caused nonlinear behavior of the adhesive were calculated and are shown in Table 2.

The first two columns of the table give the metal and adherend thicknesses, t_m and t_c. The third and fourth columns give the half-crack length, a, and the debond aspect ratio, b/a. The fifth column gives the stress intensity in the metal adherend normalized by the remote stress, k/s. The sixth column gives the strain energy release rate at the debond front (along the longitudinal centerline) normalized by the remote stress squared, G/s^2. The last column gives the remote stress that would cause the adhesive layer in the reinforced system to behave nonlinearly.

TABLE 2

CALCULATED VALUES FOR PARAMETRIC STUDY

t_m (in)	t_c (in)	a (in)	b/a	k/s ($in^{\frac{1}{2}}$)	G/s^2 (in^4/lbs)	s_{yield} psi
0.050	0.025	0.50	0.001	0.171	12.4E-10	19,600
		0.50	0.50	0.240	8.2E-10	25,200
		0.50	1.00	0.289	4.4E-10	25,600
		1.00	0.001	0.170	12.6E-10	17,600
		1.00	0.50	0.286	9.5E-10	23,900
		1.00	1.00	0.366	4.9E-10	23,600
		1.50	0.001	0.171	12.4E-10	16,500
		1.50	0.50	0.322	9.6E-10	23,800
	0.025	1.50	1.00	0.426	5.1E-10	23,700
	0.050	0.50	0.001	0.138	7.3E-10	25,000
		0.50	0.50	0.190	5.6E-10	21,700
		0.50	1.00	0.230	3.0E-10	29,500
		1.00	0.001	0.136	7.2E-10	22,800
		1.00	0.50	0.221	6.0E-10	28,100
		1.00	1.00	0.286	3.3E-10	27,000
		1.50	0.001	0.137	7.2E-10	21,100
		1.50	0.50	0.264	6.0E-10	27,600
	0.050	1.50	1.00	0.329	3.3E-10	27,200
	0.075	0.50	0.001	0.125	5.7E-10	28,200
0.050	0.075	0.50	0.50	0.170	4.8E-10	33,800

TABLE 2-Continued

t_m (in)	t_c (in)	a (in)	b/a	k/s ($in^{\frac{1}{2}}$)	$G's^2$ (in^4/lbs)	s_{yield} psi
0.050	0.075	0.50	1.00	0.206	2.4E-10	31,900
		1.00	0.001	0.123	5.6E-10	26,500
		1.00	0.50	0.196	4.7E-10	30,600
		1.00	1.00	0.254	2.6E-10	29,100
		1.50	0.001	0.123	5 6E-10	23,800
		1.50	0.50	0.217	4.8E-10	30,000
0.050	0.075	1.50	1.00	0.291	2.7E-10	29,300
0.100	0.025	0.50	0.001	0.254	41.5E-10	11,200
		0.50	0.50	0.334	24.6E-10	15,700
		0.50	1.00	0.385	11.4E-10	17,600
		1.00	0.001	0.256	46.1E-10	9,800
		1.00	0.50	0.407	28.9E-10	14,200
		1.00	1.00	0.498	13.5E-10	15,400
		1.50	0.001	0.257	46.2E-10	9,100
		1.50	0.50	0.462	29.9E-10	13,700
	0.025	1.50	1.00	0.583	14.2E-10	15,100
	0.050	0.50	0.001	0.202	23.9E-10	14,600
		0.50	0.50	0.263	16.2E-10	18,900
		0.50	1.00	0.307	8.1E-10	19,900
		1.00	0.001	0.202	25.1E-10	13,100
0.100	0.050	1.00	0.50	0.309	18.5E-10	17,400

TABLE 2-Continued

t_m (in)	t_c (in)	a (in)	b/a	k/s ($in^{\frac{1}{2}}$)	G/s^2 (in^4/lbs)	s_{yield} psi
0.100	0.050	1.00	1.00	0.385	9.4E-10	12,379
		1.50	0.001	0.201	25.0E-10	16,800
		1.50	0.50	0.345	19.0E-10	16,800
	0.050	1.50	1.00	0.444	9.9E-10	16,700
	0.075	0.50	0.001	0.178	17.6E-10	16,900
		0.50	0.50	0.230	12.5E-10	21,300
		0.50	1.00	0.269	6.4E-10	21,800
		1.00	0.001	0.177	18.0E-10	15,200
		1.00	0.50	0.266	14.0E-10	19,400
		1.00	1.00	0.333	7.4E-10	18,500
		1.50	0.001	0.176	17.9E-10	14,600
		1.50	0.50	0.294	14.4E-10	18,600
0.100	0.075	1.50	1.00	0.382	7.4E-10	18,100
0.150	0.025	0.50	0.001	0.313	78.3E-10	8,300
		0.50	0.50	0.397	40.9E-10	12,400
		0.50	1.00	0.446	18.0E-10	14,800
		1.00	0.001	0.323	95.6E-10	7,000
		1.00	0.50	0.493	51.3E-10	10,900
		1.00	1.00	0.584	22.3E-10	12,500
		1.50	0.001	0.325	99.0E-10	6,500
		1.50	0.50	0.565	54.1E-10	10,400
0.150	0.025	1.50	1.00	0.689	23.7E-10	12,100

TABLE 2-Continued

t_m (in)	t_c (in)	a (in)	b/a	k/s ($in^{\frac{1}{2}}$)	G/s^2 (in^4/lbs)	s_{yield} psi
0.150	0.050	0.50	0.001	0.253	46.8E-10	10,600
		0.50	0.50	0.318	28.9E-10	14,400
		0.50	1.00	0.362	13.9E-10	16,200
		1.00	0.001	0.256	52.9E-10	9,400
		1.00	0.50	0.379	35.2E-10	12,900
		1.00	1.00	0.460	17.1E-10	13,400
		1.50	0.001	0.256	53.7E-10	8,700
		1.50	0.50	0.425	37.1E-10	12,400
0.150	0.050	1.50	1.00	0.534	18.2E-10	12,900
0.150	0.75	0.50	0.001	0.222	34.4E-10	12,300
		0.50	0.50	0.278	22.5E-10	16,100
		0.50	1.00	0.318	11.3E-10	17,600
		1.00	0.001	0.223	37.3E-10	11,100
		1.00	0.50	0.325	26.9E-10	14,500
		1.00	1.00	0.397	13.7E-10	14,400
		1.50	0.001	0.222	37.6E-10	10,300
		1.50	0.50	0.360	28.2E-10	14,000
0.150	0.75	1.50	1.00	0.457	14.5E-10	13,700

Stress Intensity Factor, Crack Growth Rate

Figures 19, 20, and 21 show the effects of composite adherend thickness, debond aspect ratio, and crack lengths on stress intensity for the different thickness metal adherends. On the figures circles, diamonds and squares represent stress intensity values for 0.025, 0.05, and 0.075 inch thick composite adherends respectively. Open, half-shaded, and shaded symbols represent stress intensity values for debond aspect ratios of 0.0, 0.50, and 1.0 respectively. On the figures the stress intensity normalized by the remote stress was plotted against the half-crack length.

For all three metal adherend thicknesses, the figures show consistent trends. If the debond aspect ratio is small, the stress intensity is not significantly affected by either the crack length or the thickness of the composite reinforcement. However, as the debond size increases, the stress intensities increase significantly with longer crack lengths and thinner composite reinforcement.

The effects of debond size, composite adherend thickness, and crack length become more pronounced for the thicker metal adherends.

Strain Energy Release Rate, Debond Propagation

Figures 22, 23, and 24 show the effect of composite adherend thickness, debond aspect ratio, and crack length on the strain energy release rate at the debond front (along the longitudinal centerline of the reinforced system). As on figures 19, 20, and 21, different

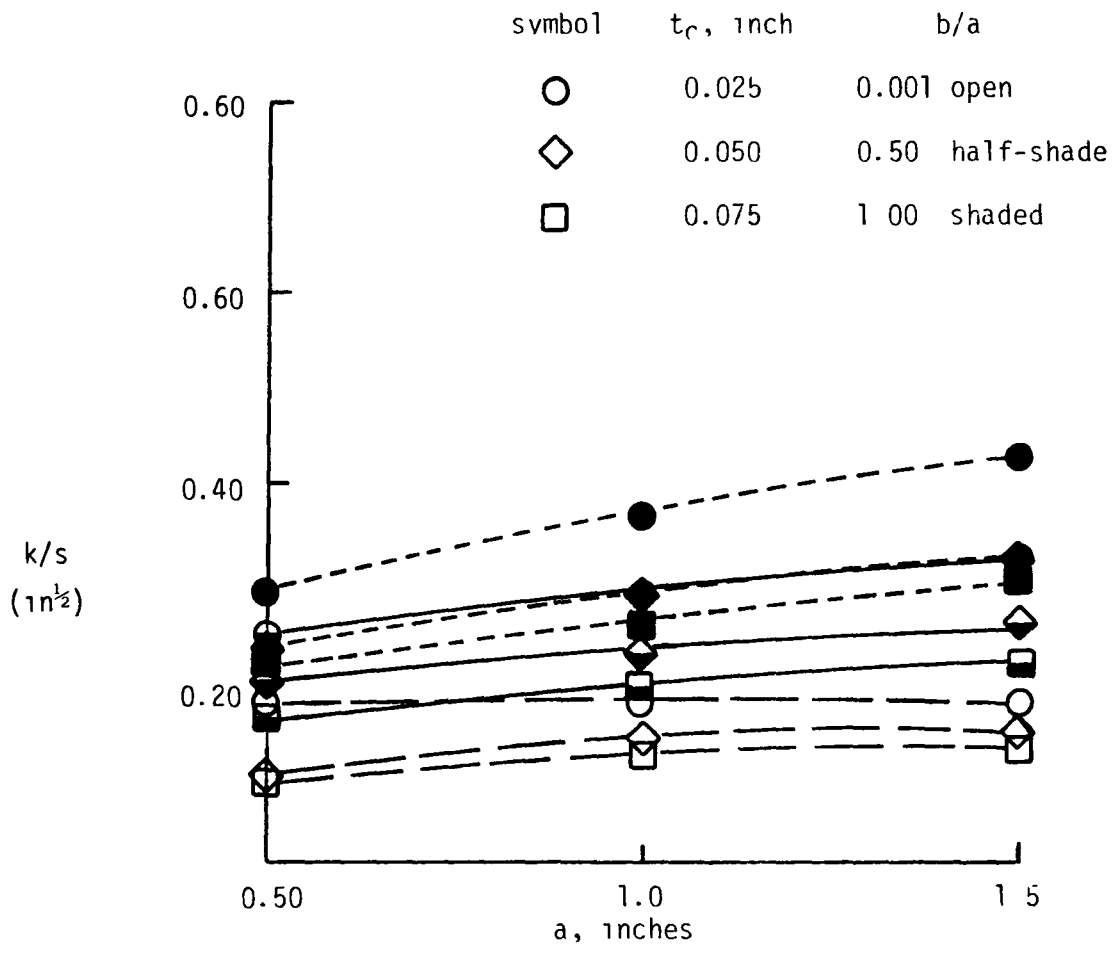

Fig. 19. Stress intensities for 0.050 in thick metal adherend

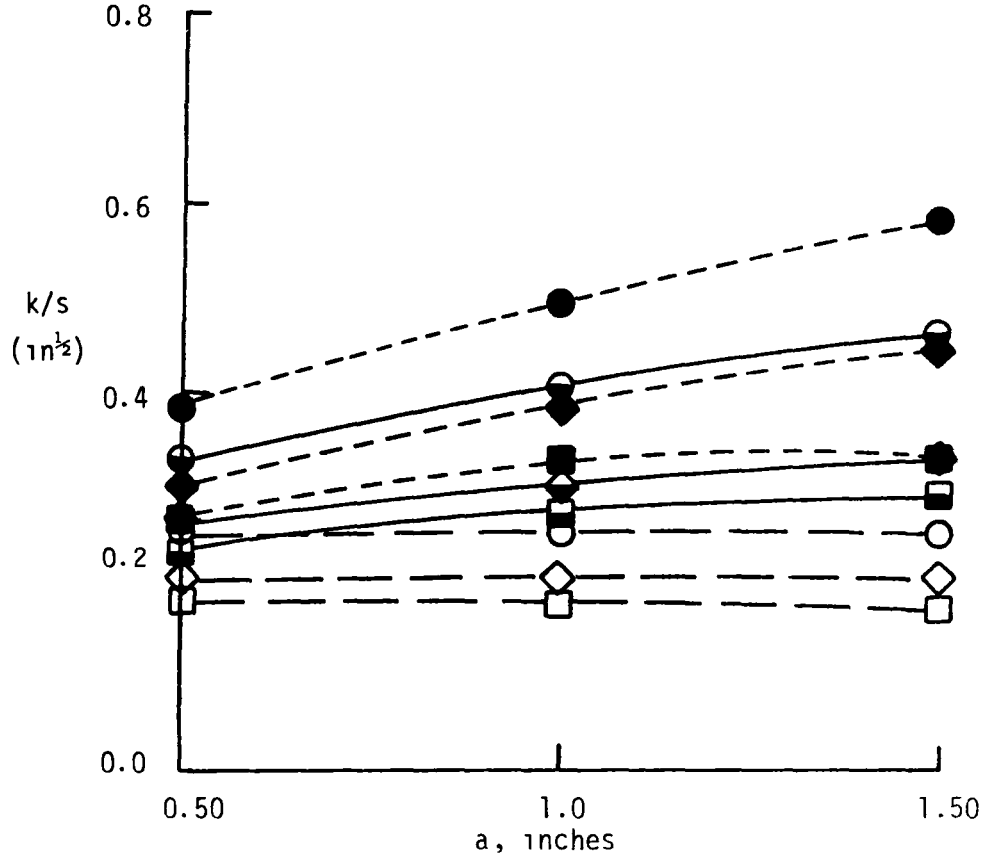

Fig. 20. Stress intensities for 0.100 in thick metal adherend

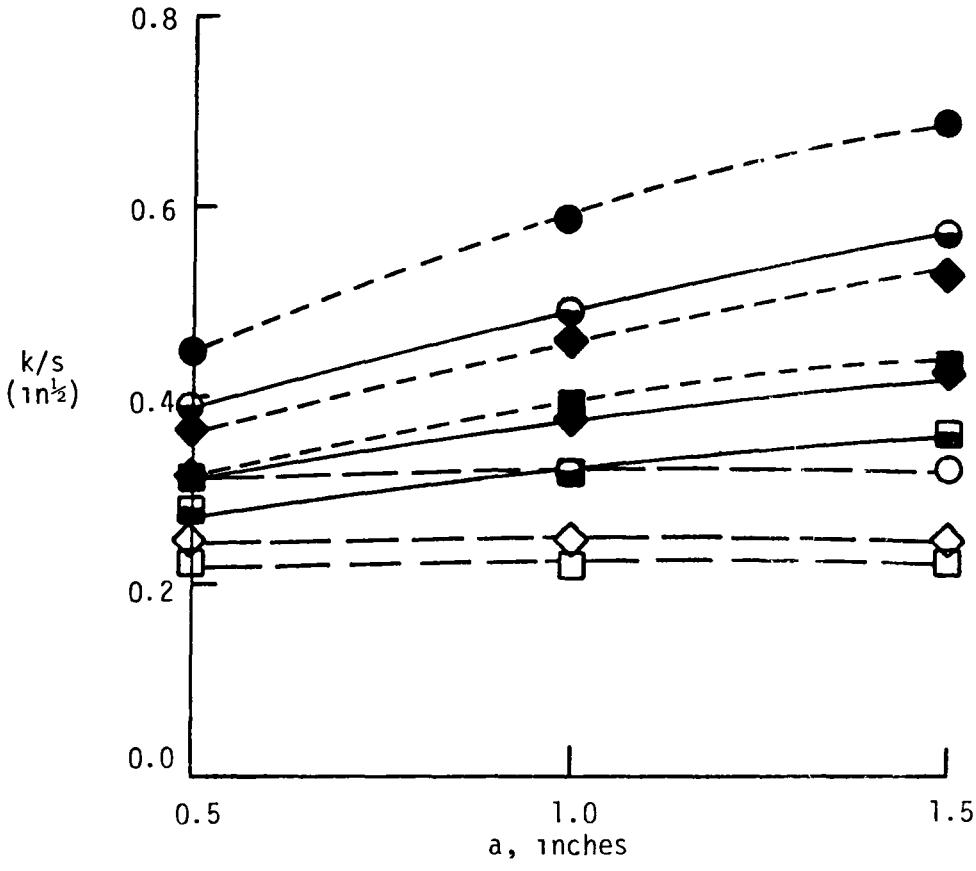

Fig. 21. Stress intensities for 0.15 in thick metal adherend

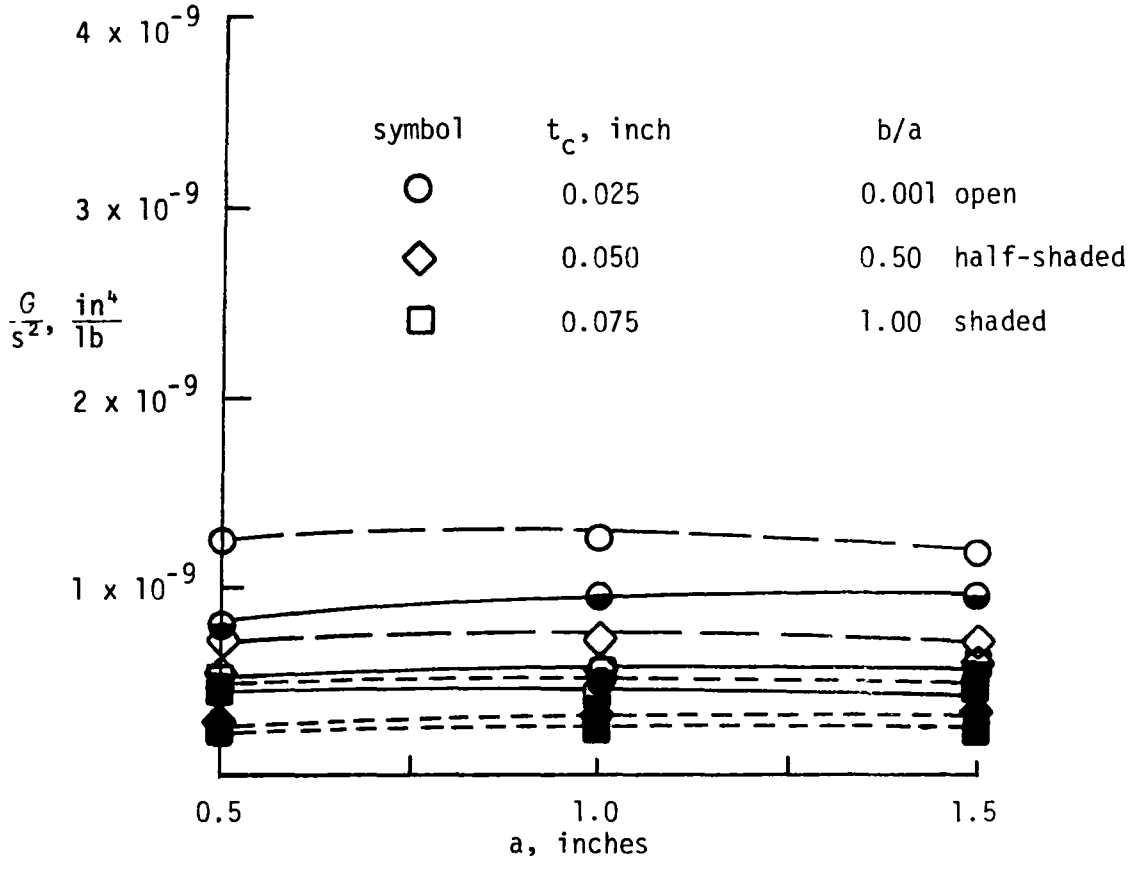

Fig. 22. Strain energy release for 0.05 in thick metal adherend

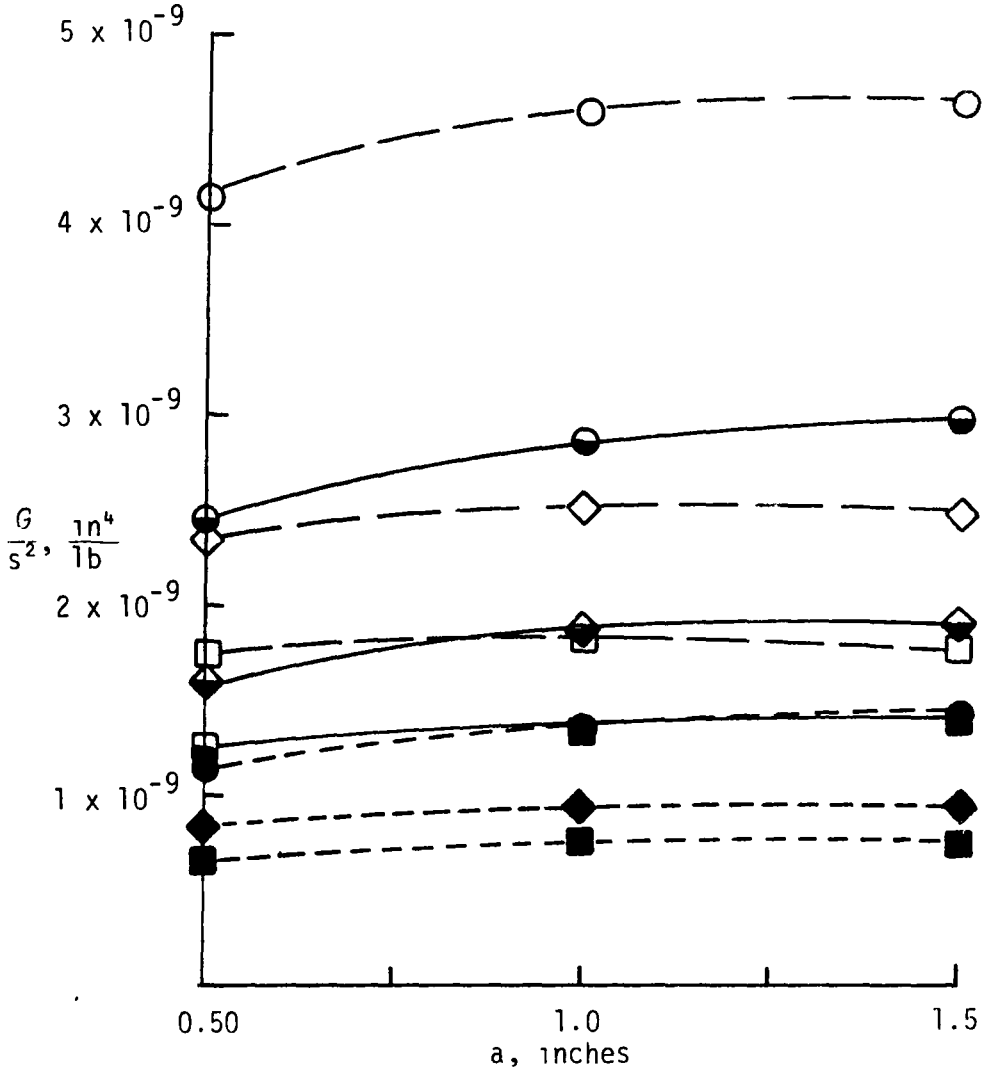

Fig. 23. Strain energy release for 0.10 in thick metal adherend

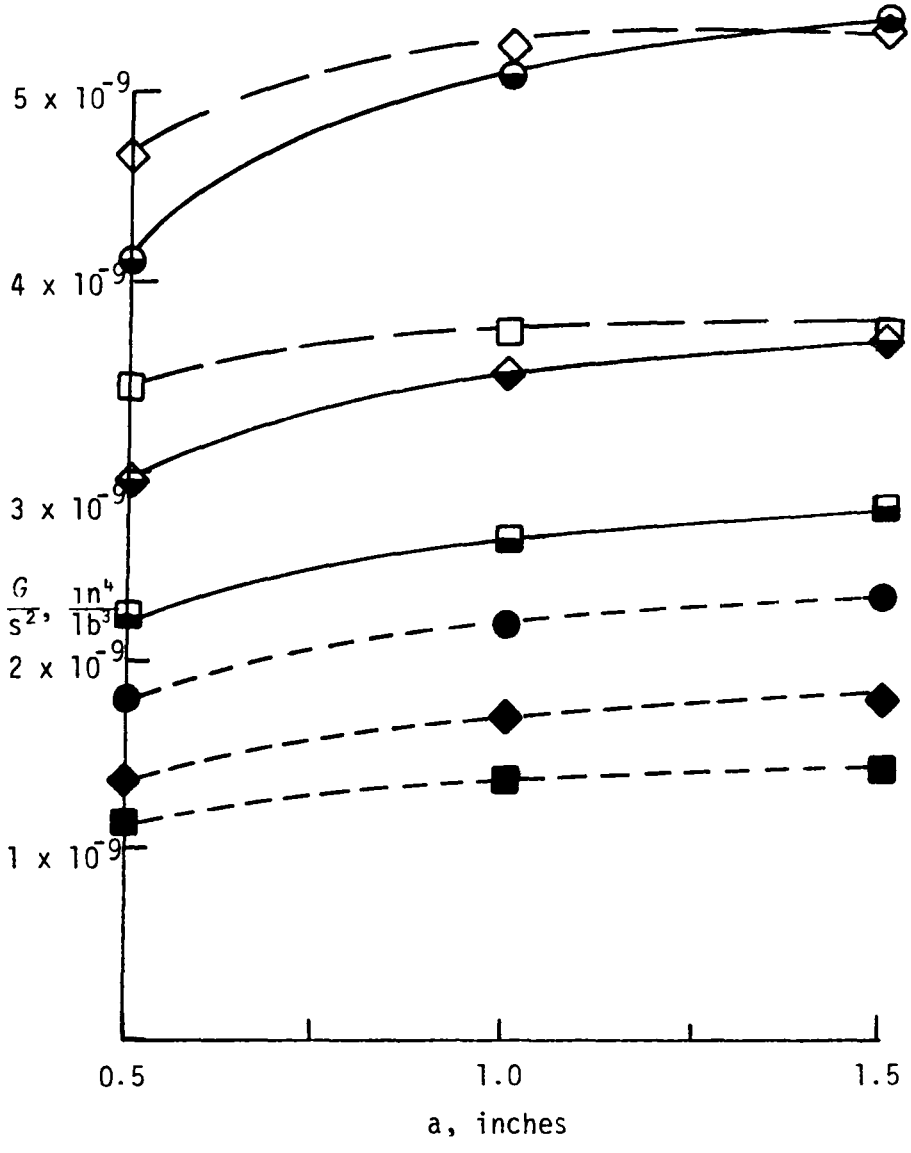

Fig. 24. Strain energy release for 0.15 in thick metal adherend

symbols indicate different composite adherend thicknesses, and different amounts of shading indicate different aspect ratios. On the figures the strain energy release rate normalized by the remote stress squared was plotted against the half crack length.

Examination of the figures revealed that for all metal adherend thicknesses the thickness of the composite had the most pronounced effect on the strain energy release rate. The thinner the composite adherend the higher the strain energy release rate and the more likely debonding would occur. The debond aspect ratio had the next most significant effect. The larger the debond aspect ratio the lower the strain energy release rate. Of all the parameters the crack length had the smallest effect on the strain energy release rate.

As in the case for stress intensities, the effects of debond size, composite adherend thickness, and crack length are more pronounced for the thicker metal adherends. In fact on figure 24 the energy release rates for 0.025 inch composite reinforcement with no debond reinforcing a 0.15 inch metal were so great for all crack lengths that the energy release rates were off scale in the figure. Evidently, the most severe case for debond occurs with a thick metal adherend reinforced with a thin composite sheet with no debonding between adherends.

Nonlinear Effects

Figures 19 through 24 were generated by assuming that the adhesive behaved linearly. Hence, because they were normalized with respect to the remote stress or its square, they can be used to estimate the

stress intensity and strain energy release rate for any remote stress that does not produce nonlinear behavior of the adhesive in the reinforced system. For the different parameters studied, Table 2 gives the values for the remote stresses that cause nonlinear behavior of the adhesive. As evident from the table nonlinear behavior can occur at relatively low remote stresses. For values in the table, the lowest value of remote stress to cause nonlinear behavior occurred for the thickest (0.15 in) metal adherend with a 1.5 inch crack that was reinforced with the thinnest (0.025 in) composite adherend and no debond. For this reinforced system a remote stress of 6,000 psi caused nonlinear behavior of the adhesive. However, for practical purposes, the remote stress applied to this system could be as high as 52,000 psi. To investigate the effects of the nonlinear adhesive on the crack and debond growth predictions, the analysis was conducted using the preceding parameters for both a linear adhesive and nonlinear adhesive.

For the linear analysis an effective shear modulus (see Appendix B) of 65,000 psi was used, while for the nonlinear analysis an effective shear modulus of 65,000 psi was used until the remote stress reached 6,000 psi after which an effective shear modulus of 36,000 psi was used for nonlinear elements of region B (see page 38). With the use of the two different analyses, the stress intensity and the strain energy release were found as

adhesive	k_1	G
linear	18,800	26.1
nonlinear	16,700	26.1
percent error	13	0

For this example, the nonlinear analysis predicted the stress intensity 13 percent below that predicted by the linear analysis. However, the predicted strain energy release rate was the same for both analyses.

At first glance the linear analysis would then accurately predict the debond growth and conservatively estimate the crack growth. But by the use of equations (4) and (5) and the above values the debond and crack growth rates were found at 4.2 inches/cycle and 1.56E-04 inches/cycle respectively. Hence, the debond propagates much faster than the crack. As the debond grows, the magnitude of the stress intensity from the linear and nonlinear analysis converges. In fact, because the debond grows so much faster than the crack, before the crack extends any appreciable amount the stress intensities from the two analyses predict the same crack growth rates. In addition, because the example exhibits the most significant nonlinearity of all the cases considered in Table 2, the linear analysis, and hence figures 19 through 24 can be used to estimate crack and debond growth even when the adhesive behaves nonlinearly.

Prediction of Crack and Debond Growth

To predict the crack and debond growth in a reinforced system, the computer code discussed in Appendix F should in general be employed. However, figures 19 through 24 can also be used to estimate both the debond and crack growth for a variety of reinforced systems in the following manner. First, for the given adherend thickness, crack length, debond size, and remote applied stress, the strain energy release rate, G, and the stress intensity, k_1, can be estimated from figures 19 through 24. Then, equations (4) and (5), the crack and debond growth equations, can be used to estimate the number of applied load cycles to extend the crack by, for example, 10 percent and to extend the debond length (along the longitudinal axis of the reinforced system) by 10 percent. The smallest value of the applied load cycles required to produce these extensions is used with equations (4) and (5) to predict the extension of crack and debond growth. Next, these extensions are added to the original crack and debond length and the entire process is repeated until the stress intensity reaches 56,000 psi-$in^{\frac{1}{2}}$ (fracture occurs) or the desired crack length or number of applied load cycles is reached.

CONCLUSIONS

The failure mode of cracked metal sheets that are reinforced with composite is crack propagation in the metal sheet. Analysis of the crack growth is complicated by the development of a debond near the crack. Herein, an analysis was developed to predict both the debond and crack growth in a reinforced system. The analysis was predicated on the use of strain energy release rate to correlate debond growth. Empirical constants required for the correlation were developed from simple bonded specimens. The correlating equation for the debond growth was then used in a stress analysis that was based on complex variable Green's functions which were developed herein for cracked, isotropic sheets and uncracked, orthotropic sheets. The stress analysis was used to calculate the inplane and interlaminar stresses, the stress intensity at the crack tip, and the strain energy release rate at the debond front. By the use of the analysis, an iterative solution was developed that used the stress intensity and the strain energy release rate to predict the crack and debond growth on a cycle-by-cycle basis.

To verify the analysis, tests were conducted on two different reinforced panels which exhibited different amounts of debonding. For both panels the predicted crack growth was within the accuracy of crack growth prediction in unreinforced metal sheets. Hence,

the analysis appears accurate within the bounds of existing fracture mechanics concepts.

The analysis was used in a parametric study of the effects of boron/epoxy composite reinforcement on crack propagation in aluminum sheets. The study showed that the aspect ratio of the debond area has a significant effect on the crack propagation in the aluminum sheet. For small debonds the crack propagation rate is reduced significantly, but these small debonds have a strong tendency to enlarge. Debond growth is most likely to occur in reinforced systems that have a cracked metal sheet that is reinforced with a relatively thin composite sheet.

The analysis can be used to predict crack growth in reinforced systems. Hence, the analysis can be applied in developing methods to repair damaged metal structure and to increase lives and payloads of metal structures by selective reinforcement.

APPENDIX A

DETERMINATION OF DEBOND CONSTANTS

As discussed in Chapter II, debonding can be predicted in a bonded system with an equation of the type

$$db/dN = c_2 (G)^{n_2} \tag{5}$$

where G is the strain energy release rate and c_2 and n_2 are empirical constants. The objective of this appendix is to determine the empirical constants for the reinforced system used in the experimental portion of this dissertation.

Specimen Fabrication

To determine c_2 and n_2, several test specimens with the configuration shown in figure A.1 were fabricated. The specimens consisted of 1-inch wide strips of 0.188 inch thick 2024-T3 aluminum bonded to 0.03 inch thick unidirectional boron/epoxy The strips were bonded with Shell EA-934 room curing adhesive. To maintain a constant adhesive thickness in the bond, 2 percent by volume of 0.004 inch diameter glass beads were added to the adhesive prior to bonding.

The process used to bond the aluminum to the composite was as follows

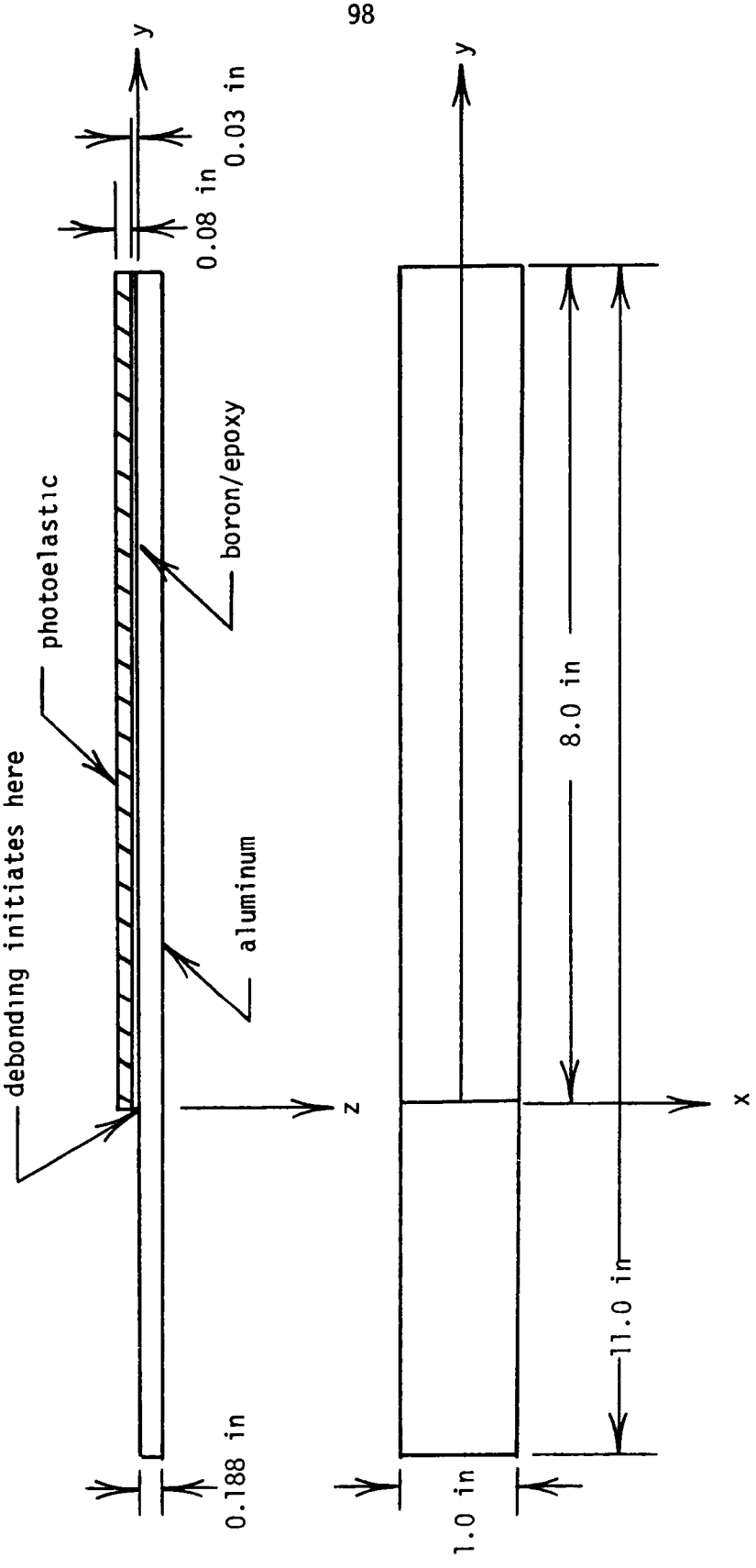

Fig. A.1. Debond specimen configuration

SURFACE PREPARATION

Aluminum 2024-T3

1. Vapor degrease - perchloroethylene condensing vapors for 5 to 10 minutes.
2. Grit blast with 220 grit at 90 psig.
3. Alkaline degrease - Oaklite 164 solution (9 - 11 ounces/ gallon of water) at 190 ±10° F for 15 minutes. Rinse immediately in large quantities of cold running water.
4. Acid etch - place panels in the following solution for 10 minutes at 150° ±5° F.

Distilled water	30 parts
Sulfuric acid (conc)	10 parts
Sodium Dichromate	1 part

5. Rinse - rinse panels in clear, deionized running water.
6. Dry - air dry 15 minutes; force dry 10 minutes at 150° F ±10° F.

Boron/epoxy

1. Vapor degrease as above.
2. Grit blast with 220 grit at 30 psig.

BONDING

1. Bond within 4 hours of surface preparation.
2. Coat surfaces of both adherends prior to bonding.
3. Cure at room temperature under 15 psig ±2 psig pressure.
4. Record date of bonding.

The method of surface preparation for the aluminum was taken from Cagle (1973) while the surface preparation for the boron/epoxy and the bonding method was developed by the author. The bonding process was verified with lap-shear strength tests of the bonded system.

As shown in figure A.1 photoelastic material was bonded to the surface of the boron/epoxy. The photoelastic material enabled tracking of the debond front in the fatigue tests of the specimens.

Fatigue Tests

The fabricated specimens were tested in a servo-hydraulic fatigue machine with a maximum load capacity of 10,000 pounds. All of the tests were conducted at a loading frequency of 10 Hz with a ratio of minimum to maximum load in the load cycle of $R = 0.05$. Duplicated tests were conducted for maximum loads of 5,000, 4,000, and 3,000 pounds.

As the specimens were tested, a debond developed at the change of cross section and propagated between the aluminum and boron/epoxy adherends. Throughout the tests the location of the debond front was indicated by an isochromatic that was observed by viewing the photoelastic material through a polarizing material. The location of the debond front is plotted against the number of applied load cycles on figure A.2 for all of the tests. The results of these tests will be used with a stress analysis to determine the empirical constants c_2 and n_2.

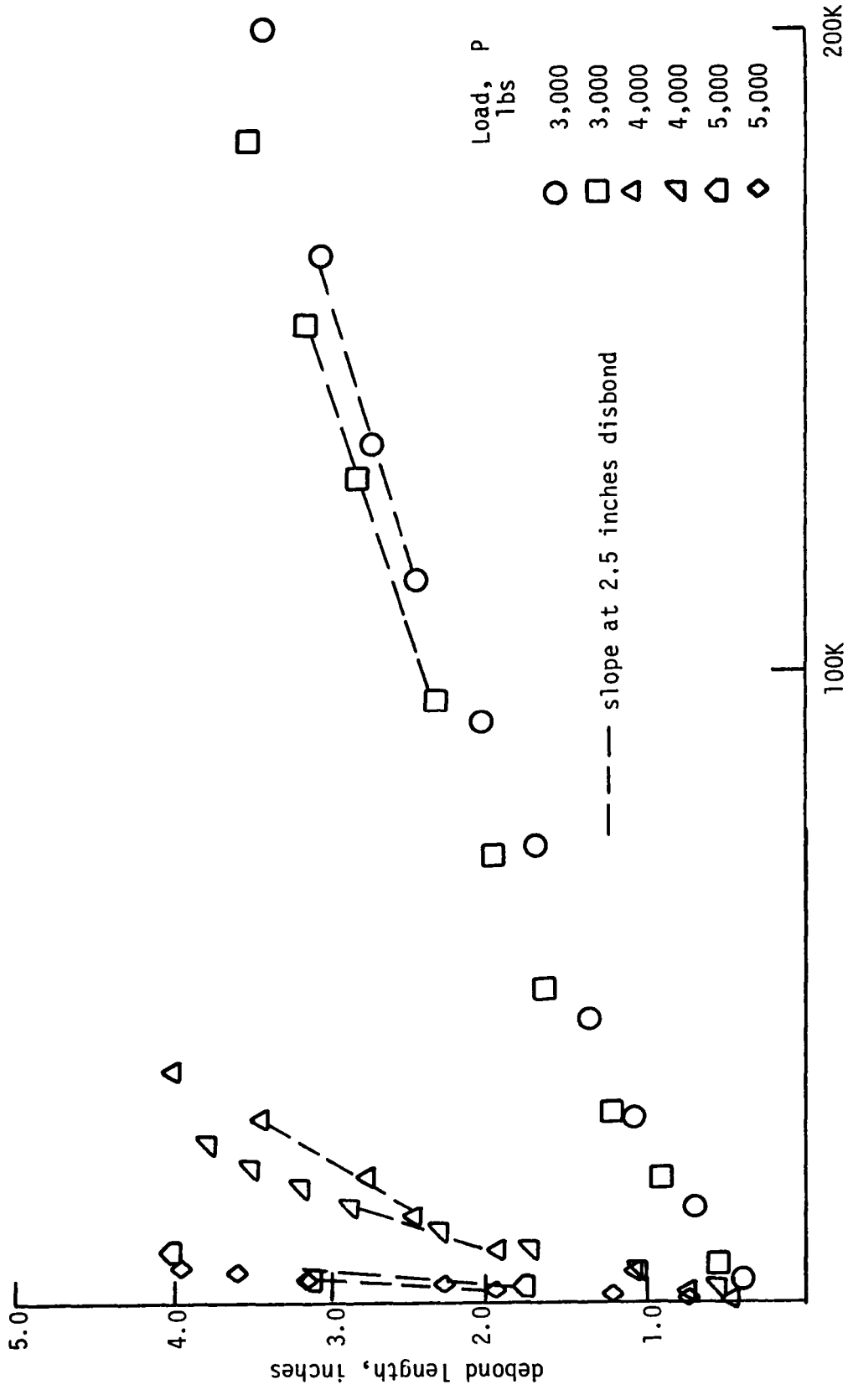

Fig. A.2. Debonding behavior

Stress Analysis

Because of the change of cross section of the test specimen, as an axial load, P, is applied to it, it bends. As shown by Timoshenko (1961) the equilibrium equation for a beam that exhibits both axial and bending deformation can be written as

$$V = \frac{dM}{dy} + P\frac{dw}{dy} \tag{A.1}$$

where V is the shear, M is the bending moment, and P is the tensile axial load. To use equation (A.1) both the moment M and the axial load P were related to the deflection in the z-direction, w, with two equations given by Calcote (1969) as

$$\frac{P}{A} = A_{11}\frac{dv}{dy} - B_{11}\frac{d^2w}{dy^2} \tag{A.2}$$

$$M = B_{11}\frac{dv}{dy} - D_{11}\frac{d^2w}{dy^2} \tag{A.3}$$

where A is the cross sectional area of the beam and dv/dy is the axial strain of the beam and

$$A_{11} = \sum_{i=1}^{k} Q_i(z_i - z_{i-1}) \qquad B_{11} = \frac{1}{2} \sum_{i=1}^{k} Q_i(z_i^2 - z_{i-1}^2)$$

$$D_{11} = \frac{1}{3} \sum_{i=1}^{k} Q_i(z_i^3 - z_{i-1}^3) \qquad Q_k = \frac{(E_y)_i}{1 - (\nu_{xy}\nu_{yx})_i}$$

where i indicates the layer of a beam with k layers and z is measured from any reference surface.

Eliminating dv/dy from equations (A.2) and (A.3) yielded an expression for the moment as

$$M = \frac{B_{11}}{A_{11}} \left\{ P + B_{11} \frac{d^2w}{dy^2} \right\} - D_{11} \frac{d^2w}{dy^2} \tag{A.4}$$

Substituting equation (A.4) into equation (A.1) and differentiating once with respect to y, yielded a governing equation as

$$q_z = \left\{ \frac{B_{11}^2}{A_{11}} - D_{11} \right\} \frac{d^4w}{dy^4} + P \frac{d^2w}{dy^2} \tag{A.5}$$

where q_z is a transverse distributed load acting on the beam.

The boundary conditions for equation (A.5) were determined from the end conditions of the test specimen installed in the test machine as shown schematically on figure A.3a. With the assumption

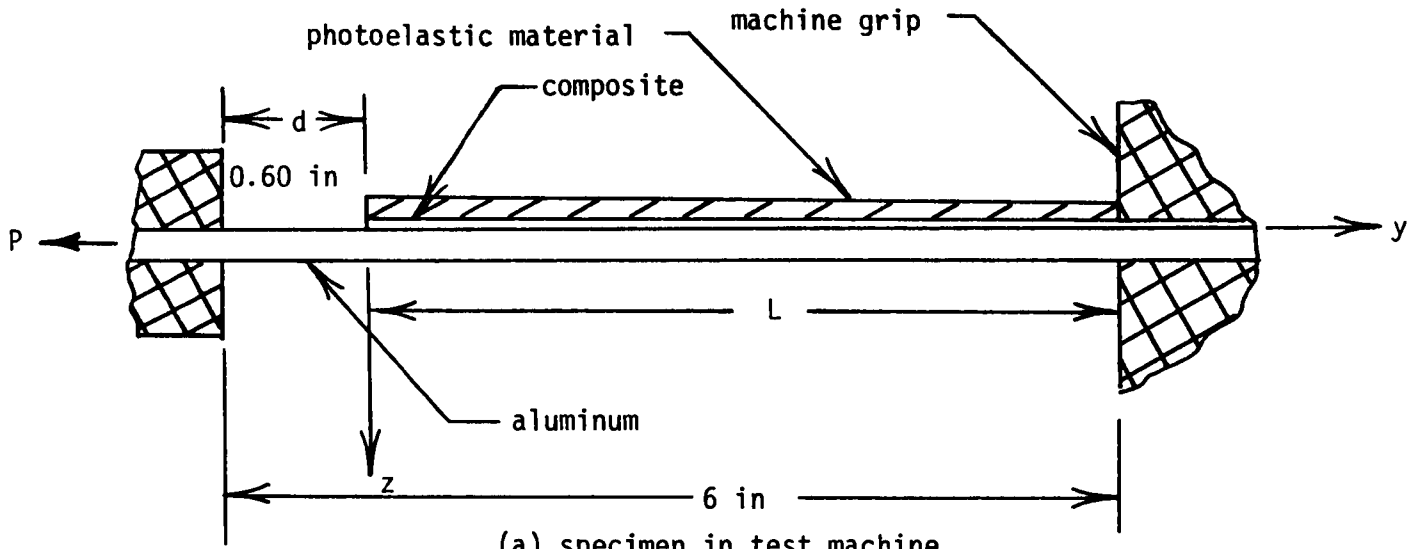

(a) specimen in test machine

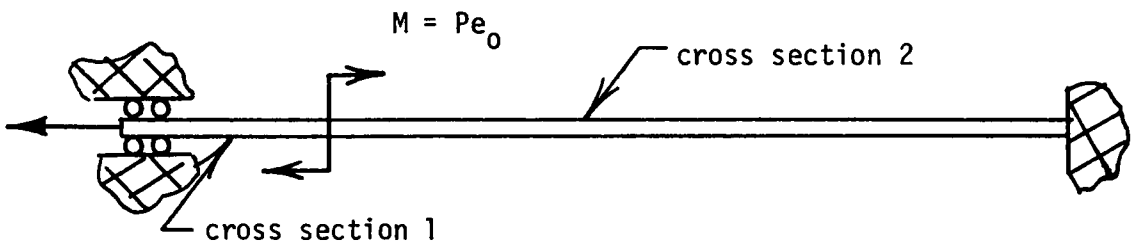

(b) beam model of specimen

Fig. A.3. Beam model for stress analysis

that the specimen is effectively fixed at both ends by the relatively massive test machine grips the boundary conditions were determined as

$$w(-d) = 0 \qquad w(L) = 0$$

$$\frac{dw(-d)}{dy} = 0 \qquad \frac{dw(L)}{dy} = 0 \tag{A.6}$$

At the change in cross section of the test specimen a local moment given as

$$M = Pe_o \tag{A.7}$$

where e_o is the distance between centroids of the two cross sections, was produced. With this moment the beam can be modeled as a symmetric beam with two different cross sections acted upon by a local moment M at the change in cross section and an axial load P as shown in figure A.3b. For the model shown in figure A.3b, equation (A.5) was solved with conventional finite difference techniques (Ames 1971).

To verify the analysis, the strains were determined by both the finite difference analysis and by experiments. The test specimen shown in figure A.3a was analyzed. In cross section 2 the specimen was composed of four layers: the metal core, the adhesive layer, the composite cover, and the photoelastic material. The thickness, moduli, and Poison's ratio for each of these layers are given as

layer	material	thickness (in)	elastic modulus psi	Poisson's ratio
1	aluminum	0.188	10^7	0.30
2	adhesive	0.004	600,000	0.40
3	composite	0.030	3×10^7	0.21
4	photoelastic	0.083	390,000	0.36

With the preceding values and the surface of the metal with strain gages (see figure A.4) as a reference plane A_{11}, B_{11}, and D_{11} were found for section 1 (see figure A.3) as

$$A_{11} = 2.1 \times 10^6 \text{ lbs/in} \qquad B_{11} = 200{,}000 \text{ lbs}$$

$$D_{11} = 2{,}500 \text{ lbs/in}$$

and for section 2 as

$$A_{11} = 3 \times 10^6 \text{ lbs/in} \qquad B_{11} = 392{,}000 \text{ lbs}$$

$$D_{11} = 65{,}000 \text{ lbs/in}$$

With the use of the previous values and an applied load P of 5,000 pounds as shown on figure A.4, the finite difference method was used to calculate deflections and curvatures of the beam. With the curvatures the strains in the beam were calculated on the surface of the metal with (Calcote 1969)

$$\varepsilon_o = \frac{1}{A_{11}} \left\{ P + B_{11} \frac{d^2w}{dy^2} \right\}$$

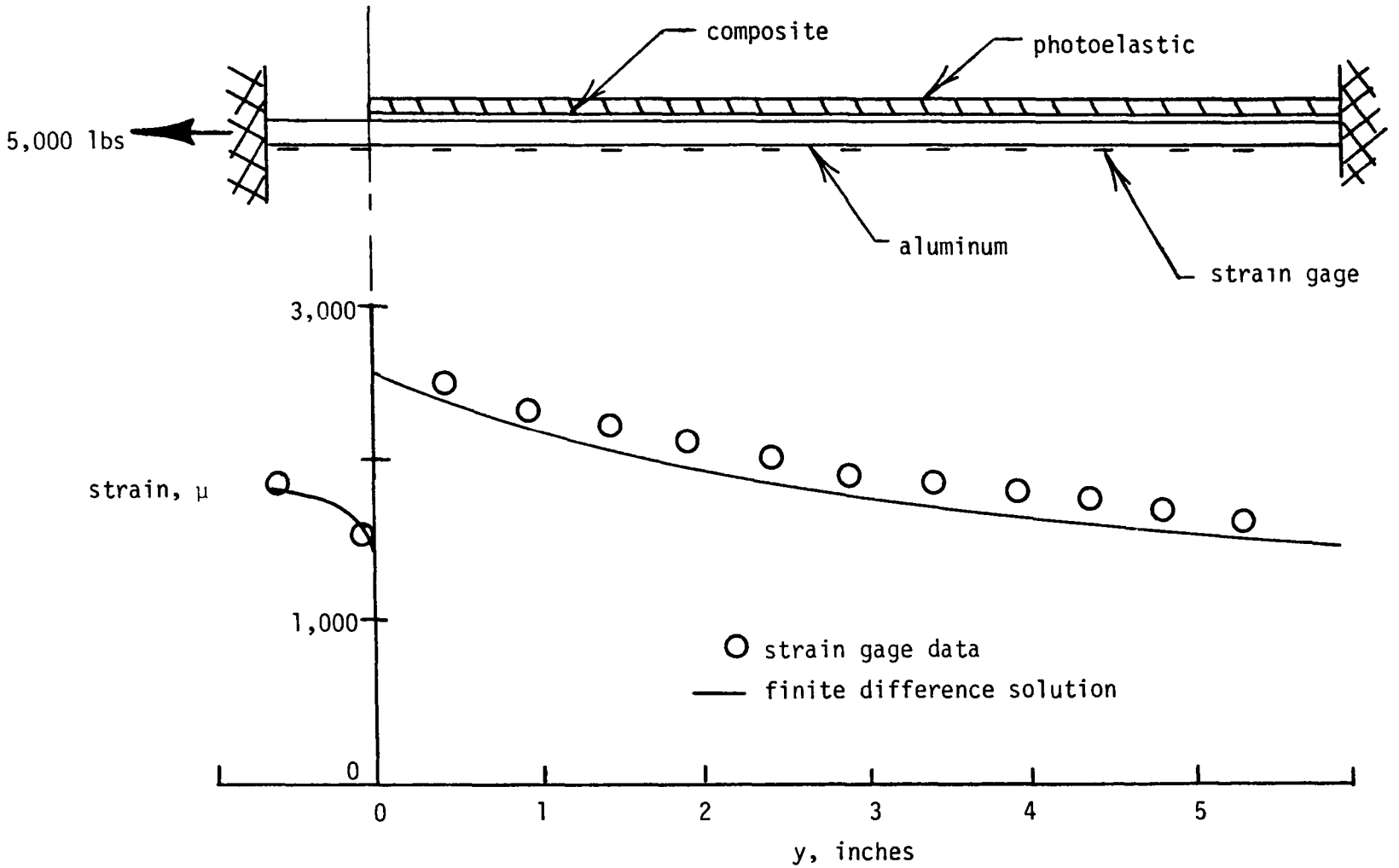

Fig. A.4. Comparison of finite difference solution with experimental data

On figure A.4 the solid line indicates calculated strains on the surface of the metal adherend while the circles indicate strains obtained experimentally with strain gages. As evident from the figure. the comparison is very good. Consequently, the developed stress analysis is adequate and can be used to calculate the strain energy release rates as the test specimens debond.

Calculation of Strain Energy Release Rates

The strain energy release rate can be calculated as

$$G = \lim_{\Delta b \to 0} \left\{ \frac{\Delta W}{\Delta b} - \frac{\Delta U}{\Delta b} \right\} \tag{A.8}$$

where W is the change in work done on the system, U is the change in internal strain energy, and Δb is a small extension of the debond. With the assumption that the debond extends at the maximum applied load, the work done as the debond extends can be calculated as

$$\Delta W = P\left\{\Delta\delta_{axial} + \Delta\delta_{bending}\right\} + M\Delta\Theta\Theta \tag{A.9}$$

where $\Delta\Theta\Theta$ is the rotation of the beam at the debond front. The change in internal energy can be calculated as

$$\Delta U = \Delta U_{axial} + \Delta U_{bending} \tag{A.10}$$

Substituting equations (A.9) and (A.10) into equation (A.8) and rearranging slightly yields the strain energy release rate as

$$G = \lim_{\Delta b \to 0} \left\{ P \frac{\delta_{axial}}{\Delta b} - \frac{\Delta U_{axial}}{\Delta b} + P \frac{\delta_{bend}}{\Delta b} + \frac{M \Delta \Theta_{bend}}{\Delta b} - \frac{\Delta U_{bend}}{\Delta b} \right\} \tag{A.11}$$

The first two terms, which neglect bending, of equation (A.11) can be calculated as shown by Roderick et al (1975) as[1] (for a unit width)

$$\lim_{\Delta b \to 0} \left\{ P \frac{\delta_{axial}}{\Delta b} - \frac{\Delta U_{axial}}{\Delta b} \right\} = \frac{t_c E_c P^2}{2 E_m \tau_m (t_m E_m + t_c E_c)} \tag{A 12}$$

The last three items, which are due to bending, can be calculated with the finite difference results in the following manner

First, the axial deflection due to bending is calculated as shown by Den Hartog (1952) as

$$\delta_{bend} = \frac{P}{2} \int_{-d}^{L} \left\{ \frac{dw}{dy} \right\}^2 dy \tag{A.13}$$

---

[1] The flexible adhesive and photoelastic material are neglected because they have little effect on the strain energy due to the axial load

where the slope dw/dy was calculated at each nodal point in the finite difference approximation. Between the nodes the slope was assumed to vary linearly. The integration of equation (A.13) was done piecewise over the length of the beam. The work done by the moment was expressed as

$$M = \frac{M}{2}\left\{\frac{dw}{dy}\right\} \tag{A.14}$$

The strain energy due to bending was calculated as

$$U_{bend} = \int_{-d}^{L} \frac{M^2 \; A_{11}}{2(A_{11}D_{11} - B_{11})}\, dy \tag{A.15}$$

where again the integration was performed in a piecewise fashion.

Equations (A.13) through (A.15) were evaluated before and after a debond extension Δb. The quantities were subtracted to calculate the last terms of equation (A.11). The result was added to equation (A.12) to give the strain energy release at the debond front. In figure A 5 the solid lines show the calculated strain energy release rate plotted against the debond lengths for values of applied loads of 5,000, 4,000, and 3,000 pounds. The dashed line on the figure shows the strain energy release rate--neglecting bending--calculated with equation (A 12) As evident from the figure, when the debond length is greater than 0 5 inch or less than 4.5 inches, the contribution of bending to the strain energy release rate is small. Particularly,

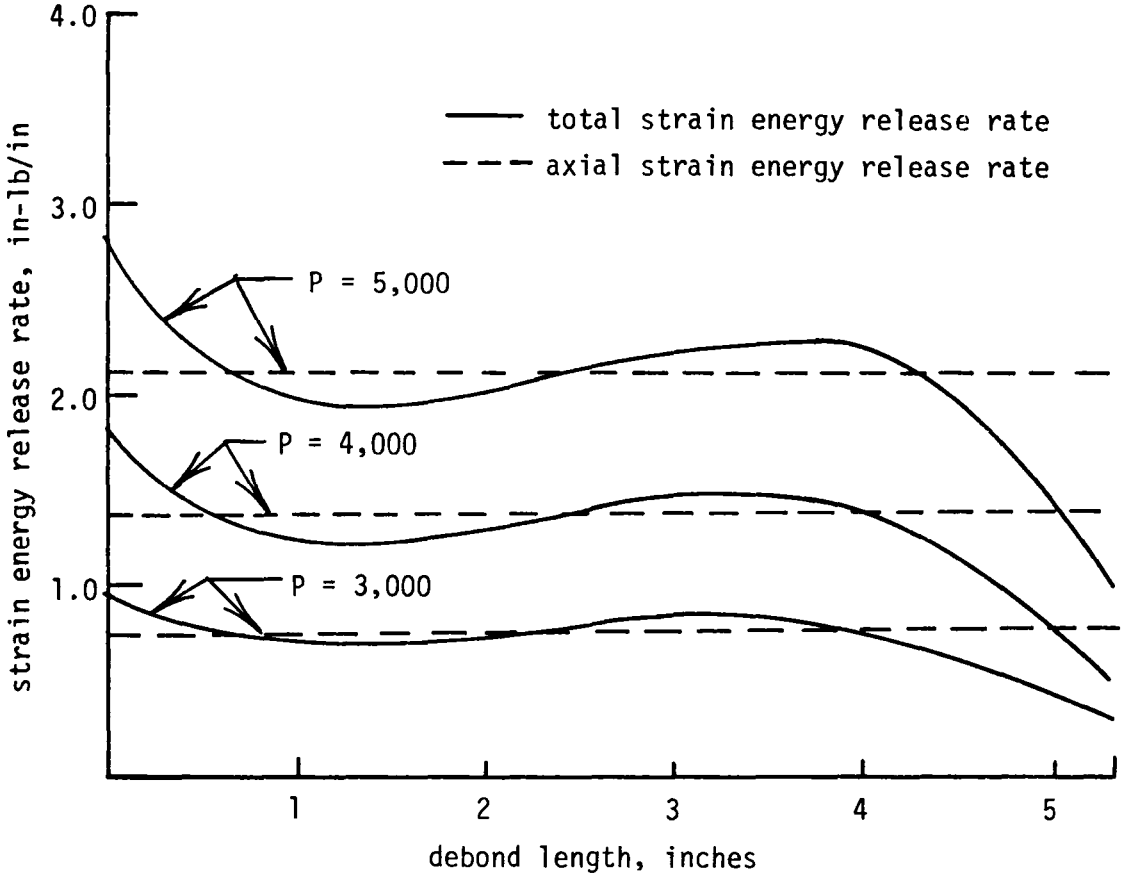

Fig. A.5. Strain energy release rate versus debond front location

when the debond length is about 2.5 inches long, the bending contribution is zero.[2] Consequently, for a debond length of 2.5 inches, equation (A.12) can be used to calculate the strain energy release rate

Curve Fit for Empirical Constants

The debond rates for the configuration analyzed were determined by taking the slope of the curves at a 2.5-inch debond length from figure A.2. These experimental rates and the corresponding values of the calculated strain energy release rates are shown in Table A.1. The values in Table A.1 were used to determine the empirical constants c_2 and n_2 in equation (5) with a least squares fit (Wylie 1966). To perform the fit, equation (5) was written as

$$\log(db/dN) = \log(c_2) + n_2 \log(G) \tag{A.16}$$

As a result of the curve fit, c_2 and n_2 were found as

$$c_2 = 3.158 \times 10^{-5} \qquad n_2 = 3.616$$

Figure A.6 shows the data as points and the fitted equation (5) as a solid line. As evident from the figure, the equation fits the

---

[2]Actually, there are also two other debond lengths where the strain energy release rate is zero, but they are located closer to the ends of the specimen where the analysis may be more inaccurate than at the 2.5-inch debond length.

TABLE A.1

STRAIN ENERGY RELEASE RATES

AND DEBOND PROPAGATION RATES

load lbs	strain energy release rate, G in-lbs/in	debond rate db/dN in/cycle
5,000	2.15	5.60×10^{-4}
5,000	2.15	5.20×10^{-4}
4,000	1.38	1.04×10^{-4}
4,000	1.38	8.00×10^{-5}
3,000	0.77	1.26×10^{-5}
3,000	0.77	1.33×10^{-5}

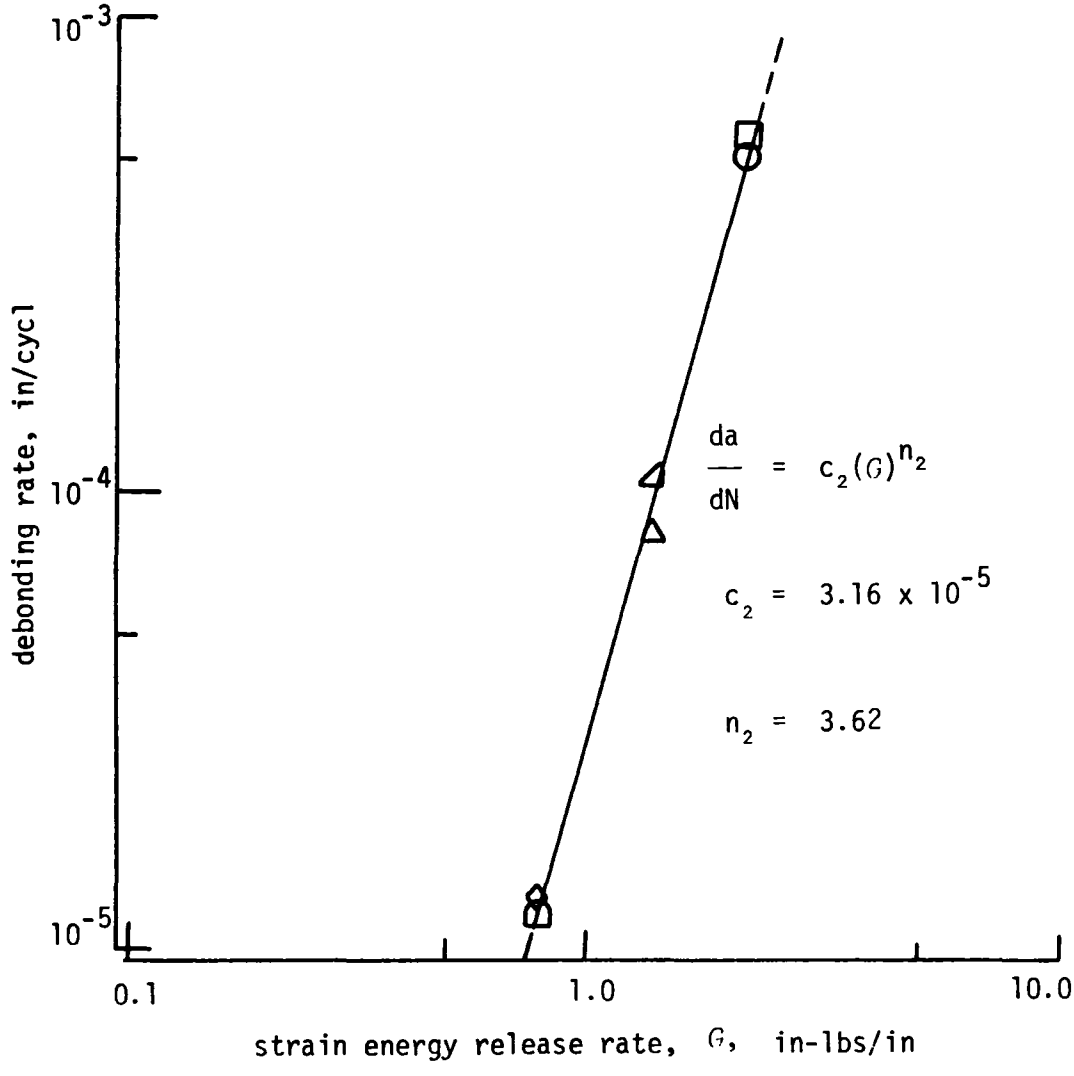

Fig. A.6. Correlation of debonding rates with strain energy release rates

data well. With the determined empirical constants, equation (5) can be used to predict debond propagation rates whenever the strain energy release rate can be determined.

APPENDIX B

ADHESIVE SHEAR DEFORMATION ASSUMPTION

As mentioned in Chapter IV, the complexity of the analysis for a reinforced system is significantly reduced by assuming that the adhesive only undergoes shear deformation while the adherends only undergo extensional deformations that do not vary through the adherend thickness. Herein, the validity of these assumptions were investigated by comparing a one-dimensional solution that was based on these assumptions with a more rigorous two-dimensional finite element solution. Before the one-dimensional and two-dimensional solutions were compared the bulk properties of the adhesive were determined.

Adhesive Bulk Properties

To determine the bulk properties of the adhesive an appropriate test specimen was designed and fabricated in several steps. First, a female plastic mold was made from the specimen shown in figure B.1a. Then, the adhesive liquid base and hardener were combined and cast into the mold. Next, after curing 24 hours in the mold the adhesive specimen was removed and cured an additional 5 days before it was handled. Finally, x-rays were taken of the specimen to locate air bubbles developed in the molding process. Specimens that contained

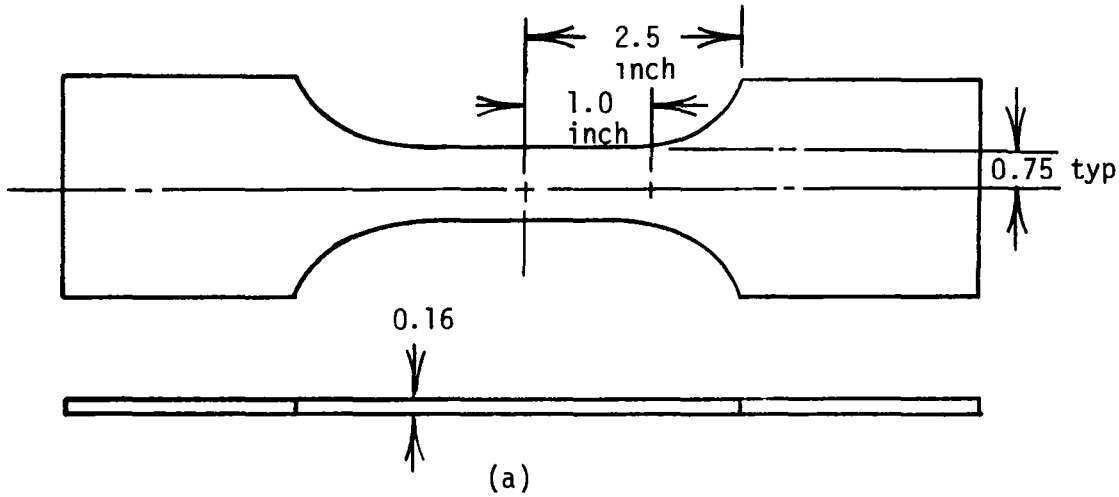

(a)

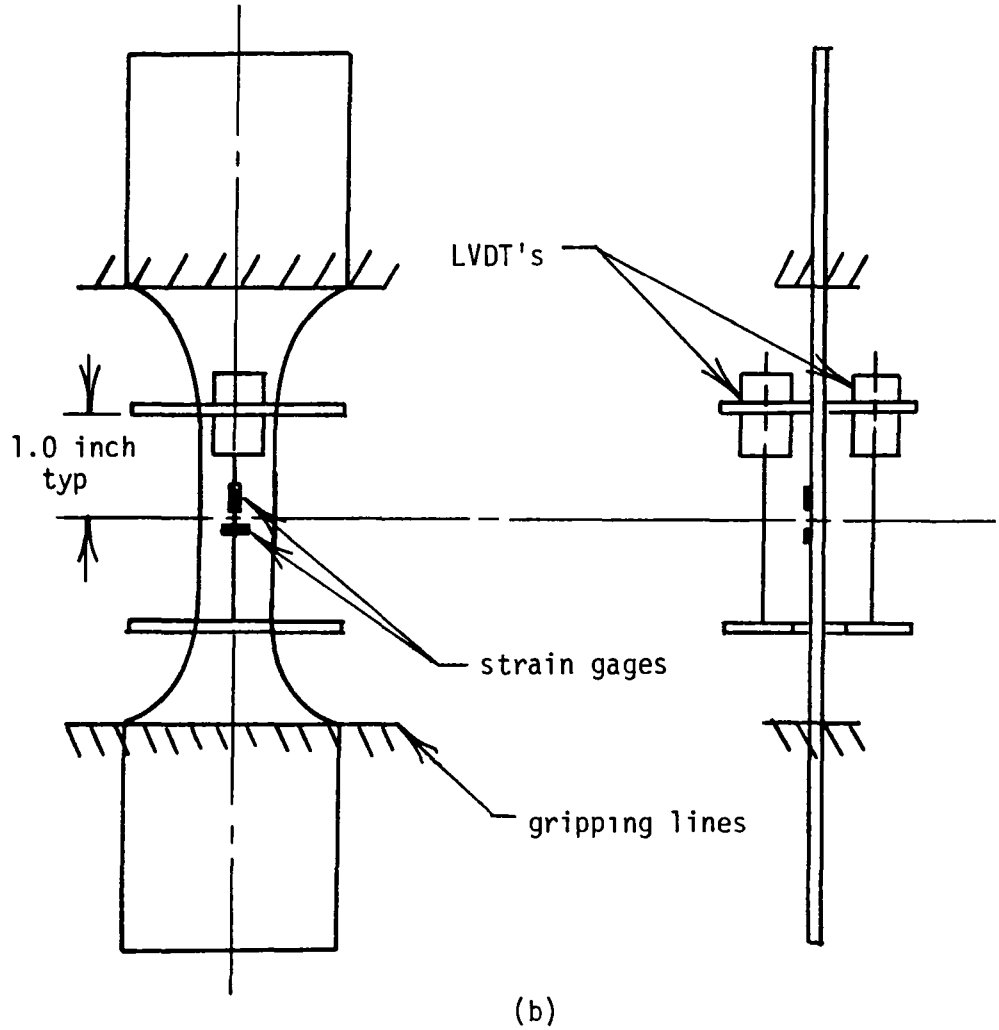

(b)

Fig. B.1. Bulk adhesive specimen configuration and instrumentation

large air bubbles in critical areas were scrapped Six test specimens were fabricated in this manner but only three were acceptable for testing.

Prior to the testing the specimens were instrumented with strain gages and linear variable differential transformers (LVDT) as shown in figure B.1b. The strain gages were used to obtain the longitudinal and transverse strain while the LVDT's were used to check the strain gages (the LVDT's were wired to eliminate bending effects in their readings while the strain gages would include bending in their readings). Discrepancies between the readings would indicate bending due to poor specimen alignment in the test machine Each instrumented specimen was placed in a servo-hydraulic test machine with a loading range of 2,000 pounds and a sensitivity of $\pm$10 pounds. Then, each specimen was loaded to failure at a rate of 80 lbs/sec.

In this manner, the three specimens were tested and the results were nearly identical for all three of the tests. For all specimens, the longitudinal strain calculated from LVDT's agreed within 1.5 percent of the longitudinal strain gage reading and indicated the specimens were aligned properly in the test machine. The data obtained from the strain gages are shown on figure B.2 in the form of a stress-strain plot. On the figure the heavy solid line indicates the strain in the loading direction ε_y and the dashed line indicates the strain transverse to the loading direction ε_x. As indicated by the light solid lines on the figure, the stress-strain curve can be approximated by a bilinear stress-strain curve with a change of slope occurring at 4,200 psi.

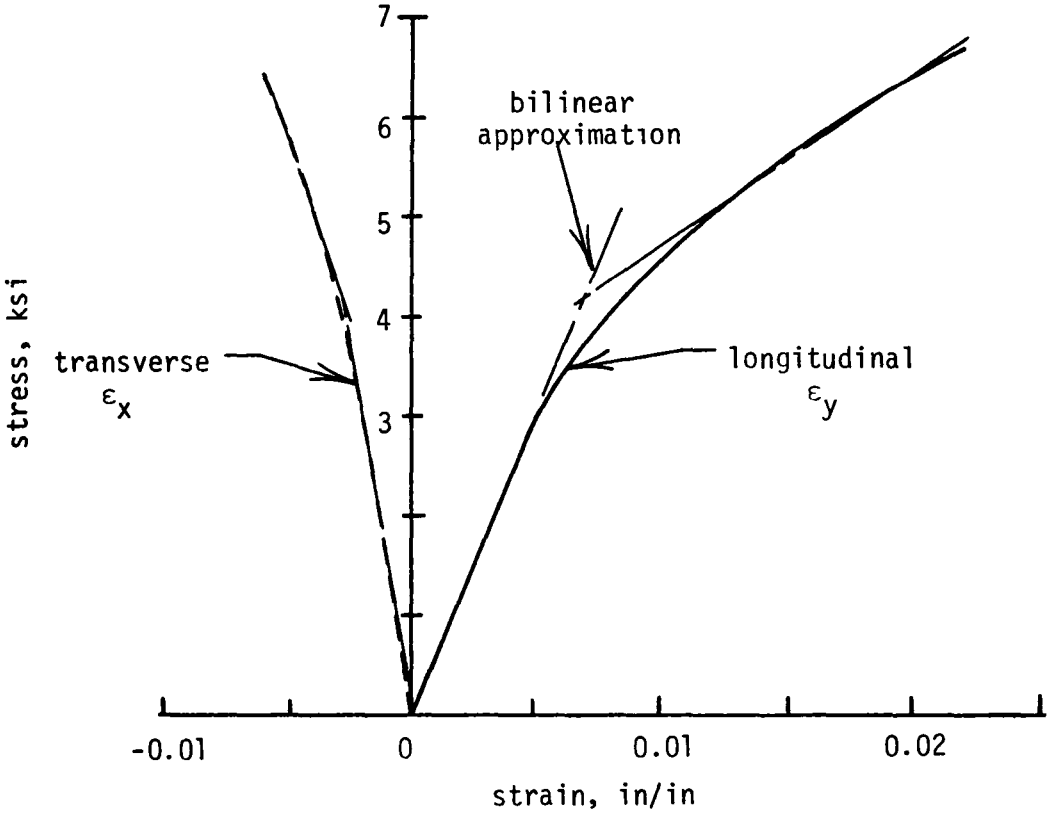

Fig. B.2. Adhesive stress-strain curve

In the initial linear region the following values were obtained from the curve:

$$\Delta\sigma_y = 3{,}000 \text{ psi}, \qquad \Delta\varepsilon_y = 0.005, \qquad \varepsilon_x = 0.002$$

Using these parameters, the Poisson's ratio and the elastic modulus were calculated as

$$\nu_{yx} = \frac{\varepsilon_x}{\varepsilon_y} = 0.40 \qquad E_y = \frac{\Delta\sigma_y}{\Delta\varepsilon_y} = 600{,}000 \text{ psi}$$

With the assumption that the adhesive is isotropic the shear modulus was calculated as

$$G = \frac{E_y}{2\,(1 + \nu_{yx})} = 215{,}000 \text{ psi}$$

Along similar lines, the material parameters in the second linear region were determined as

$$\nu_{xy} = 0.28 \qquad E_y = 190{,}000 \text{ psi} \qquad G = 74{,}000 \text{ psi}$$

The fracture of the specimen occurred at a stress of 6,600 psi at an axial strain, ε_y, of 0.0215. With the preceding material property values for the adhesive, the one-dimensional and two-dimensional solutions were compared.

As a test case, the shearing stresses in the adhesive layer of the specimen shown on figure B.3a (the specimen is symmetric about the x-y plane) was calculated with both types of solutions for a plane stress state. Although the solution was for plane stress, for the self-equilibrating load system shown on figure A.1a the stress distributions are identical for both plane stress and strain states (Timoshenko (1951)). Consequently, although the tests case considered a state of plane stress, the results are also applicable to a state of plane strain which may be more appropriate for a section taken through the thickness of the reinforced system shown on figure 9.

One-Dimensional Solution

Figure B.3b shows a freebody of the specimen shown in figure B.3a. On the figure P is half the load in a composite adherend, $F(y)$ and $q(y)$ are the load in the metal adherend and the shear flow in the adhesive at any point y, and t_m, $2t_c$, and t_{ad} are the thicknesses of the metal, composite, and adhesive respectively.

The change in the load $F(y)$ with respect to y is the shear flow in the adhesive layer given as

$$q(y) = \frac{dF(y)}{dy} \tag{B.1}$$

The shear stress in the adhesive is this shear flow divided by the width, w, of the specimen, given as

$$\tau(y) = \frac{q}{w} = \frac{1}{w}\frac{dF(y)}{dy} \tag{B.2}$$

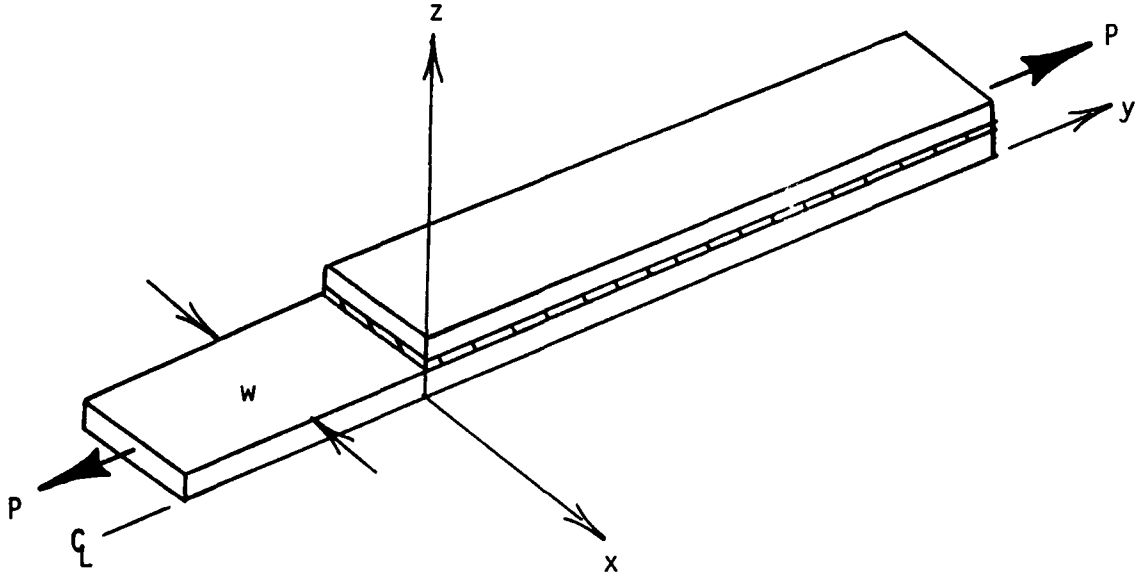

(a) Specimen configuration

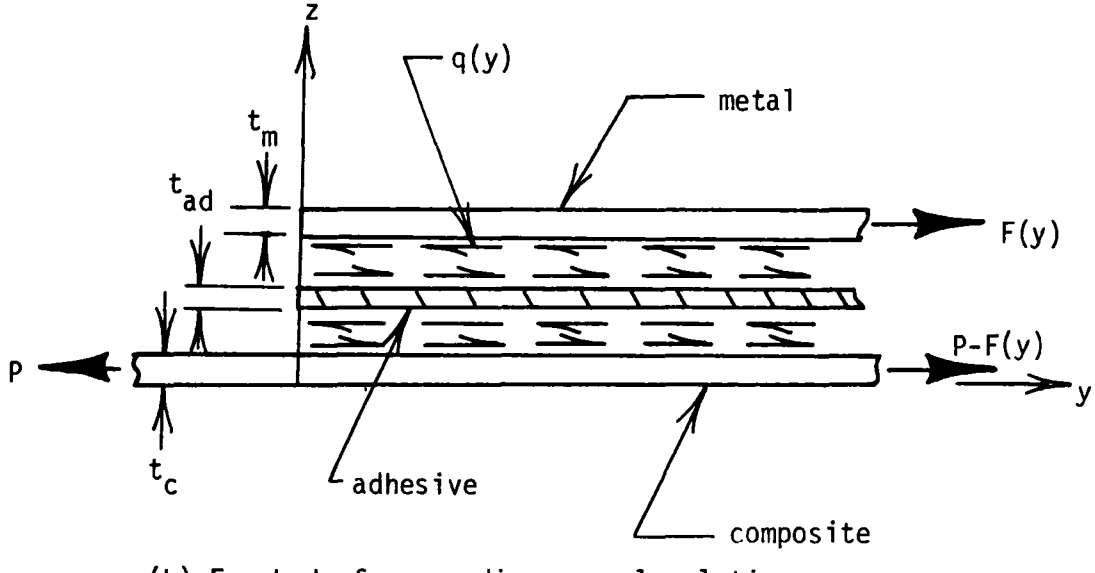

(b) Freebody for one-dimensional solution

Fig. B.3. Specimen configuration and freebody for one-dimensional solution

With the assumption that the adhesive only undergoes shear deformation and that this deformation does not change through the adhesive thickness, the shearing stress in the adhesive can be related to the shearing strain in the adhesive by the constitutive equation as

$$\tau(y) = \gamma(y)G_{ad} \tag{B.3}$$

The shearing strain in the adhesive can be related to the extensional displacements in the metal, $u_m(y)$, and the composite, $u_c(y)$, as

$$\gamma(y) = \frac{v_m(y) - v_c(y)}{t_{ad}} \tag{B.4}$$

Substituting equation (B.4) into equation (B.3) and that result into equation (B.2) yields

$$\frac{dF(y)}{dy} = \frac{G_{ad}w}{t_{ad}} [v_m(y) - v_c(y)] \tag{B.5}$$

Equation (B.5) can be differentiated with respect to y to yield

$$\frac{d^2F}{dy^2} = \frac{Gw}{t_{ad}} \left\{ \frac{dv_m(y)}{dy} - \frac{dv_c(y)}{dy} \right\} \tag{B.6}$$

when the derivatives of the extensional displacements u_m and u_c with respect to y are the extensional strains in the metal and composite adherends respectively. These strains were related to the extensional loads in the adherends by

$$\varepsilon_m = \frac{dv_m(y)}{dy} = \frac{F(y)}{wE_m t_m} \qquad \varepsilon_c = \frac{dv_c(y)}{dy} = \frac{P - F(y)}{wE_c t_c} \tag{B.7}$$

where E_M and E_c are the moduli of the metal and composite respectively. Substituting equations (B.7) into equation (B.6) yielded a second order, nonhomogeneous differential equation in $F(y)$ as

$$\frac{d^2F(y)}{dy} - \alpha F(y) = \beta \tag{B.8}$$

where

$$\alpha = \frac{G_{ad}}{t_{ad}} \left\{ \frac{1}{t_m E_m} + \frac{1}{t_c E_c} \right\}$$

and

$$\beta = \frac{-PG_{ad}}{wt_{ad}E_c t_c} = \frac{-sG_{ad}}{t_{ad}E_c}$$

where s is the stress in the composite and G_{ad} is the shear modulus of the composite.

Solving equation (B.8) yielded a complete solution as

$$F(y) = c_1 e^{\sqrt{\alpha}y} + c_2 e^{-\sqrt{\alpha}y} + \frac{\beta}{\alpha} \tag{B.9}$$

With referral to figure B.3a, the boundary conditions for equation (B.9) are

$$\begin{aligned} y = 0 \qquad & F(y) = F(0) = 0 \\ y = \infty \qquad & F(y) \text{ is bounded} \end{aligned} \tag{B.10}$$

With the use of these boundary conditions, the constants in equation (B.9) were found to be

$$c_1 = 0 \qquad c_2 = \frac{\beta}{\alpha}$$

Thus, equation (B.9) becomes

$$F(y) = \frac{swG_{ad}}{\alpha t_{ad} E_c} \left\{ 1 - e^{-\sqrt{\alpha}y} \right\} \tag{B.11}$$

By the use of equation (B.2), the shear stress in the adhesive was calculated from equation (B.11) as

$$\tau(y) = \frac{sG_{ad}w}{t_{ad}E_c\sqrt{\alpha}} \; e^{-\sqrt{\alpha}y} \qquad (B.12)$$

Finite Element Solution

A finite element computer program, PLANE, was used to calculate the shearing stresses in the adhesive layer in the specimen shown in figure B3.a. PLANE is an elastic-plastic, two-dimensional program which uses constant strain and linear strain triangular elements. PLANE was developed by the Grumman Aircraft Corporation for the National Aeronautics and Space Administration and was documented by Armen and Levy (1962). The mesh used for the analysis is shown on figure B.4 and contains 1,522 degrees of freedom. The triangles are predominately linear strain triangles which allow linear variations in the stresses and strains through the elements. Each of the adherends is modeled with several elements through the thickness thus allowing variations of extensional and shearing stresses through the thickness. In contrast, the one-dimensional analysis assumed uniform extensional stresses and no shearing stresses through the thickness of each adherend. The adhesive layer was modeled by one layer of elements which allowed linear variation in stresses through the adhesive thickness.

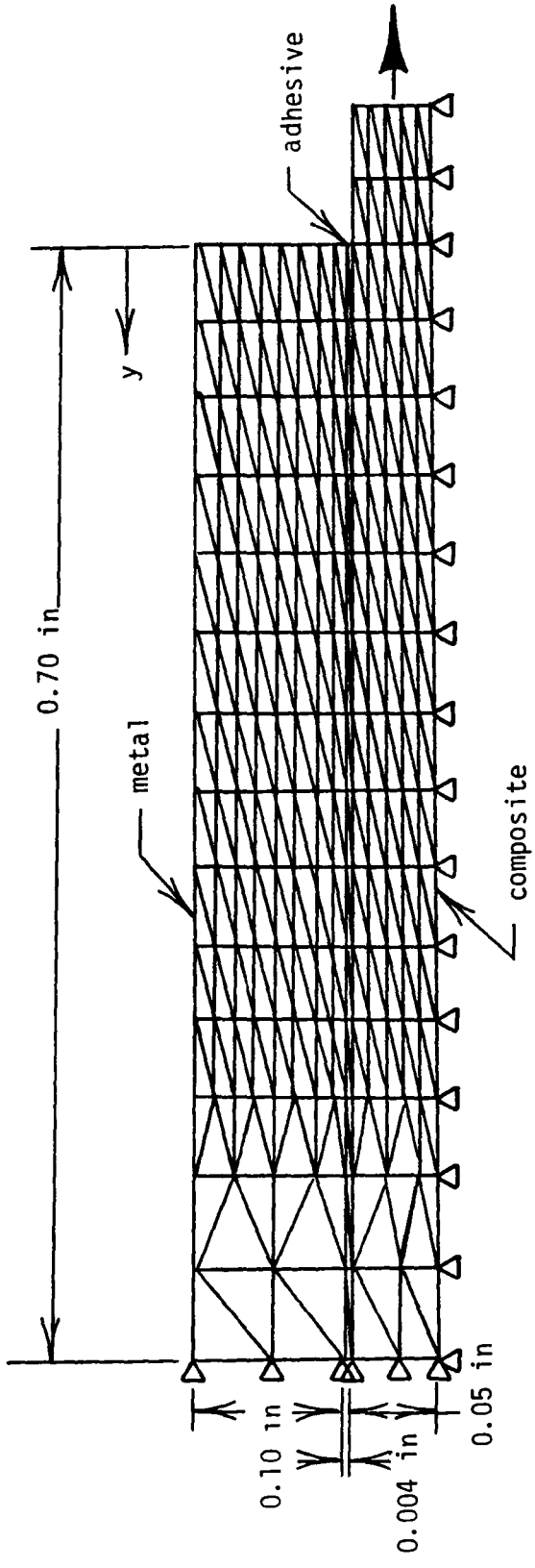

Fig. B.4. Finite element mesh

One-Dimensional Versus Finite Element Solution

To compare the results of the two solutions, the specimen configuration shown in figure B.3a with a width of $w = 1.0$ inch and the following parameters

	metal	adhesive	composite
thickness	$t_m = 0.1$ in	$t_{ad} = 0.004$ in	$t_c = 0.1$ in
moduli	$E_m = 10.3 \times 10^6$ psi	$G_{ad} = 215{,}000$ psi	$E_c = 30 \times 10^6$ psi

and an applied stress s of 1,000 psi was analyzed with both solutions. The parameters used in these solution were typical for constituents used in the reinforced system discussed in Chapter II. The adhesive shear stress calculated from the one-dimensional solution equation (B.12) was plotted as a solid line against y (distance from the edge of the metal adherend) on figure B.5. On the same figure the circles indicate values of the adhesive shear stress calculated from the finite element solution. As evident from the figure the one-dimensional solution gives shear stress values twice as high as those obtained from the finite element solution near the edge of the metal adherend ($y = 0$). Evidently, the shearing deformation of the adherends which was not accounted for in the one-dimensional solution has a significant effect on the values of the shear stresses.

To account for the adherend shear deformation and still use the simplified one-dimensional analysis, an effective shear modulus G_{eff}

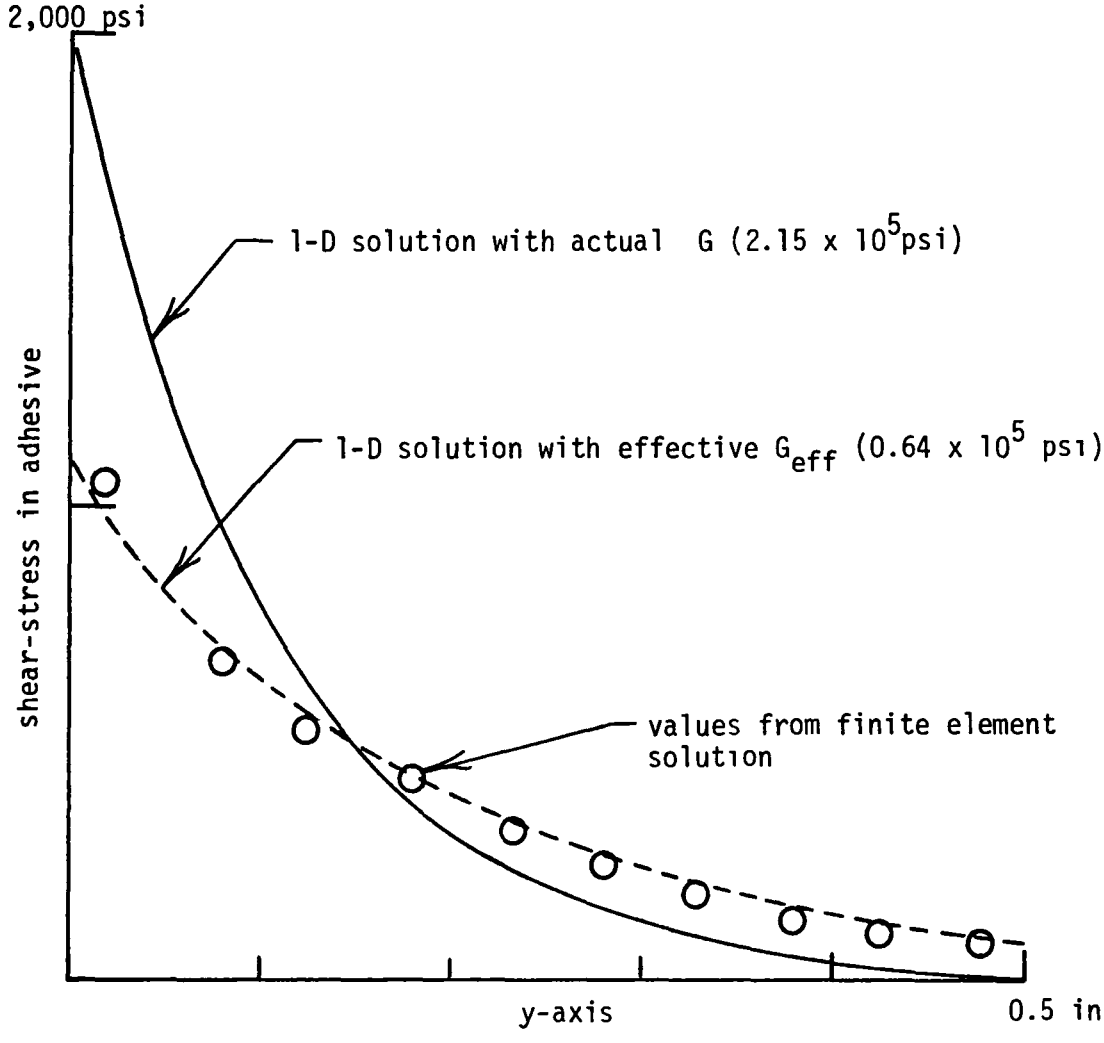

Fig. B.5. Finite element versus one-dimensional solution

was introduced. The magnitude of G_{eff} was determined by equating the maximum shear stresses in the adhesive calculated by the finite element solution to the expression for the maximum shear stress from the one-dimensional solution from equation (B.12) as

$$\tau_{\substack{max \\ Finite\ Element}} = \frac{sG_{ad}}{t_{ad}E_c\sqrt{\alpha}} \quad (y = 0) \tag{B.13}$$

Solving equation (B.13) for G yielded an expression for an effective shear modulus G_{eff} as

$$G_{eff} = \left\{\frac{\tau_{max_{(FE)}}E_c}{sw}\right\}^2 \left\{\frac{1}{t_mE_m} + \frac{1}{t_cE_c}\right\} \tag{B.14}$$

With this value for G in equation (B.12) yields a corrected one-dimensional solution for the adhesive shear stress as

$$\tau(y) = \frac{sG_{eff}we^{-\sqrt{\alpha}y}}{t_{ad}E_c\sqrt{\alpha}} \tag{B.15}$$

For the sample analysis, equation (B.14) yielded G_{eff} as 64,000 psi. Using this value for G_{eff}, equation (B.15) was plotted against y as a dashed line on figure B.5. The agreement between equation (B.15) and finite element results indicated by the circles on the figure is excellent. Consequently, the assumptions made in Chapter IV, that the adherends only undergo extensional deformation while the adhesive

only undergoes shear deformation, can be used to accurately predict shear stresses in the adhesive with a simplified analysis if an effective shear modulus for the adhesive is used in the calculations.

For analysis of the reinforced system shown in figure 2 the effective modulus was determined for a range of adherend thicknesses for the adhesive used in the reinforced system both for before and after the adhesive yields. To determine the values of effective shear moduli numerous finite element solutions were run with different adherend thicknesses for both the initial bulk adhesive shear modulus of 215,000 psi and the bulk shear modulus after yielding of 74,000 psi. The results of these calculations are given in table B.1. In the table the maximum shear stress calculated from the finite element solution and the effective shear modulus are tabulated for the different adhesive thicknesses.

As shown in table B.1 the value of the effective modulus for the initial shear modulus of the adhesive does not vary much with adherend thicknesses. The average value for G_{eff} is about 65,000 psi and is within 3 percent of any of the calculated values.

Also, as shown in table B.1, the value of the effective modulus for shear modulus of the adhesive after yielding also has little variation with adherend thicknesses. The average value in this case is about 36,000 psi and is within 3.3 percent of any of the calculated values.

As evident from the previous discussion the reinforced system can be analyzed by assuming that the adherends only undergo extensional

deformation while the adhesive only undergoes shearing deformation if an effective shear modulus of 65,000 psi is used for the adhesive before the adhesive yields and an effective shear modulus of 36,000 psi is used for the adhesive after yielding.

TABLE B.1

EFFECTIVE SHEAR MODULI FOR REINFORCED SYSTEM

adhesive modulus 215,000 psi	composite thickness in		metal adherend thickness, inches			
			0.05	0.10	0.15	0.20
	0.025	τ_{max}, psi	754	887	957	1,003
		G_{eff}, psi	66,960	65,200	65,200	65,800
	0.050	τ_{max}, psi	841	1,049	1,169	1,251
		G_{eff}, psi	66,400	64,800	64,400	64,800
	0.075	τ_{max}, psi	876	1,124	1,278	1,389
		G_{eff}, psi	65,800	64,300	64,000	64,500
	0.10	τ_{max}, psi	897	1,171	1,347	1,479
		G_{eff}, psi	66,000	64,300	63,600	64,400
adhesive modulus 74,000 psi	composite thickness in					
	0.025	τ_{max}, psi	561	661	710	743
		G_{eff}, psi	37,100	36,200	35,900	36,100
	0.050	τ_{max}, psi	629	785	871	929
		G_{eff}, psi	37,100	36,300	35,900	35,800
	0.075	τ_{max}, psi	656	842	953	1,030
		G_{eff}, psi	36,900	36,100	35,700	35,500
	0.10	τ_{max}, psi	671	876	1,002	1,090
		G_{eff}, psi	36,840	36,000	35,400	35,000

APPENDIX C

REMOTE STRESSES IN THE ADHERENDS

For equilibrium to exist, the macroscopic stresses applied to the reinforced system must be balanced by the stresses in the adherends of the system. This relationship can be written in vector form as

$$\begin{bmatrix} s_x \\ s_y \\ s_{xy} \end{bmatrix}_{system} A = \begin{bmatrix} \sigma m_{xx} \\ \sigma m_{yy} \\ \sigma m_{xy} \end{bmatrix}_{metal} A_m + \begin{bmatrix} \sigma c_{xx} \\ \sigma c_{yz} \\ \sigma c_{xy} \end{bmatrix}_{composite} A_c \tag{C.1}$$

where A represents the area of the reinforced system and A_m and A_c represent the area of each element. For the case where stress was applied in only the y-direction,

$$\begin{aligned} s_x &= 0 \\ s_y &= \text{applied load}/A \\ s_{xy} &= 0 \end{aligned} \tag{C.2}$$

With strains uniform through the thickness, (C.1) can be rewritten for a unit width as

$$\begin{bmatrix} 0 \\ s_y \\ 0 \end{bmatrix} (t_m + t_c) = \begin{bmatrix} & & \\ & [C]t_m + [D]t_c & \\ & & \end{bmatrix} \begin{bmatrix} \varepsilon_x \\ \varepsilon_y \\ \varepsilon_{xy} \end{bmatrix} \tag{C.3}$$

where the C and D are the stiffness matrices for an isotropic and orthotropic material in plane stress, respectively, as given by Zienkiewicz (1971) as

$$[C] = \begin{bmatrix} \frac{E}{1-\nu^2} & \frac{\nu E}{1-\nu^2} & 0 \\ \frac{\nu E}{1-\nu^2} & \frac{E}{1-\nu^2} & 0 \\ 0 & 0 & G \end{bmatrix} \tag{C.4}$$

$$[D] = \begin{bmatrix} \frac{E_x}{E_y} & \frac{\nu_{yx}E_x}{E_y} & 0 \\ \frac{\nu_{yx}E_x}{E_y} & 1 & 0 \\ 0 & 0 & \frac{G_{yx}}{E_y}\left(1 - \frac{E_x}{E_y}\nu_{yx}^2\right) \end{bmatrix} \frac{E_y}{1 - \frac{E_x}{E_y}\nu_{yx}^2} \tag{C.5}$$

with E, G_{yx}, and ν_{yx} denoting the extensional modulus, the shear modulus, and Poisson's coefficient respectively. With simple matrix algebra, equation (C.3) can be solved and the strains determined. These strains in turn can be used with the appropriated stiffness matrices to calculate the stresses in the metal and composite adherends as

$$\begin{bmatrix} \sigma m_{xx} \\ \sigma m_{yy} \\ \sigma m_{xy} \end{bmatrix} = [C] \begin{bmatrix} \varepsilon m_{xx} \\ \varepsilon m_{yy} \\ \varepsilon m_{xy} \end{bmatrix} \tag{C.6}$$

$$\begin{bmatrix} \sigma c_{xx} \\ \sigma c_{yy} \\ \sigma c_{xy} \end{bmatrix} = [D] \begin{bmatrix} \varepsilon c_{xx} \\ \varepsilon c_{yy} \\ \varepsilon m_{xy} \end{bmatrix} \tag{C.7}$$

APPENDIX D

GREEN'S FUNCTION FOR THE CRACKED SHEET

The solutions for the interlaminar stresses and the strain energy release at the debond front developed in Chapters IV and V respectively require Green's functions for both displacements and stresses. As pointed out by Dennemeyer (1968), the solution for a concentrated load acting on a body can be used as a Green's function.

Herein, the solution for four concentrated loads that are symmetric with respect to a crack in an isotropic sheet was developed. The solution was based on elasticity theory using complex variable theory as developed by Muskhelishvili (1975). The solution was predicted on the assumptions that the cracked sheet is infinite isotropic, and can be described by a plane stress or strain analysis. As shown by Muskhelishvili (1975), both the stresses and displacements in a cracked sheet can be expressed in terms of two stress functions, $\Phi(z)$ and $\Psi z)$, as

$$\sigma_x = \text{Real}\{\Phi(z) + \overline{\Phi(z)} - [\bar{z}\Phi'(z) + \Psi(z)]\} \tag{D.1}$$

$$\sigma_y = \text{Real}\{\Phi(z) + \overline{\Phi(z)} + \bar{z}\Phi'(z) + \Psi(z)\} \tag{D.2}$$

$$\sigma_{xy} = \text{Imag}\{\bar{z}\Phi'(z) + \Psi(z)\} \tag{D.3}$$

$$2G(u + iv) = \eta\phi(z) - z\overline{\Phi'(z)} - \psi(z) \tag{D.4}$$

where σ_x, σ_y and σ_{xy} are stresses, u and v are displacements, the bar over the functions denotesthe complex conjugate, i is the square root of -1 and

$$\Phi(z) = \phi'(z) = \frac{d\phi(z)}{dz} \qquad \Psi(z) = \psi'(z) = \frac{d\psi(z)}{dz}$$

$$\eta = 3 - 4\nu \quad \text{plane strain}$$

$$\eta = \frac{3 - \nu}{1 + \nu} \quad \text{plane stress}$$

is the Poisson's ratio.

The stress functions, $\Phi(z)$ and $\Psi(z)$, for the cracked sheet under four concentrated loads as shown on figure D.1c were constructed by superimposing the stress functions for a cracked sheet under two different loading conditions. The first condition which is shown on figure D.1a has concentrated loads acting on the cracked sheet plus a stress distribution applied to the crack surface. This stress distribution was equal to the stress distribution which exists along the x-axis for an uncracked sheet with concentrated loads. This stress

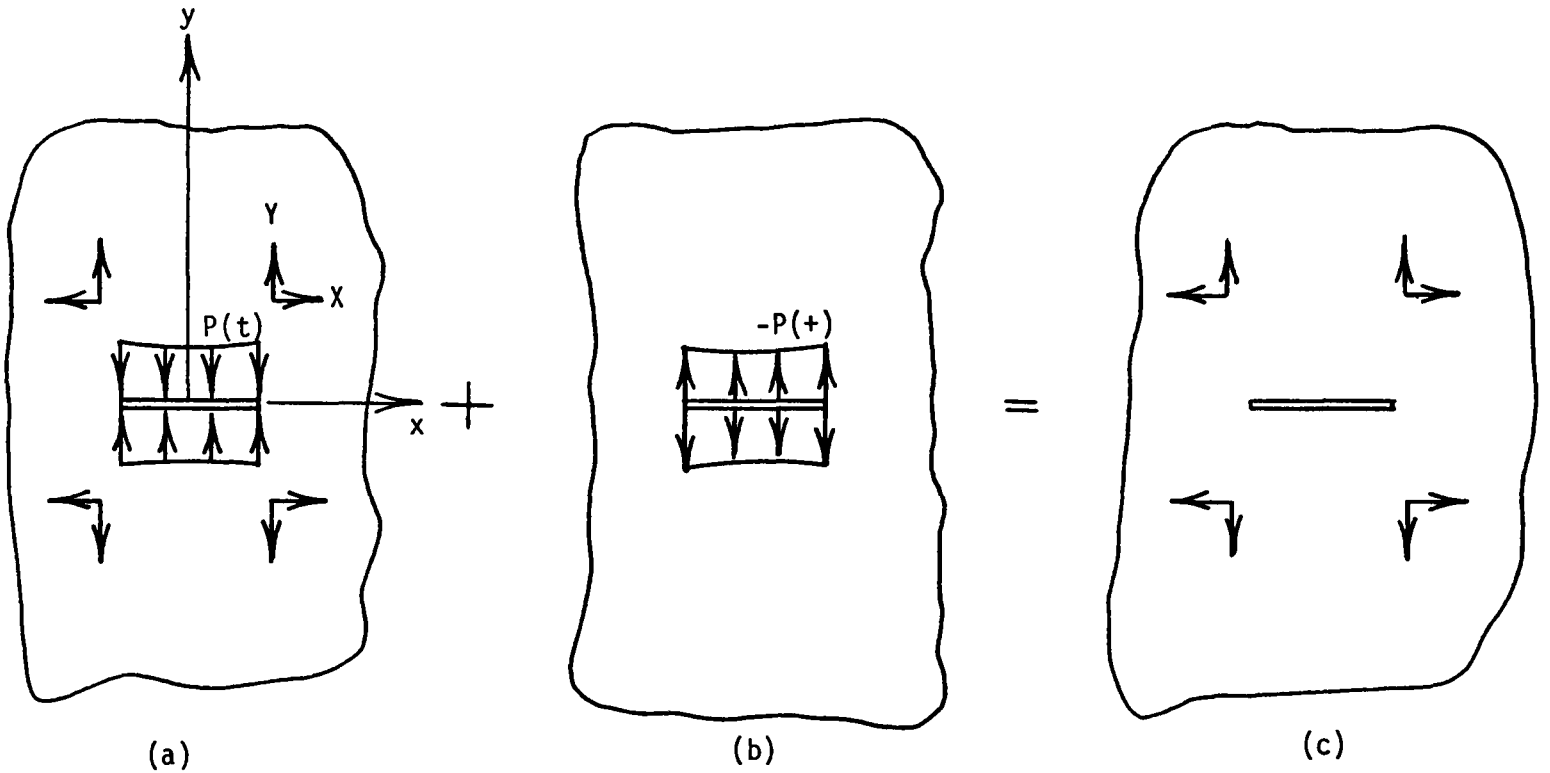

Fig. D.1. Superposition method used to formulate Green's functions for a cracked sheet

distribution closes the crack and, therefore, effectively eliminates it. As a result, figure D.1a represents an uncracked sheet with concentrated loads acting on it. The second condition which is shown on figure D.1b is for a stress distribution acting on the surface of a crack. This stress distribution has the same magnitude, but is of opposite sign to the stress distribtuion applied to the crack in the first condition. The development of the stress functions for these two conditions follows.

The stress functions for figure D.1a were developed by superimposing the solution for single concentrated forces that act in different quadrants. For a point, z_o, in the first quadrant the solution was given by Muskhelishvili (1975) as

$$\Phi(z) = -S \frac{1}{z - z_o} \qquad \Psi(z) = \bar{S}\eta \frac{1}{z - z_o} - S \frac{\bar{z}_o}{(z - z_o)^2} \tag{D.5}$$

where

$$S = \frac{X + iY}{2\pi(1 + \eta)t_m}$$

and X and Y are the load components in the x and y directions respectively, $\pi = 3.1459$, and t_m is the thickness of the sheet. Equations (D.5) were generated for the second, third and fourth

quadrants by replacing S and z_0 with $-\bar{S}$ and $-\bar{z}_0$, -S and $-z_0$, and $\bar{S}$ and $\bar{z}_0$ respectively. These stress functions were then superimposed to form the functions

$$\Phi(z) = S\left\{\frac{1}{z + z_0} - \frac{1}{z - z_0}\right\} + \bar{S}\left\{\frac{1}{z + \bar{z}_0} - \frac{1}{z - \bar{z}_0}\right\} \tag{D.6}$$

$$\Psi(z) = S\left\{\eta\left\{\frac{1}{z - \bar{z}_0} - \frac{1}{z + \bar{z}_0}\right\} - \bar{z}_0\left\{\frac{1}{(z - z_0)^2} + \frac{1}{(z + z_0)^2}\right\}\right\}$$

$$+ S\left\{\eta\left\{\frac{1}{z - z_0} - \frac{1}{z + z_0}\right\} - z_0\left\{\frac{1}{(z - \bar{z}_0)^2} + \frac{1}{(z + \bar{z}_0)^2}\right\}\right\} \tag{D.7}$$

where upon differentiation equation (D 6) becomes

$$\Phi'(z) = -S\left\{\frac{1}{(z + z_0)^2} - \frac{1}{(z - z_0)^2}\right\} - \bar{S}\left\{\frac{1}{(z + \bar{z}_0)^2} - \frac{1}{(z - \bar{z}_0)^2}\right\} \tag{D.8}$$

and upon integration equations (D.6) and (D.7) become

$$\phi(z) = S\,[\mathrm{Log}(z + z_0) - \mathrm{Log}(z - z_0)\,]$$

$$+ \bar{S}\,[\mathrm{Log}(z + \bar{z}_0) - \mathrm{Log}(z - \bar{z}_0)\,] \qquad (D.9)$$

$$\psi(z) = S\left\{\eta\left\{\mathrm{Log}(z - \bar{z}_0) - \mathrm{Log}(z + \bar{z}_0)\right\} + \bar{z}_0\left\{\frac{1}{z - z_0} + \frac{1}{z + z_0}\right\}\right\}$$

$$+ \bar{S}\left\{\eta\left\{\mathrm{Log}(z - z_0) - \mathrm{Log}(z + z_0)\right\} + z_0\left\{\frac{1}{z - \bar{z}_0} + \frac{1}{z + \bar{z}_0}\right\}\right\}$$

(D.10)

Equations (D.6) through (D.10) are the required stress functions, derivative, and integrals to compute stresses and displacements from equations (D.1) through (D.14) for figure D.1a.

The stress functions for load condition 2 shown on figure D.1b were obtained in the following manner. Following Muskhelishvili (1975), a new stress function $\Omega(z)$ was introduced which is related to the previously discussed stress function by the equation

$$\Psi(z) = \bar{\Omega}(z) - \Phi(z) - z\Phi'(z) \qquad (D.11)$$

where

$$\bar{\Omega}(z) = \overline{\Omega(\bar{z})}$$

The required stress functions, $\Phi(z)$ and $\Omega(z)$, can be determined for pressure acting on a single crack as (Muskhelishvili 1975)

$$\Phi_p(z) = \frac{1}{2\pi i I(z)} \int_{-a}^{a} \frac{I(t)P(t)dt}{t - z} + \frac{1}{2\pi i} \int_{-a}^{a} \frac{q(t)dt}{t - z} \qquad (D.12)$$

$$\Omega_p(z) = \frac{1}{2\pi i I(z)} \int_{-a}^{a} \frac{I(t)P(t)dt}{t - z} - \frac{1}{2\pi i} \int_{-a}^{a} \frac{q(t)dt}{t - z} \qquad (D.13)$$

with

$$I(z) = \sqrt{z^2 - a^2} \qquad a = \frac{\text{crack length}}{2}$$

and

$$P(t) = \frac{1}{2} (\sigma_y^+ + \sigma_y^-) - \frac{i}{2} (T_{xy}^+ - T_{xy}^-)$$

$$q(t) = \frac{1}{2} (\sigma_y^+ - \sigma_y^-) - \frac{i}{2} (T_{xy}^+ - T_{xy}^-) \qquad (D.14)$$

σ_y and T_{xy} are normal and shearing stresses acting on the crack surfaces respectively (the plus sign indicates the upper surface of the crack while the minus sign indicates the lower surface.) P(t)

and $q(t)$ are total normal and shearing pressures which act on the crack surfaces. As mentioned previously, the stresses which acts on the crack surface in figure D.1b is equal to the magnitude but of opposite sign to the stress caused by four point loads acting on an uncracked sheet. Therefore, the functions, $\Phi(z)$ and $\Psi(z)$, shown in equations (D.6) and (D.7), which are solutions for point loads on a continuous sheet, can be used to find $P(t)$ and $q(t)$.

The normal and shearing stresses acting on the crack were calculated (Muskhelishvili 1975) in terms of equations (D.6), (D.7), and (D.8), as

$$\sigma_y - i\tau_{xy} = \Phi(z) + \overline{\Phi(z)} + z\overline{\Phi'(z)} + \overline{\Psi(z)} \tag{D.15}$$

Substituting equations (D.6), (D.7), and (D.8) into equation (D.15) yields

$$\sigma_y - i\tau_{xy} = \alpha(z,z_0) + \overline{\alpha(z,z_0)} \tag{D.16}$$

or

$$\sigma_y - i\tau_{xy} = 2\text{Real}\ (\alpha(z,z_0)) \tag{D.17}$$

where

$$\alpha(z,z_0) = S\left\{\frac{-4z_0}{z^2 - z_0^2} - \frac{z + \bar{z}_0}{(z + z_0)^2} + \frac{z - \bar{z}_0}{(z - z_0)^2} + \frac{2\eta\bar{z}_0}{z^2 - \bar{z}_0^2}\right\} \tag{D.18}$$

Equation (D.16) shows that no imaginary term exists. Consequently, T_{xy} is zero. Also, σ_y has the same value along the x-axis independent of the direction in which the x-axis is approached. Consequently, $\sigma_y^+ = \sigma_y^-$. Therefore, with consideration given to the above statements and equations (D.14), the total pressures on the crack are

$$P(t) = \alpha(t,z_0) + \overline{\alpha(t,z_0)}$$

$$q(t) = 0 \tag{D.19}$$

As a result of the above simplifications, equations (D.12) and (D.13) become equal to each other and are expressed as

$$\Phi(z) = \Omega(z) = \frac{1}{2\pi i I(z)} \int_{-a}^{a} \frac{I(t)P(t)}{t - z}\, dt \tag{D.20}$$

The integral in equation (D.20) was evaluated by contour integration along the contour shown in figure D.2 by using the Residue theorem given as (Wylie 1960)

$$\int_c f(z)dz = 2\pi i \, \Sigma \text{ Residues} \tag{D.21}$$

where the residue for simple poles is given as

$$\text{Residue} = \frac{1}{(M-1)!} \lim_{z \to a} \left\{ \frac{d^{M-1}}{d^{M-1}} (z - a)^M f(z) \right\} \tag{D.22}$$

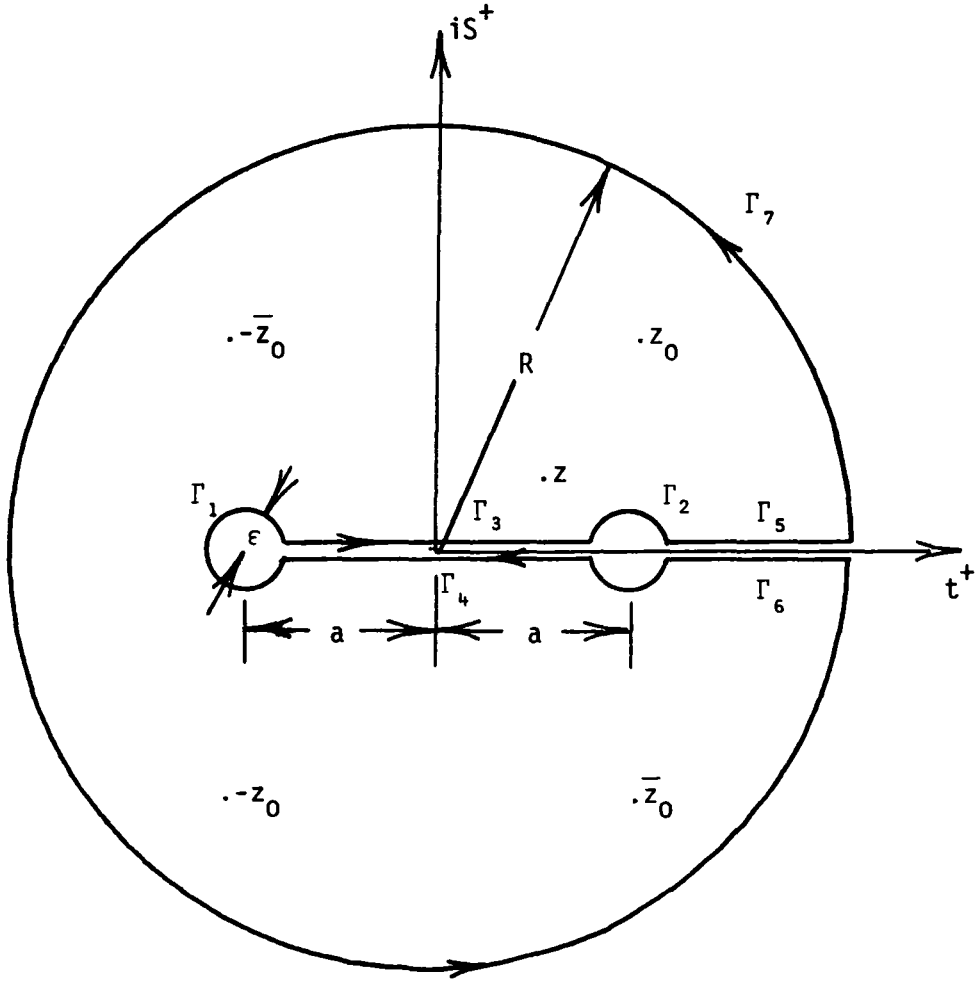

Fig. D.2. Path for contour integration

The contour shown in figure D.2 can be broken into several sections. Thus, equation (D.19) becomes

$$\int_{\Gamma_1} A(\zeta) + \int_{\Gamma_2} A(\zeta) + \int_{\Gamma_3} A(\zeta) - \int_{\Gamma_4} A(\zeta) + \int_{\Gamma_5} A(\zeta)$$

$$- \int_{\Gamma_6} A(\zeta) + \int_{\Gamma_7} A(\zeta) = 2\pi i \, \Sigma \, \text{Res} \qquad \text{(D.23)}$$

where

$$A(\zeta) = \frac{\sqrt{\zeta^2 - a^2}\, P(\zeta)}{\zeta - z} \, d\zeta, \qquad \zeta = t + iS$$

On figure D.2 the integral is evaluated along the contour as R approaches infinity and ε approaches zero. Each of the contours can be expressed as follows.

$$\int_{\Gamma_1} A(\zeta) = \lim_{\varepsilon \to 0} \int \frac{I(\zeta)\, P(\zeta)}{\zeta - z} \, d\zeta$$

$$\text{Let} \quad \zeta + a = \varepsilon e^{i\Theta} \qquad d\zeta = i\varepsilon e^{i\Theta} d\Theta$$

$$\therefore \int_{\Gamma_1} A(\zeta) = \lim_{\varepsilon \to 0} \int_{2\pi}^{0} \frac{i\varepsilon \sqrt{\varepsilon^2 e^{i\Theta} - 2a\varepsilon e^{i\Theta}}\, P(\varepsilon e^{i\Theta} - a) e^{i\Theta} d\Theta}{\varepsilon e^{i\Theta} - a - z}$$

(D.24)

likewise for Γ_2 let $\zeta - a = \varepsilon e^{i\theta}$

$$\therefore \int_{\Gamma_2} A(\zeta) = \lim_{\varepsilon \to 0} \int_{\pi}^{-\pi} \frac{i\varepsilon \sqrt{\varepsilon^2 e^{i\theta} + 2a\varepsilon e^{i\theta}}\, P(\varepsilon e^{i\theta} + a) e^{i\theta} d\theta}{\varepsilon e^{i\theta} + a - z} \tag{D.25}$$

for Γ_3

$$\int_{\Gamma_3} A(\zeta) = \int_{-a}^{a} \frac{\overset{+}{I}(t)\, P(t)dt}{t - z} \tag{D.26}$$

likewise

$$\int_{\Gamma_4} A(\zeta) = \int_{-a}^{a} \frac{\overset{-}{I}(t)\, P(t)dt}{t - z} = - \int_{-a}^{a} \frac{\overset{-}{I}(t)\, P(t)}{t - z} dt \tag{D.27}$$

Noting that Muskhelishvili (1975) showed that $\overset{-}{I}(t) = -\overset{+}{I}(t)$ for $\zeta < a$, equations (D.26) and (D.27) can be combined to give the integral on the left hand side of equation (D.20) as

$$\int_{\Gamma_3} A(\zeta) = \int_{\Gamma_4} A(\zeta) = 2\int_{-a}^{a} \frac{\overset{+}{I}(t)\, P(t)dt}{t - z} \tag{D.28}$$

Noting that

$$\overset{+}{I}(t) = \overset{-}{I}(t) \quad \text{for } \zeta > a$$

the sum of the next two segments of the contour integral equals zero, because

$$\int_{\Gamma_5} A(\zeta) = \int_a^R \frac{\overset{+}{I}(t)\, P(t)dt}{t - z} \qquad \int_{\Gamma_6} A(\zeta) = \int_R^a \frac{\overset{+}{I}(t)\, P(t)dt}{t - z}$$

so that

$$\int_{\Gamma_5} A(\zeta) + \int_{\Gamma_6} A(\zeta) = 0 \tag{D.29}$$

The last contour segment can be evaluated as

$$\int_{\Gamma_7} A(\zeta) = \lim_{R \to \infty} \int \frac{I(\zeta)\, P(\zeta)d\zeta}{\zeta - z}$$

Let $\zeta = Re^{i\Theta}, d\zeta = Rie^{i\Theta}d\Theta$

$$\therefore \int_{\Gamma_7} A(\zeta) = \lim_{R \to \infty} \int_0^{2\pi} \frac{Ri\sqrt{R^2e^{2i\Theta} - a^2}\, P(Re^{i\Theta})d\Theta}{Re^{i\Theta} - z} \tag{D.30}$$

Substituting equations (D.24), (D.25), (D.28), (D.29), and (D.30) into equation (D.23) and rearranging the terms yield the desired integral as

$$\int_{-a}^{a} \frac{I(t)\,P(t)dt}{t - z} = \pi i \,\Sigma\,\text{Residues} - \lim_{\varepsilon \to 0} \frac{1}{2} \int_{2\pi}^{0} \frac{i\varepsilon\sqrt{\varepsilon^2 e^{i\theta} - 2a\varepsilon e^{i\theta}}\,P(\varepsilon e^{i\theta} - a)d\theta}{\varepsilon e^{i\theta} - a - z}$$

$$- \lim_{\varepsilon \to 0} \frac{1}{2} \int_{\pi}^{-\pi} \frac{i\varepsilon\sqrt{\varepsilon^2 e^{i\theta} + 2a\varepsilon e^{i\theta}}\,P(\varepsilon e^{i\theta} - a)e^{i\theta}d\theta}{\varepsilon e^{i\theta} + a - z}$$

$$- \lim_{R \to \infty} \frac{1}{2} \int_{0}^{2\pi} \frac{Ri\sqrt{R^2 e^{2i\theta} - a^2}\,P(Re^{i\theta})d\theta}{Re^{i\theta} - z} \qquad \text{(D.31)}$$

where $P(t)$ is given by equation (D.19). As an example, equation (D.31) was calculated for the first term of $P(t)$. For this case the expression to consider was chosen as

$$\frac{I(\zeta)\,P_1(\zeta)}{\zeta - z} = \frac{-4I(\zeta)\,Sz_o}{(\zeta^2 - z_o^2)(\zeta - z)}, \quad P_1(t) = \frac{-4Sz_o}{(t^2 - z_o^2)(t - z)}$$

(D.32)

The residuals for expression (D.32) were calculated with equation (D.22). They become

$$\text{Residuals} = S\left\{\lim_{\zeta \to z_0}\left\{\frac{-4I(\zeta)z_0}{(\zeta + z_0)(\zeta - z)}\right\}\right.$$

$$+ \lim_{\zeta \to -z_0}\left\{\frac{-4I(\zeta)z_0}{(\zeta - z_0)(\zeta - z)}\right\}$$

$$\left.+ \lim_{\zeta \to z}\left\{\frac{-4I(\zeta)z_0}{(\zeta - z_0)(\zeta + z_0)}\right\}\right\} \qquad \text{(D.33)}$$

To insure single valuedness of the stress functions, values of $I(\zeta)$ must be chosen so that they lie on the same branch. Values of $I(\zeta)$ will lie on the same branch for all values for ζ if

$$\lim_{\zeta \to \infty} \frac{I(\zeta)}{\zeta} = 1 \qquad \text{(D.34)}$$

The two possible values of $I(\zeta)$ are the complex numbers w_0 and $-w_0$. Hence, equation (D.34) requires that $I(z_0)$ equals w_0 and that $I(-z_0)$ equals $-w_0$, or simply that $I(z_0) = -I(-z_0)$. With the proper values of $I(\zeta)$ defined according to equation (D.34), equation (D.33) reduces to

$$\text{Residual} = -\frac{4S}{z_0^2 - z^2}\,(zI(z_0) - z_0 I(z)) \qquad (D.35)$$

In order to evaluate equation (D.31) the limits of three integrals must be taken. The first two integrals involve limits as $\varepsilon \to 0$ (equations (D.24) and (D.25)). The evaluation of these limits is similar for both equations. The limits can be obtained by rearranging the terms in the integrand so that they can be expressed by a simple binomial series as

$$(x + y)^n = x^n + nx^{n-1}y + \frac{n(n-1)}{2!}\,x^{n-2}y^2 \ldots (y^2 < x^2) \qquad (D.36)$$

or

$$(1 \pm x)^{-1} = 1 \mp x \mp x^2 + x^3 + \ldots \qquad (x^2 < 1) \qquad (D.37)$$

With the use of the first term of $P(t)$ as shown in (D.32), as an example (D.24) can be expressed

$$\int_{\Gamma_1} A(\zeta) = \lim_{\varepsilon \to 0} S \int_{2\pi}^{0} \frac{-4z_0 i\varepsilon \sqrt{\varepsilon^2 e^{2i\Theta} - 2a\varepsilon e^{i\Theta}}\, e^{i\Theta} d\Theta}{(\varepsilon e^{i\Theta} - a + z_0)(\varepsilon e^{i\Theta} - a - z_0)(\varepsilon e^{i\Theta} - a - z)} \qquad (D.38)$$

The term $\sqrt{\varepsilon e^{2i\theta} - 2a\varepsilon e^{i\theta}}$ in equation (D.39) can be expressed in terms of equation (D.36) as

$$\sqrt{\varepsilon e^{2i\theta} - 2a\, e^{i}} = \sqrt{\varepsilon}\, e^{\frac{i\theta}{2}} \sqrt{\varepsilon e^{i\theta} - 2a}$$

$$= i\sqrt{\varepsilon 2a}\, e^{i\theta/2} \left(1 - \frac{\varepsilon e^{i\theta}}{2a}\right)^{\frac{1}{2}}$$

$$= i\sqrt{\varepsilon 2a}\, e^{i\theta/2} \left\{1 - \frac{\varepsilon e^{i\theta}}{4a} - \frac{\varepsilon^2 e^{2i\theta}}{32a^2} \ldots\right\} \qquad \text{(D.39)}$$

while the term $(\varepsilon e^{i\theta} - a + z)^{-1}$ can be expressed in terms of equation (D.37) as

$$\frac{1}{\varepsilon e^{i\theta} - a + z_o} = \frac{1}{z_o - a\left\{\frac{\varepsilon e^{i\theta}}{z_o - a} + 1\right\}}$$

$$= \frac{1}{z_o - a}\left\{1 - \frac{\varepsilon e^{i\theta}}{z_o - a} + \frac{\varepsilon^2 e^{2i\theta}}{(z_o - a)^2} \cdots\right\}$$

(D.40)

Substituting equations (D.39), (D.40) and similar expressions for the remaining terms in the denominator of equation (D.38) into equation (D.38) yields an expression as

$$\lim_{\varepsilon \to 0} - 4z_o \int_{2\pi}^{0} i\varepsilon^2 \sqrt{\varepsilon 2a}\, e^{\frac{i\theta}{2}} \left\{1 + \frac{\varepsilon e^{i\theta}}{4a} \cdots\right\}\left\{\frac{1}{z_o - a}\right\}\left\{1 - \frac{\varepsilon e^{i\theta}}{z_o - a} \cdots\right\}$$

$$\left\{\frac{-1}{z_o + a}\right\}\left\{1 + \frac{\varepsilon e^{i\theta}}{z_o + a} \cdots\right\}\left\{\frac{-1}{z + a}\right\}\left\{1 + \frac{\varepsilon e^{i\theta}}{z + a} \cdots\right\} e^{i\theta} d\theta \qquad (D.41)$$

whose limit is zero. Equation (D.25) can be evaluated by similar means. The result for $P(t)$ as shown by (D.32) is also zero.

Equation (D.30) can also be evaluated by a limiting process and by the use of equations (D.36) and (D.37) as $R \to \infty$. For this case, the integrand has to be arranged in a manner that makes the expansions for equation (D.36) and (D.37) valid for large values of R. For example, for the first term of $P(t)$ as given by (D.37), equation (D.30) can be expressed as

$$\lim_{R \to \infty} -4z_0 \int_0^{2\pi} \frac{i\left\{1 - \frac{a^2}{R^2 e^{2i\Theta}}\right\}^{\frac{1}{2}} d\Theta}{Re^{i\Theta}\left\{1 - \frac{z_0^2}{R^2 e^{2i\Theta}}\right\}\left\{1 - \frac{1}{Re^{i\Theta}}\right\}} = \int_{\Gamma_7} A(\zeta) \qquad (D.42)$$

By substituting the appropriate expansions for the terms in the integrand of equation (D.42), the limit as R increases without bound gives the value of equation (D.42) as zero.

Similarly, equation (D.31) can be evaluated for all terms of $P(t)$ contained in equation (D.19). All of these terms were combined, simplified, and substituted into equation (D.20) to yield

$$\Phi(z,z_0) = \Omega(z,z_0) = S\, B(z,z_0) + \bar{S}\, B(z,\bar{z}_0) \qquad (D.43)$$

where

$$B(z,z_0) = \frac{1}{2}\left\{\frac{-4z_0}{z^2 - z_0^2} + \frac{2\eta\bar{z}_0}{z^2 - \bar{z}_0^2} + \frac{z - \bar{z}_0}{(z - z_0)^2} - \frac{z + \bar{z}_0}{(z + z_0)^2}\right\}$$
$$+ \frac{z_0 - \bar{z}_0}{2I(z_0)I(z)}\left\{\frac{a^2 - zz_0}{(z_0 - z)^2} - \frac{a^2 + zz_0}{(z_0 + z)^2}\right\}$$
$$- \frac{z}{I(z)}\left\{\frac{I(z_0)}{z_0^2 - z^2} - \frac{\eta I(\bar{z}_0)}{\bar{z}_0^2 - z^2}\right\} \qquad (D.44)$$

A

With the use of equation (D.43), which shows $\Phi(z)$ and $\Omega(z)$ to be equal, and equation (D.11), $\Psi'(z)$ was expressed as

$$\Psi(z) = \overline{\Phi(\bar{z})} - \Phi(z) - z\Phi'(z) \tag{D.45}$$

where $\Phi(z)$ is given by right hand side of equation (D.43). To evaluate equation (D.45), the derivative of $\Phi(z)$ was required. Hence, the derivative of $B(z,z_0)$ was required because

$$\Phi'(z) = \frac{d\Phi(z)}{dz} = SB'(z,z_0) + \bar{S}B'(z,\bar{z}_0) \tag{D.46}$$

Using a symbolic manipulation system, MACSYMA (1975), written in LISP programming language, the derivative of $B(z,z_0)$ was found to be

$$B'(z,z_0) = -2z \left\{ \frac{\eta \bar{z}_0}{(z^2 - \bar{z}_0^2)^2} + \frac{3z_0^2\bar{z}_0 + z^2\bar{z}_0 - 4z_0^3}{(z_0 - z)^3 (z_0 + z)^3} \right\}$$

$$- \frac{1}{I(z)} \left\{ \frac{1}{z^2 - a^2} \left\{ \frac{\eta I(\bar{z}_0)(a^2\bar{z}_0^2 - 2z^4 + a^2z^2)}{(\bar{z}_0^2 - z^2)^2} \right.\right.$$

$$\left.\left. - \frac{I(z_0)(a^2z_0^2 - 2z^4 + a^2z^2)}{(z_0^2 - z^2)^2} \right\}\right.$$

A

$$+ \frac{z_o - \bar{z}_o}{2I(z_o)} \left\{ \frac{z_o^2 + zz_o - 2a^2}{(z_o - z)^3} + \frac{z_o^2 - zz_o - 2a^2}{(z_o + z)^3} \right.$$

$$\left. + \frac{z}{z^2 - a^2} \left\{ \frac{a^2 - zz_o}{(z_o - z)^2} - \frac{zz_o + a^2}{(z_o + z)^2} \right\} \right\} \tag{D.47}$$

To complete the evaluation of the functions used in equations (D.1) through (D.4) for pressure acting on the crack surface, the integrals of $\Phi(z)$ and $\Psi(z)$ given by $\phi(z)$ and $\psi(z)$ respectively were determined. As shown by equation (D.45), once $\phi(z)$ is found $\psi(z)$ is also determined. To evaluate $\phi(z)$ by integrating (D.43) the integral of $B(z,z_o)$ was determined (evaluation of the integral of $B(z,\bar{z}_o)$ is the same as for the integral of $B(z,z_o)$ except that z_o is replaced by $\bar{z}_o$).

Many of the terms in $B(z,z_o)$ are easy to integrate by using standard rules of calculus. However, those terms which contain $I(z)$ in the denominator require some rearrangement before the integration is attempted. For example, integrals of the type

$$II(z) = \int \frac{dz}{I(z)(z_o - z)} \tag{D.48}$$

appear frequently and were integrated as follows. First, a change of variables was made by letting

$$z = a\sin\theta, \quad dz = a\cos\theta d\theta$$

With the restriction that $|z| \leq a$, equation (D.48) became

$$II(z) = \int \frac{dz}{I(z)(z_0 - z)} = \int \frac{a\cos\theta d\theta}{I(z)(z_0 - a\sin\theta)} \qquad (D.49)$$

Next, the trigonometric relation $\sin^2\theta + \cos^2\theta = 1$ was used to express $\cos\theta$ as

$$\cos\theta = \frac{\sqrt{a^2 - z^2}}{a} \qquad (D.50)$$

At this point care must be taken to choose the correct value of the multi-valued function. The correct value was assured by requiring equation (D.34) to hold. For example, $I(z)$ can be written as

$$I(z) = \sqrt{z^2 - a^2} = i\sqrt{a^2 - z^2} \quad \text{or} \quad -i\sqrt{a^2 - z^2}$$

but according to equation (D.34)

$$\lim_{z \to \infty} \frac{\sqrt{z^2 - a}}{z} = 1 \quad \therefore \quad \lim_{z \to \infty} \frac{\pm i\sqrt{a^2 - z^2}}{z} = 1$$

so then

$$I(z) = - i\sqrt{a^2 - z^2} \quad \text{or} \quad \sqrt{a^2 - z^2} = iI(z) \tag{D.51}$$

Substituting equation (D.51) into equation (D.40) and that result into equation (D.49) yields the result

$$\int \frac{dz}{I(z)(z_0 - z)} = i \int \frac{d\Theta}{z_0 - a\sin\Theta} \tag{D.52}$$

which can be integrated by using standard integral tables. Burlington (1973) gives the value of the integral in (D.52) as

$$\int \frac{d\Theta}{z_0 - a\sin\Theta} = \frac{-1}{\sqrt{a^2 - z_0^2}} \text{Log}\left\{\frac{-a + z_0\sin\Theta + \sqrt{a^2 - z_0^2}\cos\Theta}{z_0 - \sin\Theta}\right\} \tag{D.53}$$

Making the appropriate substitutions of

$$\sin\Theta = z/a$$

$$\cos\Theta = iI(z)/a$$

$$\sqrt{a^2 - z_0^2} = iI(z_0)$$

gives the result of (D.48) as

$$\int \frac{dz}{I(z)(z_0 - z)} = -\frac{1}{\sqrt{z_0^2 - a^2}} \text{Log} \left\{ \frac{-a^2 + zz_0 - I(z_0)I(z)}{a(z_0 - z)} \right\} \tag{D.54}$$

The development of equation (D.54) was restricted to values of $|z| \leq a$. However, for values of $|z| > a$ the substitution $z = a\text{CSC}\,\Theta$ can be made and a similar process repeated. The results of this integration are identical to equation (D.54). Consequently, equation (D.54) is valid for all values of z (the same can be shown to be true for all values of z_0).

After much labor and simplification the integral of $B(z,z_0)$ was found to be

$$BI(z,z_0) = \frac{1}{2} \left\{ \text{Log}(z + z_0) - \text{Log}(z_0 - z) + \eta \left\{ \text{Log}(\bar{z}_0 - z) - \text{Log}(z + \bar{z}_0) \right\} + \frac{2(\bar{z}_0 - z_0)}{z^2 - z_0^2} \left\{ z - z_0 \frac{I(z)}{I(\bar{z}_0)} \right\} + XI(z,z_0) - \eta XI(z,\bar{z}_0) \right\} \tag{D.55}$$

where

$$XI(z,z_0) = \text{Log} \left\{ \frac{(zz_0 - a^2 - I(z)I(z_0))(z_0 + a)}{(zz_0 + a^2 - I(z)I(z_0))(z_0 - z)} \right\}$$

Therefore, integration of equation (D.43) can be expressed as

$$\phi(z,z_0)=\omega(z,z_0) = \int\Phi(z,z_0)dz = \int\Omega(z,z_0)dz = SBI(z,z_0) + \overline{S}BI(z,\overline{z}_0) \tag{D.56}$$

By integrating equation (D.45), $\psi(z)$ can be expressed in terms of equation (D.56) as

$$\psi(z) = \overline{\phi}(z) - z\Phi(z) \tag{D.57}$$

Therefore, in summary, the functions required to evaluate equations (D.1) through (D.4) for the cracked metal sheet which has a stress applied to the crack surface (equal in magnitude but of opposite sign to the stress along the crack line for a solid sheet) are given by the equations (D.43), (D.45), (D.56), and (D.57).

Green's Functions for Stress

As mentioned previously, the solution for the cracked sheet is obtained from superposition of the stresses from the two loading conditions shown on figure D.1a and D.1b. The stress functions for these two loading conditions, which were developed in the previous sections, were used to obtain the stresses in each loading condition. The stresses for the two conditions were then added to form the Green's function for stresses for the loading condition shown in figure D.1c.

The stress state for four point loads acting on a solid sheet shown on figure D.1a was found by substituting equation (D.6), (D.7), and (D.8) into equations (D.1), (D.2), and (D.3). The result is, in terms of the coefficients of the X and Y point loads:

$$\sigma_x = \text{Real}\{G1 - G2 - G3\}X + \text{Real}\{G1A - i(G2 - G3)\}Y$$

$$\sigma_y = \text{Real}\{G1 + G2 + G3\}X + \text{Real}\{G1A + i(G2 - G3)\}Y \qquad \text{(D.58)}$$

$$\sigma_{xy} = \text{Img}\{G1 + G2 + G3\}X + \text{Img}\{G1A + i(G2 - G3)\}Y$$

where

$$G1 = \frac{\text{Real}}{2\pi(1+\eta)t_m}\left\{\frac{-2z_o}{z^2 - z_o^2} - \frac{2\bar{z}_o}{z^2 - \bar{z}_o^2}\right\} \qquad \text{(D.59)}$$

$$G1A = \frac{\text{Real}}{2\pi(1+\eta)t_m}\left\{i\left\{\frac{-2z_o}{z^2 - z_o^2} + \frac{2\bar{z}_o}{z^2 - \bar{z}_o^2}\right\}\right\} \qquad \text{(D.60)}$$

$$G2 = \frac{1}{2\pi(1+\eta)t_m}\left\{\frac{2\eta\bar{z}_o}{z^2 - \bar{z}_o^2} - \left\{\frac{\bar{z}_o + \bar{z}}{(z + z_o)^2} + \frac{\bar{z}_o - \bar{z}}{(z - z_o)^2}\right\}\right\} \qquad \text{(D.61)}$$

$$G3 = \frac{1}{2\pi(1+\eta)t_m}\left\{\frac{2\eta\bar{z}_o}{z^2 - \ell_o^2} - \left\{\frac{z_o + \bar{z}}{(z+\bar{z}_o)^2} + \frac{z_o - \bar{z}}{(z-\bar{z}_o)^2}\right\}\right\} \tag{D.62}$$

The stress state for the stress applied to the crack surface, as shown on figure D.1b, was found by substituting equations (D.43), (D.45), and (D.46) into equations (D.1), (D.2), and (D.3). After several algebraic manipulations, the result was found to be

$$\sigma_x = \text{Real}\{2G5 - G7\}\ X + \text{Real}\{2G6 - G8\}Y$$

$$\sigma_y = \text{Real}\{2G5 + G7\}\ X + \text{Real}\{2G6 + G8\}Y \tag{D.63}$$

$$\sigma_{xy} = \text{Img}\ \ (G7)\ \ X + \text{Img}\ (G8)\ Y$$

where

$$G5 = \frac{1}{2\pi(1+\eta)t_m}\left\{B(z,z_o) + B(z,\bar{z}_o)\right\} \tag{D.64}$$

$$G6 = \frac{i}{2\pi(1+\eta)t_m}\left\{B(z,z_o) - B(z,z_o)\right\} \tag{D.65}$$

$$G7 = \frac{(\bar{z} - z)}{2\pi(1+\eta)t_m}\left\{B'(z,z_o) + B'(z,\bar{z}_o)\right\} \tag{D.66}$$

$$G8 = \frac{i(\bar{z} - z)}{2\pi(1+\eta)t_m}\left\{B'(z,z_o) - B'(z,\bar{z}_o)\right\} \tag{D.67}$$

Superimposing the stresses from the two loading conditions by adding equations (D.58) and (D.63) and taking the coefficients of the X and Y loads for the different stresses yielded six Green's functions for stress as

$$GS_{xx} = \text{Real}\{G1 - G2 - G3 - 2G5 + G7\} \tag{D.68}$$

$$GS_{xy} = \text{Real}\{G1A - i(G2 - G3) - 2G6 + G8\} \tag{D.69}$$

$$GS_{yx} = \text{Real}\{G1 + G2 + G3 - 2G5 - G7\} \tag{D.70}$$

$$GS_{yy} = \text{Real}\{G1A + i(G2 - G3) - 2G6 - G8\} \tag{D.71}$$

$$GS_{(xy)x} = \text{Img}\{G1 + G2 + G3 - G7)\} \tag{D.72}$$

$$GS_{(xy)y} = \text{Img}\{G1A + i(G2 - G3 - G8)\} \tag{D.73}$$

where the first index on GS indicates the stress and the second indicates the load responsible for it. For example, GS_{yx} indicates the σ_y stress at point z due to a unit load applied in the x-direction at point z_0.

The Green's functions given by equations (D.68) through (D.73) were verified with the use of a finite element program developed by Y. K. Cheung and I. P. King and documented in Zienkiewicz's book (1971). The finite element model used for the test case is shown in figure D.3. Because of symmetry only the first quadrant of the cracked

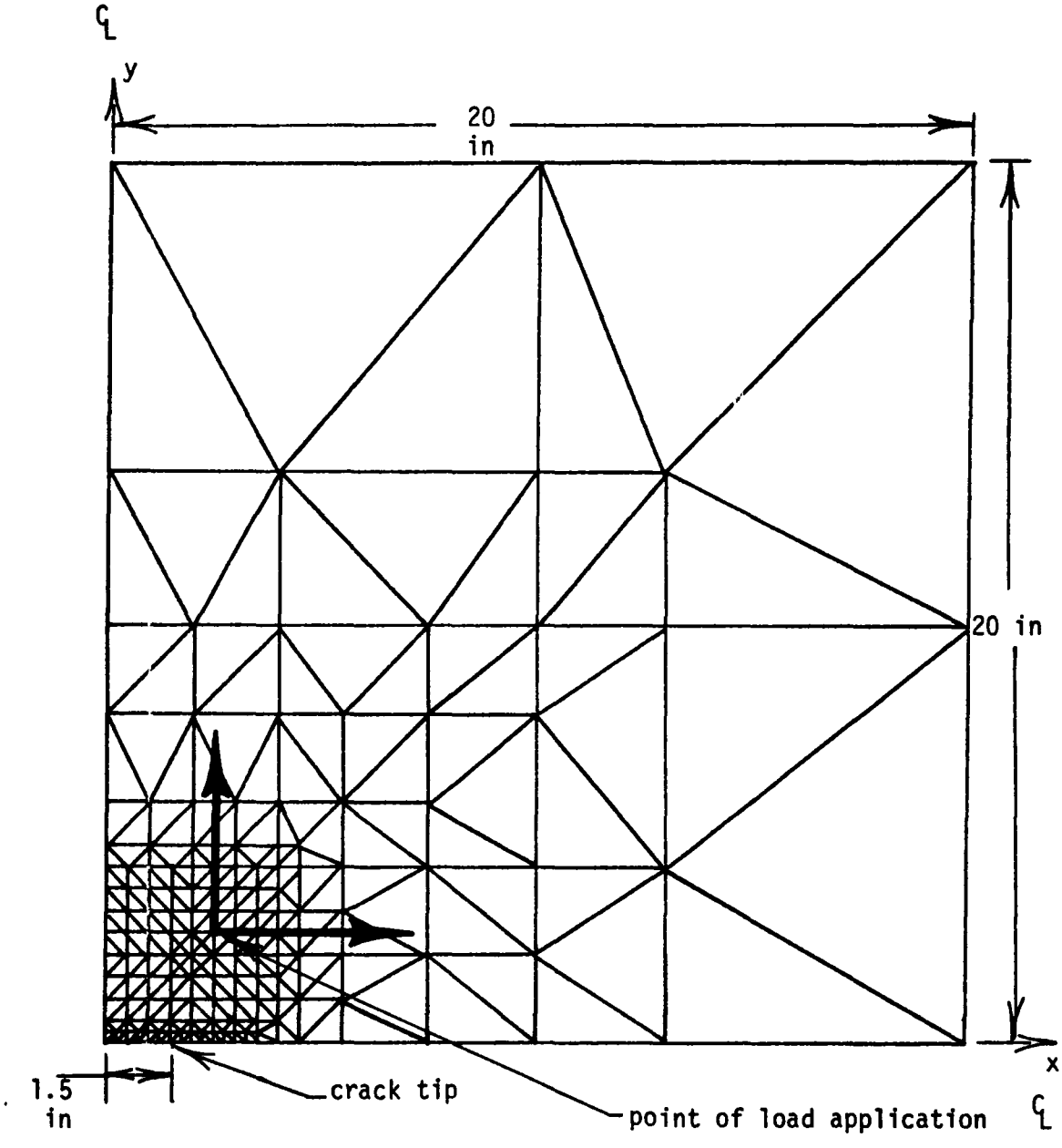

Fig. D.3. Finite element mesh used to check Green's functions

sheet was modeled; the crack was simulated by freeing the nodes in the y-direction along the x-axis from the origin to $x = 1.5$ inches. Point loads of $X = 1$ and $Y = 2$ were applied to the model at the point $z_0 = 2.5 + 2.5i$.

The finite element results were compared to the Green's functions results. For the comparison, the stresses were calculated along the line $z = x + 1.25i$ by equations (D.68) through (D.73) and with finite elements. Finite element values of stresses along this line were taken as the average of two elements midway between y-coordinates of the nodes. On figure (D.4) the dotted line, dashed line, and solid line indicate σ_x, σ_y, and σ_{xy} stresses respectively, obtained with the Green's functions while the symbols represent stresses obtained from the finite element solution. The comparison was good and verified the Green's functions within the accuracy of the finite element model.

Green's Functions for Displacements

The displacement field for the solid sheet under four point loads as shown on figure D.1a was found by substituting the stress functions $\phi(z)$, $\phi(z)$, and $\psi(t)$ shown in equation (D.8), (D.9), and (D.10) respectively into equation (D.4). The result is

$$2G(u + iv) = SF_p(z,z_0) + \overline{S}F_0(z,\overline{z}_0) \tag{D.74}$$

where

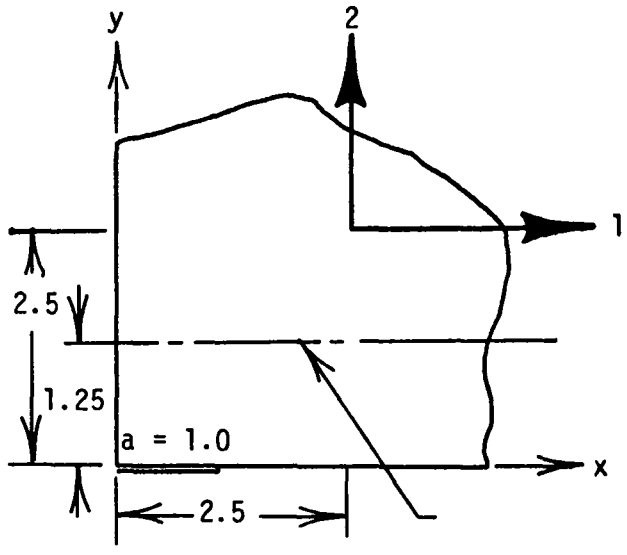

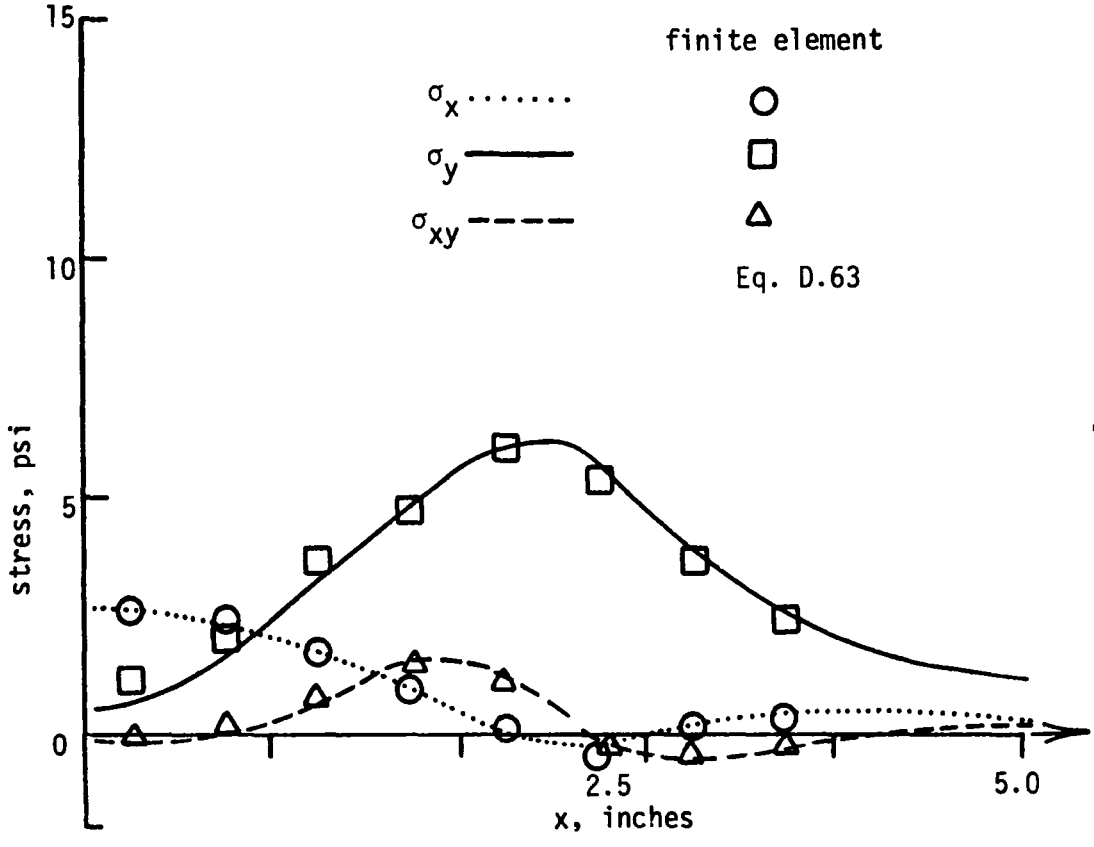

Fig. D.4. Verification of Green's functions for stresses in a cracked isotropic sheet

$$F_p(z,z_o) = 2\left\{\eta \text{Real}\left\{\text{Log}(z + z_o) - \text{Log}(z - z_o)\right\} + \frac{zz_o - \bar{z}_o\bar{z}}{\bar{z}^2 - z_o^2}\right\} \tag{D.75}$$

The displacement field for stress on the crack as shown in figure D.1b was found by substituting the equations for the stress functions $\phi(z)$, $\psi(t)$, and $\Phi(z)$ shown in equations (D.56), (D.57), and (D.43) into equation (D.4). The result is

$$2G(u + iv) = SF_o(z,z_o) + \bar{S}F_o(z,z_o) \tag{D.76}$$

where

$$F_o(z,z_o) = -\eta\, BI(z,z_o) + BI(\bar{z},z_o) - (z - \bar{z})B(\bar{z},z_o) \tag{D.77}$$

Superimposing the displacement equations for the two preceding equations yields the displacement field for the load condition shown on figure D.1c as

$$2G(u + iv) = S\left\{F_p(z,z_o) - F_o(z,z_o)\right\} + \bar{S}\left\{F_p(z,\bar{z}_o) - F_o(z,\bar{z}_o)\right\} \tag{D.78}$$

Equation (D.78) was simplified, after lengthy algebraic manipulations. The result was found as

$$2G(u + iv) = Sg(z,z_0) + \bar{S}g(z,z_0) \tag{D.79}$$

where

$$g(z,z_0) = \eta\left\{\text{Re } XA(z,z_0) - XC(z,z_0)\right\} + 0.5\left\{\eta^2 XB(z,\bar{z}_0) + \overline{XB(z,\bar{z}_0)}\right\} + XC(\bar{z},z_0) + 2\left\{\frac{zz_0 - \bar{z}_0\bar{z}}{\bar{z}^2 - z_0^2}\right\} + (z - \bar{z})B(\bar{z},z_0)$$

with

$$XA(z,z_0) = -\text{Log}\left\{-\frac{zz_0 - a^2 - I(z_0)I(z)}{zz_0 + a^2 - I(z_0)I(z)}\right\}$$

$$XB(z,z_0) = \text{Log}\left\{\frac{zz_0 - a^2 - I(z_0)I(z)}{zz_0 + a^2 - I(z_0)I(z)}\left\{\frac{z + z_0}{z_0 - z}\right\}^2\right\}$$

$$XC(z,z_0) = \frac{z_0 - \bar{z}_0}{z^2 - z_0^2}\left\{z - z_0\,\frac{I(z)}{I(\bar{z}_0)}\right\}$$

$$B(z,z_0) = \frac{1}{2}\left\{\frac{-4z_0}{z^2 - z_0^2} + \frac{2\eta\bar{z}_0}{z^2 - \bar{z}_0^2} + \frac{z - \bar{z}_0}{(z - z_0)^2} - \frac{z + \bar{z}_0}{(z + z_0)^2}\right\}$$

$$+ \frac{z_0 - \bar{z}_0}{2I(z_0)I(z)}\left\{\frac{a^2 - zz_0}{(z - z_0)^2} - \frac{a^2 + zz_0}{(z + z_0)^2}\right\}$$

$$- \frac{z}{I(z)}\left\{\frac{I(z_0)}{z_0^2 - z^2} - \eta\frac{I(\bar{z}_0)}{\bar{z}_0^2 - z^2}\right\}$$

The Green's functions for displacements were obtained from equation (D.79) by forming coefficients of the X and Y loads for the u and v displacements. The result was

$$DG_{xx} = c_o \text{ Real}(g(z,z_0) + g(z,\bar{z}_0)) \tag{D.80}$$

$$DG_{xy} = c_o \text{ Real}(i(g(z,z_0) - g(z,\bar{z}_0))) \tag{D.81}$$

$$DG_{yx} = c_o \text{ Img } (g(z,z_0) + g(z,\bar{z}_0)) \tag{D.82}$$

$$DG_{yy} = c_o \text{ Img } (i(g(z,z_0) - g(z,\bar{z}_0))) \tag{D.83}$$

with

$$c_o = \frac{1}{4Gt_m\pi(1 + \eta)}$$

where the first index of GD indicates the displacement and the second indicates the load responsible for it.

The Green's functions for displacements given in equations (D.80) through (D.83) were verified with the finite element model discussed in the previous section and shown on figure D.3. A comparison of the displacements calculated from the Green's functions and the finite element solution is shown on figure D.5. The comparison is made along the line $z = x + 2i$ where the finite element displacements are taken from the nodal points of the model. In the figure the solid and dotted lines indicate the u and v displacements calculated with the Green's functions while the symbols represent values obtained from the finite element solution. The agreement is good and verifies the Green's functions within the accuracy of the finite element model.

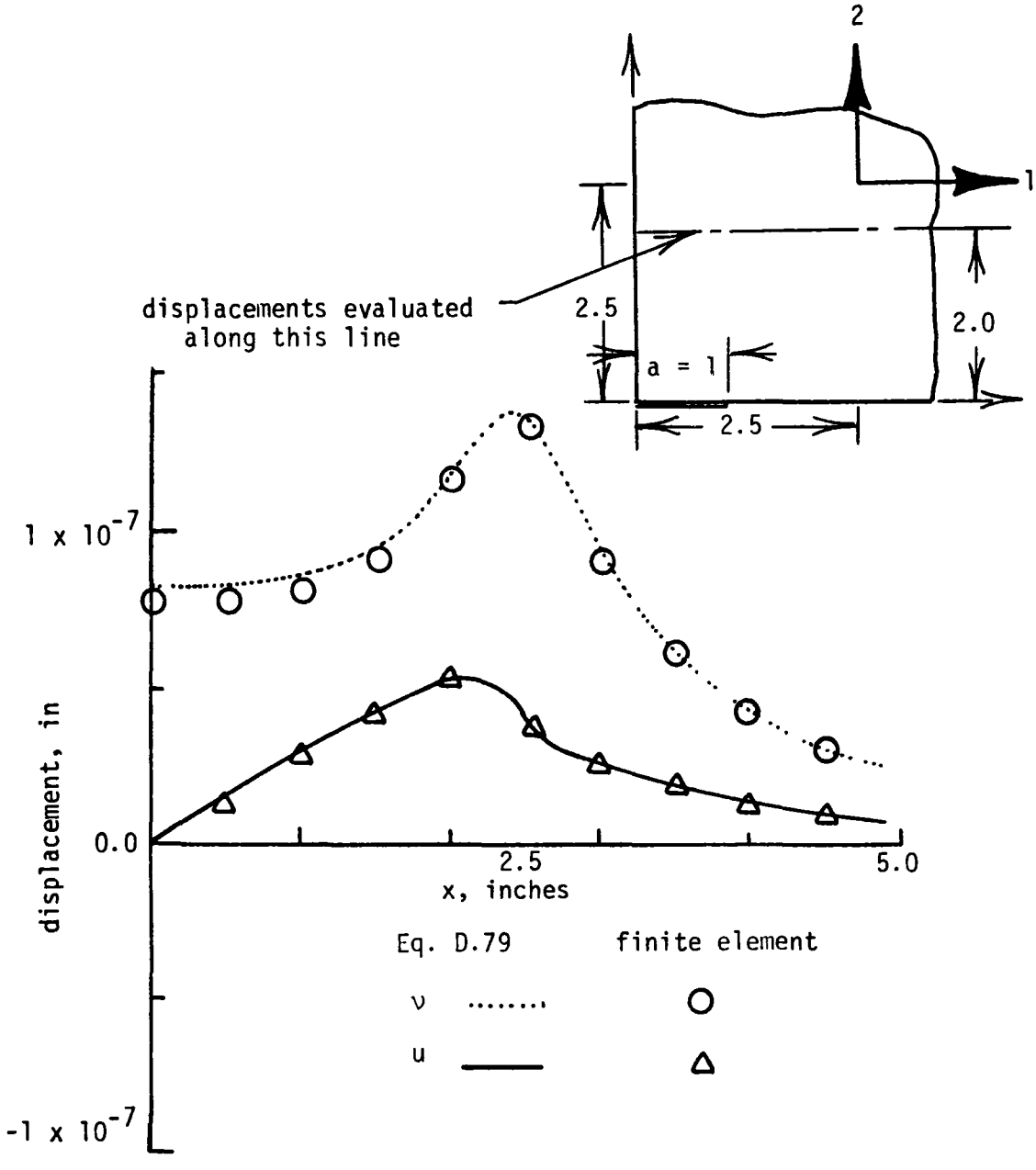

Fig. D.5. Verification of Green's functions for displacements in a cracked isotropic sheet

APPENDIX E

GREEN'S FUNCTION FOR AN UNCRACKED ORTHOTROPIC SHEET

Lekhnitskii (1968) gives the stress and displacements in an orthotropic sheet in plane stress in terms of two stress functions, $\Phi_1(z_1)$ and $\Phi_2(z_2)$, as

$$\sigma_x = 2\text{Real}\left\{s_1^2\Phi_1'(z_2) + s_2^2\Phi_2'(z_2)\right\} \tag{E.1}$$

$$\sigma_y = 2\ \text{Real}\left\{\Phi_1'(z_1) + \Phi_2'(z_2)\right\} \tag{E.2}$$

$$\sigma_{xy} = -2\text{Real}\left\{s_1\Phi_1'(z_1) + s_2\Phi_2'(z_2)\right\} \tag{E.3}$$

$$u = 2\text{Real}\left\{p_1\Phi_1(z_1) + p_2\Phi_2'(z_2)\right\} - w_o y + u_o \tag{E.4}$$

$$v = 2\text{Real}\left\{q_1\Phi_1(z_1) + q_2\Phi_2(z_2)\right\} + w_o x + v_o \tag{E.5}$$

where s_1 and s_2 are the roots of the equation.

$$s^4 + \left\{\frac{E_x}{G_{xy}} - 2\nu_{xy}\right\}s^2 + \frac{E_x}{E_y} = 0 \tag{E.6}$$

where E_x, E_y, G_{xy}, and ν_{xy} are the elastic moduli and Poisson's ratio. Leknitskii (1968) proved that the roots, s_1 and s_2, could not be purely real for real materials but are purely imaginary or complex. The complex roots occur in conjugate pairs and s_1 and s_2 are distinct roots, i.e. not complex conjugates. The following were defined

$$z_1 = x + s_1 y \qquad z_2 = x + s_2 y \qquad \nu_{yx} = \frac{\nu_{xy} E_x}{E_y}$$

$$p_1 = \frac{1}{E_x}(s_1^2 - \nu_{xy}) \qquad p_2 = \frac{1}{E_x}(s_2^2 - \nu_{xy}) \tag{E.7}$$

$$q_1 = \frac{1}{s_1 E_y}(1 - \nu_{yx} s_1^2) \qquad q_2 = \frac{1}{s_2 E_y}(1 - \nu_{yx} s_2^2) \tag{E.8}$$

Note that w_0, u_0, and v_0 in equation (E.4) and (E.5) are rigid body rotations and translations respectively and

$$\Phi_1'(z_1) = \frac{d\Phi_1(z_1)}{dz_1}, \qquad \Phi_2'(z) = \frac{d\Phi_2(z_2)}{dz_2}$$

The two required stress functions for a point load acting on a solid, orthotropic sheet were given by Lekhnitskii (1968) as

$$\Phi_1(z_1) = A_c \mathrm{Log} z_1 \qquad \Phi_2(z_2) = B_c \mathrm{Log} z_2 \tag{E.9}$$

where A_c and B_c satisfy the equations (for material axis concurrent with the axis of orthotropicity)

$$
\begin{aligned}
A_c + B_c - \bar{A}_c - \bar{B}_c &= \frac{Y}{2\pi t_c i} \\
s_1 A_c + s_2 B_c - \bar{s}_1 \bar{A}_c - \bar{s}_2 \bar{B}_c &= \frac{-X}{2\pi t_c i} \\
s_1^2 A_c + s_2^2 B_c - \bar{s}_1^2 \bar{A}_c - \bar{s}_2^2 \bar{B}_c &= \frac{-\nu_{xy} Y}{2\pi t_c i} \\
\frac{A_c}{s_1} + \frac{B_c}{s_2} - \frac{\bar{A}_c}{\bar{s}_1} - \frac{\bar{B}_c}{\bar{s}_2} &= \frac{\nu_{yx} X}{2\pi t_c i}
\end{aligned}
\qquad \text{(E.10)}
$$

With the use of the preceding equations, stress functions for point loads acting on a unidirectional boron/epoxy composite were developed. For this material the material constants are

$$E_x = 0.27 \times 10^7 \text{ psi} \qquad E_y = 3.0 \times 10^7 \text{ psi}$$

$$G_{xy} = 0.7 \times 10^6 \text{ psi} \qquad \nu_{xy} = 0.019$$

With these material constants, the roots of equation (E.6) were found to be purely imaginary as

$$s_{1,3} = \pm 0.153i \qquad s_{2,4} = \pm 1.95i$$

For purely imaginary roots equations, A_c and B_c were found from equations (E.10) as

$$A_c = C11\ X + i\ C12\ Y \tag{E.11}$$

$$B_c = C21\ X + i\ C22\ Y \tag{E.12}$$

where

$$C11 = \frac{s_2(s_1^2 \nu_{xy} + 1)}{4\pi t_c(s_2^2 - s_1^2)} \qquad C12 = \frac{s_1^2 + \nu_{xy}}{4\pi t_c(s_2^2 - s_1^2)}$$

$$C21 = -\frac{s_1(s_2^2\ \nu_{yx} + 1)}{4\pi t_c(s_2^2 - s_1^2)} \qquad C22 = -\frac{s_2^2 + \nu_{xy}}{4\pi t_c(s_2^2 - s_1^2)}$$

Using equations (E.11) and (E.12) and translating the origin so that the singularity occurs at the point z_o, equations (E.9) became

$$\Phi_1(z_1,w_1) = (C11\ X + i\ C12\ Y)\mathrm{Log}(z_1 - w_1)$$

$$\Phi_2(z_2,w_2) = (C21\ X + i\ C22\ Y)\mathrm{Log}(z_2 - w_2) \tag{E.13}$$

where $w_1 = x_0 + s_1 y_0$ $\qquad$ $w_2 = x_0 + s_2 y_0$

Equations (E.13) were used to construct a solution for four point loads acting on a solid orthotropic sheet as shown in figure E.1. The result was

$$\Phi_1(z_1,w_1) = C11\ G8(z_1,w_1)X + i\ C12\ G9(z_1,w_1)Y$$

$$\Phi_2(z_2,w_2) = C21\ G8(z_2,w_2)X + i\ C22\ G9(z_2,w_2)Y \tag{E.14}$$

where

$$G8(z,w) = \text{Log}(z - w) - \text{Log}(z + \bar{w}) - \text{Log}(z + w) + \text{Log}(z - \bar{w}) \tag{E.15}$$

$$G9(z,w) = \text{Log}(z - w) + \text{Log}(z + \bar{w}) - \text{Log}(z + w) - \text{Log}(z - \bar{w}) \tag{E.16}$$

The derivatives of equations (E.14) were found to be

$$\Phi_1'(z_1,w_1) = C11\ G8'(z_1,w_1)X + i\ C12\ G9'(z_2,w_2)Y$$

$$\Phi_2'(z_2,w_2) = C21\ G8'(z_1,w_1)X + i\ C22\ G9'(z_2,w_2)Y \tag{E.17}$$

where

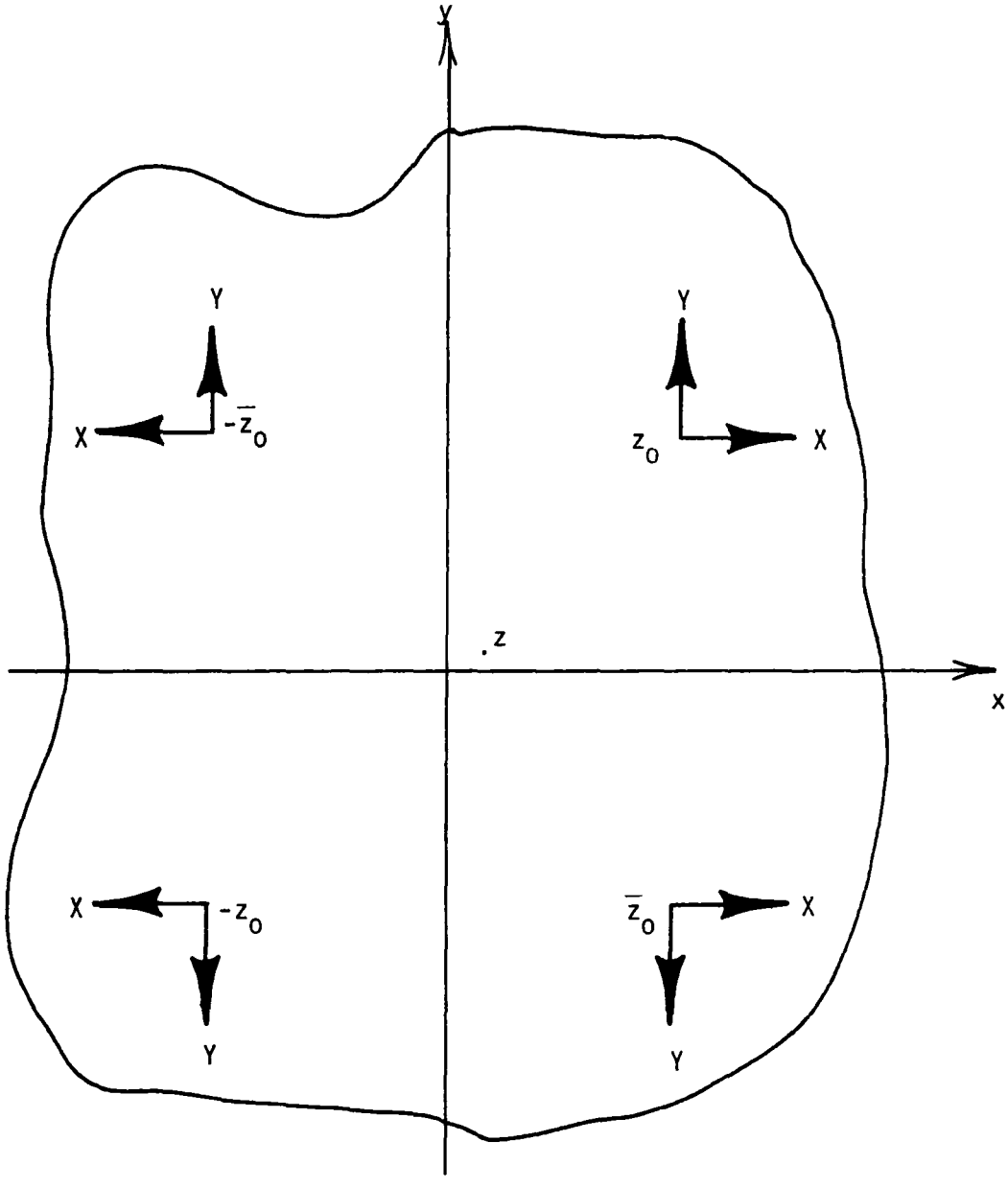

Fig. E.1. Location of point loads on orthotropic sheet

$$G8'(z,w) = \frac{2\bar{w}}{z^2 - \bar{w}^2} + \frac{2w}{z^2 - w^2} \tag{E.18}$$

$$G9'(z,w) = \frac{2w}{z^2 - w^2} - \frac{2\bar{w}}{z^2 - \bar{w}^2} \tag{E.19}$$

Equations (E.13) and (E.17) can be used in equations (E.1) through (E.5) to describe the stresses and displacements in the orthotropic sheet.

Green's Functions for Stresses

The Green's functions for stresses were developed by substituting equations (E.17) into equations (E.1), (E.2), and (E.3) to determine the stress state as

$$\sigma_x = HS_{xx}X + HS_{xy}Y \tag{E.20}$$

$$\sigma_y = HS_{yx}X + HS_{yy}Y \tag{E.21}$$

$$\sigma_{xy} = HS_{(xy)x}X + HS_{(xy)y}Y \tag{E.22}$$

where the Green's functions are given by

$$HS_{xx} = 2\text{Real}\left\{s_1^2\ C11\ G8'\ (z_1, w_1) + s_2^2\ C21\ G8'\ (z_2, w_2)\right\} \quad (E.23)$$

$$HS_{xy} = 2\text{Real}\left\{ i\left\{s_1^2\ C12\ G9'\ (z_1, w_1) + s_2^2\ C22 G9'\ (z_2, w_2)\right\}\right\} \quad (E.24)$$

$$HS_{yx} = 2\text{Real}\left\{ C11\ G8'\ (z_1, w_1) + C21\ G8'\ (z_2, w_2)\right\} \quad (E.25)$$

$$HS_{yy} = 2\text{Real}\left\{ i\left\{C12\ G9'\ (z_1, w_1) + C22\ G9'\ (z_2, w_2)\right\}\right\} \quad (E.26)$$

$$HS_{(xy)x} = -2\text{Real}\left\{s_1 C11\ G8'\ (z_1, w_1) + s_2\ C21\ G8'\ (z_2, w_2)\right\} \quad (E.27)$$

$$HS_{(xy)y} = -2\text{Real}\left\{ i\left\{s_1\ C12\ G9'\ (z_1, w_1) + s_2\ C22\ G9'\ (z_2, w_2)\right\}\right\} \quad (E.28)$$

To verify these Green's functions, stresses computed with equations (D.20) through (D.22) were compared to finite element results. The model used for the finite element solution is identical to that shown in Appendix D on figure D.3 except that no nodes were freed along the x-axis to simulate a crack. The finite element program used is documented by Zienkiewicz (1971) as mentioned in the previous appendix. However, the program as given by Zienkiewicz does not have orthotropic capability. Therefore, it was modified by introducing the orthotropic stiffness matrix for plane stress given by Zienkiewicz (1971) as

$$[D] = \frac{E_y}{1 - n\nu_{yx}} \begin{bmatrix} n & n\nu_{yx} & 0 \\ n\nu_{yx} & 1 & 0 \\ 0 & 0 & M(1 - n\nu_{yx}^2) \end{bmatrix}$$

where $n = \frac{E_x}{E_y}$ and $m = \frac{G_{yx}}{E_y}$ in place of the isotropic stiffness matrix in the program.

The comparisons between the stresses along the line $z = x + 1.25i$ are shown on figure E.2 on which the dotted line, dashed line, and solid line indicate the σ_x, σ_y, and σ_{xy} stresses respectively from the Green's functions. The symbols on the figure indicate the same stresses obtained from the finite element solution. The comparison was good and verified, within the accuracy of the finite element model, the accuracy of the Green's functions for stresses.

Green's Functions for Displacements

The Green's functions for displacements were developed by substituting equations (E.14) into equations (E.4) and (E.5). Because of the symmetry of the loads the rigid body rotation, w_0, and the rigid body translations, u_0 and v_0, are zero in equations (E.4) and (E.5). The results are

$$u = HD_{xx}X + HD_{xy}Y \tag{E.29}$$

$$v = HD_{yx}X + HD_{yy}Y \tag{E.30}$$

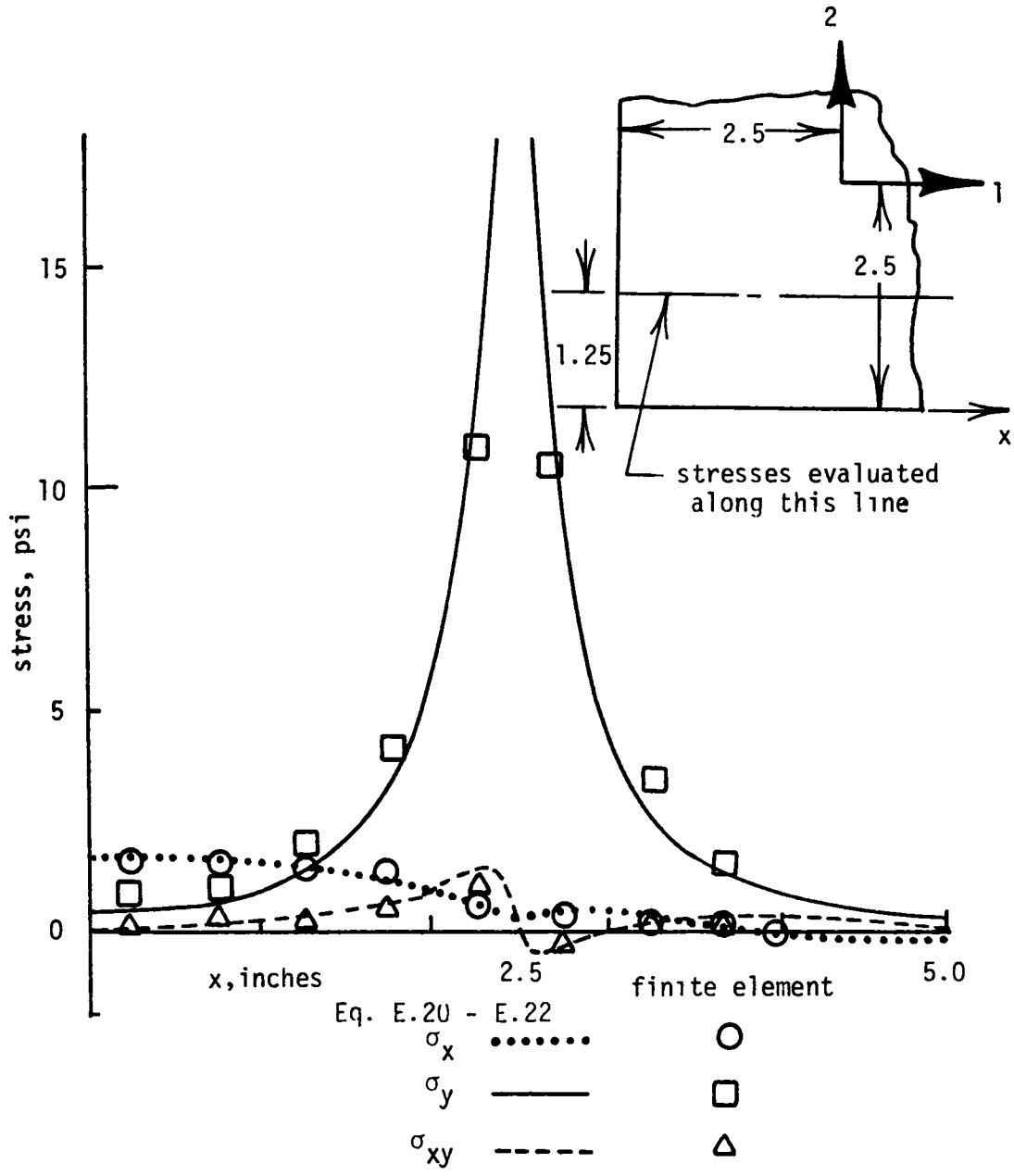

Fig. E.2. Verification of Green's functions for stresses in an uncracked orthotropic sheet

where the Green's functions are given by

$$HD_{xx} = 2\text{Real}\left\{p_1\ C11\ G8(z_1,w_1) + p_2\ C21\ G8(z_2,w_2)\right\} \qquad (E.31)$$

$$HD_{xy} = 2\text{Real}\left\{i\left\{p_1\ C12\ G9(z_1,w_1) + p_2\ C22\ G9(z_2,w_2)\right\}\right\} \qquad (E.32)$$

$$HD_{yx} = 2\text{Real}\left\{q_1\ C11\ G8(z_1,w_1) + q_2\ C21\ G8(z_2,w_2)\right\} \qquad (E.33)$$

$$HD_{yy} = 2\text{Real}\left\{i\left\{q_1\ C21\ G9(z_1,w_1) + q_2\ C22\ G9(z_2,w_2)\right\}\right\} \qquad (E.34)$$

With the use of the finite element model shown in figure D.3, equations (E.31) through (E.34) were verified by comparing the displacements along the line $z = x + 2i$ calculated with equation (E.29) and (E.30) shown on dotted and dashed line, respectively, on figure E.3 with the displacements calculated with the finite element program. The comparison is good and within the accuracy of the finite element model verifies the Green's functions for displacements in the uncracked orthotropic sheet.

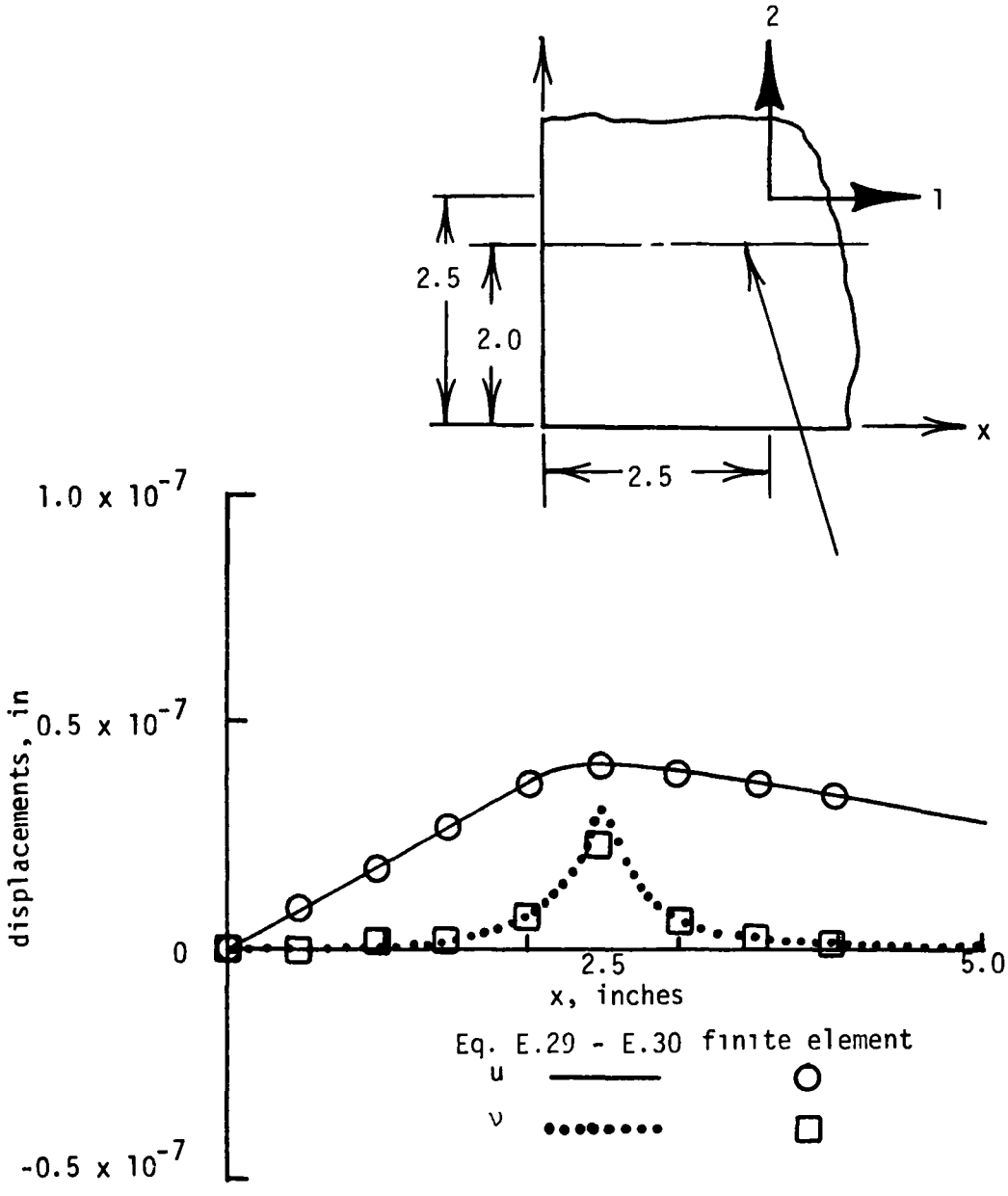

Fig. E.3. Verification of Green's functions for displacements in an uncracked orthotropic sheet

APPENDIX F

COMPUTER PROGRAM TO PREDICT CRACK AND DEBOND GROWTH

The analysis developed in Chapters IV and V to predict crack growth in reinforced systems requires the use of a digital computer to perform numerical integration and solve large systems of simultaneous equations. The analysis was programmed in FORTRAN IV for use on the NASA Langley Research Center (LRC) CDC 6600 computing system. However, no special system routines were used in the program, and the program should be usable on any computing system that uses a FORTRAN IV compiler. With the exception of the Gaussian elimination subroutine SIMQ, the program is all original code.

For economical reasons the user should be aware of the central processing time (CP) and central memory (core) required to execute the program. The CP time is primarily a function of the numerical integration of the Green's functions. Several integrations are required for each shear element, i.e. elements of region B shown on figure 8. Consequently, the CP time requirement is a function of the number of shear elements and can vary from a few to several thousand seconds depending upon the number of elements. The core requirements are also a function of the number of shear elements. Each element

contains two unknown shear stresses, f_{xz} and f_{yz}. The number of rows and columns of the square, fully populated coefficient matrix used to solve for these stresses is two times the number of elements. In the program the dimensions are set for fifty shear elements (100 unknowns), but the program can accomodate more elements if the array Z9(10,000) in the program is enlarged. For fifty elements the core requirement is 137K octal.

Data are read in the program via a NAMELIST with the following definitions:

E3 modulus of the cracked sheet

T2 thickness of the cracked sheet

V1 Poisson's ratio of the cracked sheet

E4 modulus of the composite sheet in the y-direction (loading-axis)

E5 modulus of the composite sheet in the x-direction

V4 Poisson's ratio of the composite sheet for a load applied in the x-direction

GC shear modulus of the cracked sheet

T4 thickness of the reinforcement sheet

TAD thickness of the adhesive layer

GAD initial effective shear modulus of the adhesive

GAD2 secondary effective shear modulus of the adhesive

SYIELD yield stress of the bulk adhesive in uniaxial tension

A1 initial crack length in metal sheet

F initial aspect ratio of the debond ellipse

NC number of columns of interlaminar sheat elements

NR number of rows of interlaminar shear elements

FCYC final number of applied load cycles

S remote applied stress applied to the reinforced system in the y-direction

As an example a sample run was made for one iteration. Figure F.1a shows the model prior to the iteration and figure F.1b shows it after the iteration. The sample NAMELIST input for the run was as follows:

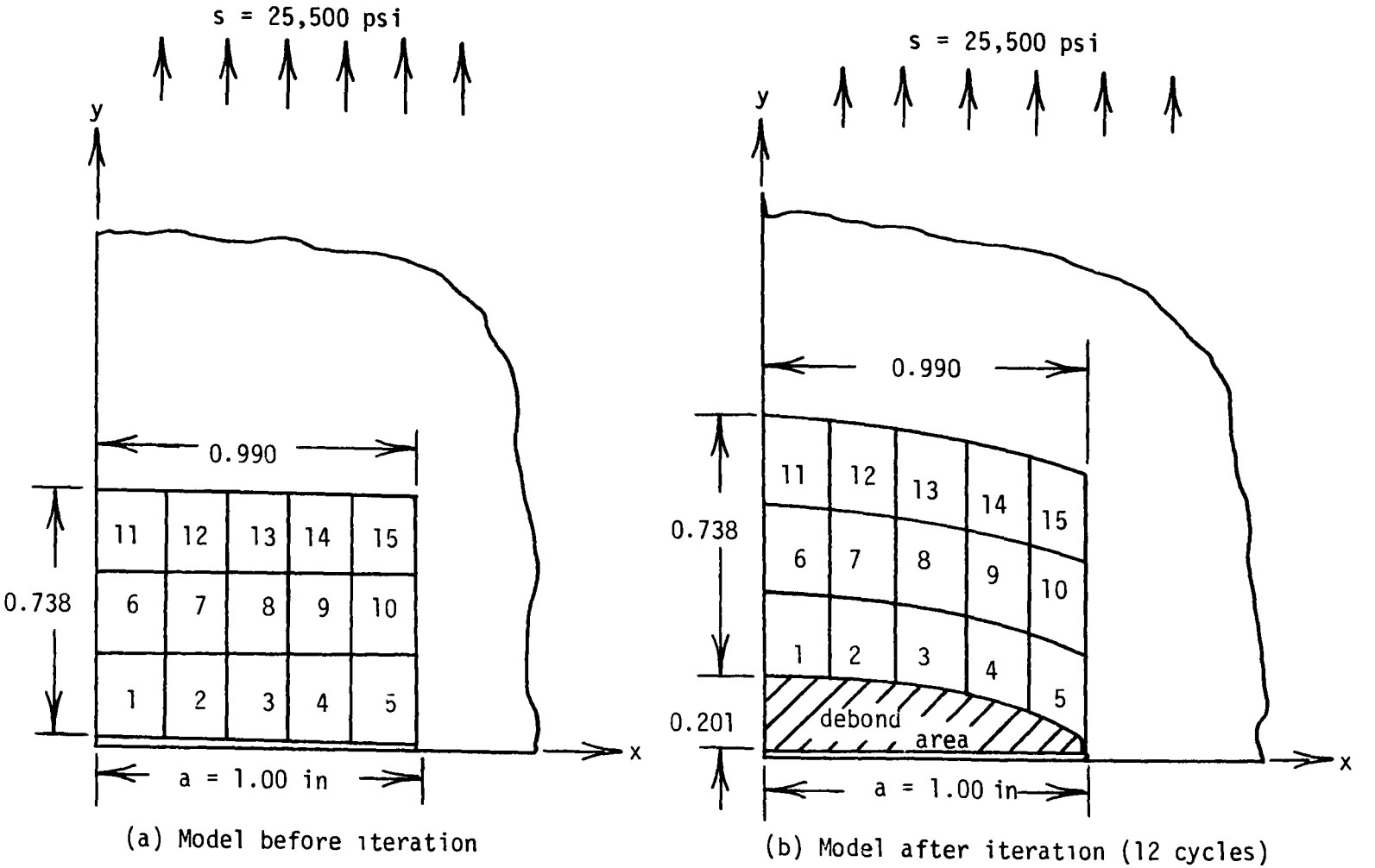

(a) Model before iteration

(b) Model after iteration (12 cycles)

Fig. F.1. Model for sample run

SAMPLE INPUT

```
$INPU E3=1.0E+07,T2=.156,VI=.30,E4=3.0E+07,E5=3.0E+06,V4=.02,GC=7.0E+05,
TAD=.004,GAD=65000.,GAD2=36000.,SYIELD=4200.,A1=1.00,F=.001,NC=5,NR=3,
FCYC=10000.,S=25500.,T4=.0208,
$
```

SAMPLE OUTPUT

MODULUS OF THE CRACKED SHEET	.107E+08
THICKNESS OF THE CRACKED SHEET	.156E+00
POISSONS RATIO FOR THE CRACKED SHEET	.300E+00
COMP MODULUS PARALLEL TO LOAD	.300E+08
COMP MODULUS TRANSV TO LOAD	.300E+07
SHEAR MODULUS OF COMPOSITE	.700E+06
COMP POISSONS RATIO TRANSV TO LOAD AXIS	.200E-01
THICKNESS OF THE REINFORCEMENT SHEET	.280E-01
MINOR AXIS HEIGHT IN PER CENT CRACK LENGTH	.100E-02
REMOTE APPLIED STRESS	.255E+05
NUMBER OF COLUMNS FOR BOUNDARY POINTS	5
NUMBER OF ROWS FOR BOUNDARY POINTS	3
FINAL NUMBER OF APPLIED LOAD CYCLES	.100E+05
INITIAL CRACK LENGTH	.100E+01
ADHESIVE THICKNESS	.400E-02
SHEAR MODULUS OF THE ADHESIVE	.650E+05
SECONDARY SHEAR MODULUS AFTER YIELDING	.360E+05
YIELD STRESS OF MODULUS IN UNIAXIAL TENSION	.420E+04

METAL SIGM-X= .269E+03 SIGM-Y= .200E+05

COMPOSITE SIGM-X= -.150E+04 SIGM-Y= .559E+05

X AND Y DIMENSIONS OF INTEGRATION AREA ARE .990E+00 .746E+00

NODE NUMBER	X-COR	Y-COR
1	.990E-01	.125E+00
2	.297E+00	.121E+00
3	.495E+00	.113E+00
4	.693E+00	.988E-01
5	.891E+00	.765E-01
6	.990E-01	.373E+00
7	.297E+00	.365E+00
8	.495E+00	.349E+00
9	.693E+00	.323E+00
10	.891E+00	.285E+00
11	.990E-01	.622E+00
12	.297E+00	.613E+00
13	.495E+00	.593E+00
14	.693E+00	.563E+00
15	.891E+00	.521E+00

14 ELEMENTS HAVE YIELDED AT .189E+05

YIELDED ELEMENTS

3	2	1	4	5	9
8	7	10	6		

THE YIELD MACROSCOPIC STRESS IS .716E+04

NODE	DEBOND HEIGHT	ELASTIC X-COEFFICIENT	ELASTIC Y-COEFFICIENT
1	.125	.300E+01	.849E+04
2	.121	.279E+02	.859E+04
3	.113	.100E+03	.864E+04
4	.099	.327E+03	.847E+04
5	.076	.111E+04	.667E+04
6	.373	.346E+02	.256E+04
7	.365	.130E+03	.266E+04
8	.349	.328E+03	.276E+04
9	.323	.806E+03	.276E+04
10	.285	.191E+04	.220E+04
11	.622	.916E+02	.117E+04
12	.613	.293E+03	.119E+04
13	.593	.560E+03	.117E+04
14	.563	.983E+03	.108E+04
15	.521	.180E+04	.807E+03

WITH PLASTICITY

NODE	DEBOND HEIGHT	X-COEFFICIENT	Y-COEFFICIENT
1	.125	.207E+01	.708E+04
2	.212	.213E+02	.709E+04
3	.113	.795E+02	.704E+04
4	.099	.245E+03	.679E+04
5	.076	.805E+03	.536E+04
6	.373	.438E+02	.312E+04
7	.365	.156E+03	.321E+04
8	.349	.371E+03	.325E+04
9	.323	.864E+03	.315E+04
10	.285	.191E+04	.244E+04
11	.622	.105E+03	.165E+04
12	.613	.333E+03	.165E+04
13	.593	.635E+03	.161E+04
14	.563	.110E+04	.146E+04
15	.521	.189E+04	.112E+04

K-BOND	K-UNSTIFFEND	K-STIFFENED	K-FACTOR
-.108E+05	.200E+05	.919E+04	.459E+00

STRESS AND STRAIN IN THE METAL

NODE	SIG-1	SIG-2	SIG-12
1	-.681E+04	.580E+04	-.472E+02
6	-.340E+04	.121E+05	-.103E+03
11	-.137E+04	.154E+05	-.146E+03

NODE	EPS-1	EPS-2	EPS-12
1	-.799E-03	.733E-03	-.115E-04
6	-.657E-03	.123E-02	-.250E-04
11	.559E-03	.148E-02	-.354E-04

STRESS AND STRAIN IN THE COMPOSITE

NODE	SIG-1	SIG-2	SIG-12
1	.838E+04	.105E+06	.742E+03
6	.897E+04	.728E 05	.252E+03
11	.758E+04	.568E+05	-.301E+03

NODE	EPS-1	EPS-2	EPS-12
1	.272E-02	.350E-02	.674E-04
6	.294E-02	.242E-02	.360E-04
11	.249E-02	.189E-02	-.430E-04

ENERGY RELEASE ON MINOR AXIS IS .597E+01

APPLIED CYCLES= .990E+01
DA/DN BEFORE CYCLE INCREMENT IS .181E-04
DB/DN BEFORE CYCLE INCREMENT IS .202E-01

INCREMENT CYCL = .990E+01 CRACK,LENGTH= .100E+01

MAX DEBOND HEIGHT= .201E+00

```
      PROGRAM COLLS(INPUT,OUTPUT,TAPE4)
C
C   THIS PROGRAM CALCULATES CRACK AND DEBOND GROWTH IN A
C   REINFORCED SYSTEM COMPOSED OF A CRACKED METAL
C   SHEET REINFORCED WITH A UNIDIRECTIONAL BORON/EPOXY
C   SHEET.
C
      COMMON/ROT/Z9(10000),D(100),NALF
      COMMON/BOND2/NE,NL,NT,XC(100),YC(100),XA(100),YA(100),
     1NOP(100)
      DIMENSION FTNC(50),FXNCY(50),FA1(50),FB1(50 )
      COMMON/ADHES/TAD,GAD
      COMMON/TOP/E3,T2,V1,SMX,SMY,G,CONS,Q,A1,SCON
      DIMENSION DR(100),CPR(100),DPR(100)
      COMMON/XLIMIT/DC(2,51),DB(6,51),FF
      DIMENSION CM(3,3),SIG(3),STRAIN(3),DD(100)
      DIMENSION SM(3,3),CMM(3,3),CMC(3,3),STRESSM(3),STRESSC
     1(3)
      DIMENSION TSIGM(3),TSIGMT(3),SMM(3,3),SMC(3,3)
      DIMENSION TOTG(50),SIGMT(3),TSTRAIN(3),STRESS(2,3,50)
     1,STRANN(2,3,50)
      COMMON/BOT/E4,T4,V4,SCX,SCY,GB,CONB,Q1,GC,E5
      COMMON/CTOL/TOL,NC,NR,TX,TY,NBC(100),IBC
      COMMON/BOND/F,P1,P2,XKF,XKUNS,XKSTIF
      COMMON/DECAY/EE,ALPHA1,ALPHA2
      COMPLEX Z,CI,XK
      EXTERNAL XK
      CI=CMPLX(0.,1.0)
      NAMELIST/INPU/E3,T2,F,S,TEST,T4,E4,V4,V1,E5,GC,TAD,GAD
     1,NR,NC,FCYC,
     1A1,GAD2,SYIELD
C
C     E3-MODULUS OF THE CRACKED SHEET
C     T2-THICKNESS OF THE CRACKED SHEET
C     V1-IS THE POISSONS RATIO FOR THE CRACKED SHEET
C     GC-SHEAR MODULUS OF THE REINFORCEMENT SHEET
C     E4-MODULUS OF THE REINFORCEMENT SHEET IN THE LOADING
C     DIRECTION
C     E5-MODULUS OF THE REINFORCEMENT SHEET TRANSVERSE TO
C     THE LOADING AXIS
C     V4 IS THE POISSONS RATIO FOR THE BOTTOM SHEET FOR A
C     TRANSVERSE LOAD
C     T4-THICKNESS OF THE REINFORCEMENT SHEET
C     F-MINOR AXIS HEIGHT IN PERCENT CRACK LENGTH
C     S -REMOTE APPLIED STRESS
C     NR-NUMBER OF ROWS OF BOUNDARY POINTS
C     NC-NUMBER OF COLUMNS OF BOUNDARY POINTS
C     FCYC-FINAL NUMBER OF LOAD CYCLES
C     A1-INITIAL CRACK LENGTH
C
      K=0
```

```
 1000 CONTINUE
      READ INPU
      MX=NR*NC
      M=MX
      N=MX
      NALF=MX
C
C     OUTPUT THE INPUT
C
      PRINT 1,E3
      PRINT 2,T2
      PRINT 20,V1
      PRINT 18,E4
      PRINT 26,E5
      PRINT 27,GC
      PRINT 21,V4
      PRINT 19,T4
      PRINT 3,F
      PRINT 7,S
      PRINT 30,NC
      PRINT 31,NR
      PRINT 32,FCYC
      PRINT 34,A1
      PRINT 24,TAD
      PRINT 25,GAD
      PRINT 5,GAD2
      PRINT 6,SYIELD
      P1=2.
      P2=2.
      TOL=.001
      FF=F
      N=2*N
      M=2*M
      NSQ=N*N
      IF(N.GT.100)500,501
  500 PRINT 502,M,N
  502 FORMAT(//* ERRORS -- M OR N EXCEEDS DIMENSIONS BOUNDS
     1M=*I10*N=*I10//)
      GO TO 1001
  501 CONTINUE
      Q=(3.-V1)/(1.+V1)
      Q1=(3.-V4)/(1.+V4)
      G=E3/(2.*(1.+V1))
      CONS=1./(12.566*T2    *(1+Q)*G)
      SCON=1./(6.2832*(1+Q  )*T2)
      GB=E4/(2.*(1.+V4))
      CONB=1./(12.566*T4   *(1+Q1)*GB)
      V5=V4*E5/E4
      EE=2.7182818
      ALPHA1=GAD*(1./(T2*E3)+1./(T4*E4))/TAD
      ALPHA1=SQRT(ALPHA1)
```

```
      ALPHA2=GAD2*(1./(T2*E3)+1./(T4*E4))/TAD
      ALPHA2=SQRT(ALPHA2)
      TY=-ALOG(.05)/ALPHA2
C
C CALCULATE THE  REMOTE STRESSES
C
C ZERO ALL COMPLIANCE MATRICES
C
      DO 50 I=1,3
      DO 50 J=1,3
      CM(I,J)=0.
      CMM(I,J)=0.
      CMC(I,J)=0.
   50 CONTINUE
C
C CALCULATE COMPLIANCE FOR METAL SHEET
C
      CMM(1,1)=E3/(1.-V1**2)
      CMM(1,2)=V1*CMM(1,1)
      CMM(2,1)=CMM(1,2)
      CMM(2,2)=CMM(1,1)
      CMM(3,3)=G
C
C  GENERATE THE STIFF MATRIX FOR THE METAL SHEET
C
      CALL INVER(CMM,SMM,DD)
C
C  CALCULATE COMPLIANCE FOR COMPOSITE SHEET
C
      XN=E5/E4
      XM=GC/E5
      CC=E4/(1.-XN*V4**2)
      CMC(1,1)=XN*CC
      CMC(1,2)=XN*V4*CC
      CMC(2,1)=CMC(1,2)

      CMC(2,2)=CC
      CMC(3,3)=XM*(1.-XN*V4**2)*CC
C
C  GENERATE THE STIFF MATRIX FOR THE COMPOSITE SHEET
C
      CALL INVER(CMC,SMC,DD)
C
C GENERATE MACRO STIFFNESS MATRIX
C
      DO 51 I=1,3
      DO 51 J=1,3
      CM(I,J)=CMM(I,J)*T2+CMC(I,J)*T4
   51 CONTINUE
C
      CALL INVER(CM,SM,DD)
```

```
      SIG(1)=0.0
      SIG(2)=S*(T2+T4)
      SIG(3)=0.0
      CALL MULT(SM,SIG,STRAIN)
  400 FORMAT(3E11.3)
C
C CAICULATE STRESSES IN EACH LAYER
C
      CALL MULT(CMM,STRAIN,STRESSM)
      SMX=STRESSM(1)
      SMY=STRESSM(2)
      CALL MUIT(CMC,STRAIN,STRESSC)
      SCX=STRESSC(1)
      SCY=STRESSC(2)
      PRINT 300,SMX,SMY
  300 FORMAT(/* METAL       SIGM-X=*E10.3* SIGM-Y=*E10.3)
      PRINT 301,SCX,SCY
  301 FORMAT(/* COMPOSITE  SIGM-X=*E10.3* SIGM-Y=*E10.3/)
C
C SET UP LOOPS FOR RIGHT HAND VECTOR AND COEFFICIENT MATRIX
C
      T1=T2
       CALL CPAR
C
C  LOOP ON INCREMENTS OF LOAD CYCLES
C
      TNC=0.0
      KOUNT=0
 1004 CONTINUE
      IF(KOUNT.NE.0)PRINT 551,KOUNT
  551 FORMAT(//10X* XXXXXXXXXX  INCREMENT FOR LOAD CYCLES*
     1*IS*I5   XXXXXXXXX*/)
      TX=.99*A1
      PRINT 16,TX,TY
   16 FORMAT(/* X AND Y DIMENSIONS OF INTEGRATION AREA ARE *
     12E11.3/)
      KOUNT=KOUNT+1
      MSAVE=M
      CALL GRID
      CALL FORM(N,M)
C
C  MAKE RIGHT HAND SIDE A UNIT VECTOR FOR USE WITH PLASTIC
C  ANAIYSIS
C
      DO 1401 I=1,N
C  SAVE UNIT RIGHT HAND VECTOR
      DR(I)=D(I)/S
      D(I)=D(I)/S
 1401 CONTINUE
      REWIND 4
 1130 FORMAT(11E10.3)
```

```
C
C   STORE COEFFICIENT MATRIX ON TAPE
C
      WRITE(4,1130)(Z9(I),I=1,NSQ)
      REWIND 4
      CALL SIMQ(Z9,D,N,IND)
C
C   RETRIVE COEFFICIENT MATRIX
C
      READ(4,1130)(Z9(I),I=1,NSQ)
C
C   SAVE ELASTIC SOLUTION
C
      DO 1402 I=1,N
      DD(I)=D(I)*S
 1402 CONTINUE
C
C   CALL THE PLASTIC SUBROUTINE TO FIND INTERLAMINAR STRESSES
C   AFTER YIELDING
C
      CALL PLASTIC(SYIELD,GAD2,S,DR)
      NALF=N/2
      PRINT 17
   17 FORMAT(/70X*WITH PLASTICITY*29X*ELASTIC*)
      PRINT 11
      DO 104 I=1,NALF
      IK=I+NALF
      X=DC(1,I)
      Y=DC(2,I)
      PRINT 12,X,I,Y,D(I),D(IK),DD(I),DD(I+NALF)
  104 CONTINUE
C
      XKTOT=0.
      DO 105 J=1,NALF
      X=DC(1,J)
      Y=DC(2,J)
      Z=X+CI*Y
      CALL XINTG(Z,J,A1,S11,S12,S21,S22,XK,3)
      XK1=S11+S12
      XK2=-(S21+S22)
      XKTOT=XKTOT+XK1
  105 CONTINUE
C
C PRINT THE STRESS INTENSITIES
C
      XKUNS=SIY*A1**.5
      XKSTIF=XKUNS+XKTOT
      XKF=XKSTIF/XKUNS
      PRINT 14
      PRINT 15,XKTOT,XKUNS,XKSTIF,XKF
  100 CONTINUE
```

```
      M=MSAVE
C
C  CALCULATE STRAINS AND STRESSES AT COORDINATE POINTS IN
C  THE ADHERENDS
C
      DO 1220 I=1,MX,MC
      X=DC(1,I)
      Y=DC(2,I)
      Z=X+CI*Y
      DO 1226 KTYPE=1,2
      CALL VERI(Z,SXX,SXY,SXXY,SYX,SYY,SYXY,MX,KTYPE)
C
C  FIRST THREE TERMS ARE FROM X-LOADS THE LATTER THREE FROM
C  Y-LOADS
C
      TSIGM(1)=SXX+SYX
      TSIGM(2)=SXY+SYY
      TSIGM(3)=SXXY+SYXY
C
C  CALCULATE THE STRESSES IN THE COMPOSITE SHEET
C
      CALL RESIGM(Z,S11,S22,S12,KTYPE,STRESSM,STRESSC)
C
C  SUPERIMPOSE STRESSES
C
      TSIGMT(1)=TSIGM(1)+S11
      TSIGMT(2)=TSIGM(2)+S22
      TSIGMT(3)=TSIGM(3)+S12
C
C  CALCULATE THE CORRESPONDING STRAINS
C
      IF(KTYPE.EQ.1)1221,1222
 1221 CALL MULT(SMI,TSIGMT,TSTRAIN)
      GO TO 1224
 1222 CALL MULT(SMC,TSIGMT,TSTRAIN)
 1224 CONTINUE
C
C      STORE ALL VALUES
C
      DO 1225 IK=1,3
      STRESS(KTYPE,IK,I)=TSIGMT(IK)
      STRAIN(KTYPE,IK,I)=TSTRAIN(IK)
 1225 CONTINUE
 1226 CONTINUE
 1220 CONTINUE
      PRINT 1227
 1227 FORMAT(/* STRESS AND STRAIN IN THE METAL */)
      PRINT 1228
 1228 FORMAT(2X*NODE*5X*SIG-1*8X*SIG-2*8X*SIG-12*8X*EPS-1*8X
     1*EPS-2*8X*EPS-12*)
      PRINT 1229,(I,(STRESS(1,K,I),K=1,3),(STRAIN(1,K,I),
```

```
     1K=1,3),I=1,MX,NC)
1229 FORMAT(I5,3XE10.3,3XE10.3,3XE10.3,4XE10.3,3XE10.3,3XE1
     10.3)
     PRINT 1230
1230  FORMAT(/* STRESS AND STRAIN IN THE COMPOSITE*/)
     PRINT 1228
     PRINT 1229,(I,(STRESS(2,K,I),K=1,3),(STRANN(2,K,I),K=1
     1,3),I=1,MX,NC)
     SUM=0.
     DX=TX/NC
     DO 1232 I=1,MX,NC
     DY=TY/NR
     SUM=SUM+DY*(STRANN(2,2,I)-STRANN(1,2,I))*D(MX+I)
1232 CONTINUE
     PRINT 1251,SUM
1251 FORMAT(/* ENERGY RELEASE ON MINOR AXIS IS*E11.3/)
     CALL XINC(SUM,XNCY,DAS,DFS)
     CPR(KOUNT)=DAS
     DPR(KOUNT)=DFS
     IF(XKSTIF.GE.56000.)GO TO 1005
     TNC=TNC+XNCY
     IF(TNC.GE.FCYC)GO TO 1003
     B1=F*A1
     PRINT 42,TNC
  42 FORMAT(/* APPLIED CYCLES=*E10.3)
     PRINT 555,DAS,DFS
 555 FORMAT(* DA/DN BEFORE CYCLE INCREMENT IS*E11.3/
    1* DB/DN BEFORE CYCLE INCREMENT IS*E11.3/)
     PRINT 40,XNCY,A1,B1,P1,P2
    1* MAXIMUM DEBOND HEIGHT=*E10.3* P1=*E10.3* P2=*E10.3/)
  40 FORMAT(5X*INCREMENT CYCL=*E10.3*  CRACK,LENGTH=*E10.3
     FTNC(KOUNT)=TNC
     FXNCY(KOUNT)=XNCY
     FA1(KOUNT)=A1
     FB1(KOUNT)=B1
     IF(A1.GT.2)GO TO 1001
     GO TO 1004
   1 FORMAT(20X*MODULUS OF THE CRACKED SHEET
    1   *,E12.3)
   2 FORMAT(20X*THICKNESS OF THE CRACKED SHEET
    1   *,E12.3)
   3 FORMAT(20X*MINOR AXIS HEIGHT IN PERCENT CRACK LENGTH
    1   *,E12.3)
   4 FORMAT(20X*INCREMENTS TO MAXIUMUM CRACK LENGTH
    1   *,I12)
   7 FORMAT(20X*REMOTE APPLIED STRESS
    1   *,E12.3)
   8 FORMAT(20X*INITIAL CRACK LENGTH BEFORE CYCLING
    1   *E12.3)
   9 FORMAT(/25X*INCREMENT *I5,4X*CRACK LENGTH *F10.3/)
  10 FORMAT(5E12.3)
```

```
   11 FORMAT(20X*LOCATION      NODE    DEBOND HEIGHT*6X
     1*X-COEFFICIENT*8X*Y-COEFFICIENT*7X*X-COEFFICIENT*
     27X*Y-COEFFICIENT*/)
   12 FORMAT(22XF5.3,9XI2,10XF5.3,4(10XE10.3))
   14 FORMAT(/23X*K-BOND*5X*K-UNSTIFFEND*5X*K-STIFFENED*5X
     1*K-FACTOR*/)
   15 FORMAT(20X,3(E10.3,5X),E10.3/)
    5 FORMAT(20X*SECONDARY SHEAR MODULUS AFTER YIELDING
     1    *E12.3)
    6 FORMAT(20X*YIELD STRESS OF MODULUS IN UNIAXIAL TENSION
     1    *E12.3)
   18 FORMAT(20X*COMP MODULUS PARALLEL TO LOAD
     1    *,E12.3)
   19 FORMAT(20X*THICKNESS OF THE REINFORCEMENT SHEET
     1    *,E12.3)
   20 FORMAT(20X*POISSONS RATIO FOR THE CRACKED SHEET
     1    *,E12.3)
   21 FORMAT(20X*COMP POISSONS RATIO TRANSV TO LOAD AXIS
     1    *,E12.3)
   22 FORMAT(20X*NUMBER OF ELLIPSES IN GRID
     1    *I12)
   23 FORMAT(20X*NUMBER OF LINES IN GRID
     1    *I12)
   24 FORMAT(20X*ADHESIVE THICKNESS
     1    *,E12.3)
   25 FORMAT(20X*SHEAR MODULUS OF THE ADHESIVE
     1    *,E12.3)
   26 FORMAT(20X*COMP MODULUS TRANSV TO LOAD
     1    *,E12.3)
   27 FORMAT(20X*SHEAR MODULUS OF COMPOSITE
     1    *,E12.3)
   30 FORMAT(20X*NUMBER OF COLUMNS FOR BOUNDARY POINTS
     1    *,I12)
   31 FORMAT(20X*NUMBER OF ROWS FOR BOUNDARY POINTS
     1    *,I12)
   33 FORMAT(20X*FINAL NUMBER OF APPLIED LOAD CYCLES
     1    *,E12.3)
   34 FORMAT(20X*INITIAL CRACK LENGTH
     1    *,E12.3)
 1005 PRINT 38,INC
   38 FORMAT(5X*SPECIMEN FAILED BEFORE*E10.3*CYCLES*/)
      GO TO 1001
 1003 PRINT 39,FCYC
   39 FORMAT(5X* THE SPECIFIED NUMBER OF LOAD CYCLES HAS*
     1* BEEN MET*E11.3)
 2002 FORMAT(/)
 1001 CONTINUE
      M=M/2
      N=N/2
      LOUNT=KOUNT-1
      PRINT 540
```

```
  540 FORMAT(/13X*DELTA-M* 11X*TOTAL-M* 18X*A* 16X*DA/DM* 18X*B*
     116X*DB/DM*/)
      PRINT 536,(FXNCY(I),FTNC(I),FA1(I),CHR(I),FB1(I),DPR(I
     1),I=1,LOUNT)
  536 FORMAT(6E20.3)
      IF (TEST.NE.0.) GO TO 1000
      END
      SUBROUTINE INVER(S,AI,D)
C
C   THIS ROUTINE INVERTS A 3X3 MATRIX
C
      DIMENSION A(3,3),AI(3,3),AG(3,3),S(3,3)
      D=S(1,1)*S(2,2)*S(3,3)+S(1,2)*S(2,3)*S(3,1)+S(1,3)*
     1S(2,1)*S(3,2)
     2-(S(1,3)*S(3,1)*S(2,2)+S(1,2)*S(2,1)*S(3,3)+S(1,1)*
     3S(3,2)*S(2,3))
      AG(1,1)=S(2,2)*S(3,3)-S(2,3)*S(3,2)
      AG(1,2)=-S(2,1)*S(3,3)+S(2,3)*S(3,1)
      AG(1,3)=S(2,1)*S(3,2)-S(2,2)*S(3,1)
      AG(2,1)=-S(1,2)*S(3,3)+S(1,3)*S(3,2)
      AG(2,2)=S(1,1)*S(3,3)-S(1,3)*S(3,1)
      AG(2,3)=-S(1,1)*S(3,2)+S(1,2)*S(3,1)
      AG(3,1)=S(1,2)*S(2,3)-S(1,3)*S(2,2)
      AG(3,2)=-S(1,1)*S(2,3)+S(1,3)*S(2,1)
      AG(3,3)=S(1,1)*S(2,2)-S(1,2)*S(1,2)
      DO 1 I=1,3
      DO 1 J=1,3
       AI(I,J)=AG(J,I)/D
    1 CONTINUE
      RETURN
      END
      SUBROUTINE MULT(A,B,C)
C
C   THIS ROUTINE MULTIPLIES TWO MATRICES
C
      DIMENSION A(3,3),B(3),C(3)
      DO 1 I=1,3
      SUM=0.0
      DO 2 K=1,3
    2 SUM=SUM+A(I,K)*B(K)
      C(I)=SUM
    1 CONTINUE
      RETURN
      END
      SUBROUTINE SIMQ(A,B,N,KS)
C     SOLUTION OF THE LINEAR ALGEBRAIC SYSTEM OF EQUATIONS
C     OF THE FORM
C     AX=B
C     A - NXN MATRIX OF COEFFICIENTS
C     B - VECTOR FOR THE RIGHTHAND-SIDE OF THE SYSTEM OF
C     EQUATIONS
```

```
C      N- NUMBER OF EQUATIONS AND VARIABLES
C      KS - OUTPUT DIGIT
C           0 FOR A NORMAL SOLUTION
C           1 FOR A SINGULAR SET OF EQUATIONS
       DIMENSION A(1),B(1)
       TOL=0.0
       KS=0
       JJ=-N
       DO 65 J=1,N
       JY=J+1
       JJ=JJ+N+1
       BIGA=0.0
       IT=JJ-J
       DO 30 I=J,N
       IJ=IT+I
       IF(ABS(BIGA)-ABS(A(IJ))) 20,30,30
   20  BIGA=A(IJ)
       IMAX=I
   30  CONTINUE
       IF(ABS(BIGA)-TOL) 35,35,40
   35  KS=1
       RETURN
   40  I1=J+N*(J-2)
       IT=IMAX-J
       DO 50 K=J,N
       I1=I1+N
       I2=I1+IT
       SAVE=A(I1)
       A(I1)=A(I2)
       A(I2)=SAVE
   50  A(I1)=A(I1)/BIGA
       SAVE=B(IMAX)
       B(IMAX)=B(J)
       B(J)=SAVE/BIGA
       IF (J-N) 55,70,55
   55  IQS=N*(J-1)
       DO 65 IX=JY,N
       IXJ=IQS+IX
       IT=J-IX
       DO 60 JX=JY,N
       IXJX=N*(JX-1)+IX
       JJX=IXJX+IT
   60  A(IXJX)=A(IXJX)-(A(IXJ)*A(JJX))
   65  B(IX)=B(IX)-(B(J)*A(IXJ))
   70  NY=N-1
       IT=N*N
       DO 80 J=1,NY
       IA=IT-J
       IB=N-J
       IC=N
       DO 80 K=1,J
```

```
      B(IB)=B(IB)-A(IA)*B(IC)
      IA=IA-N
   80 IC=IC-1
      RETURN
      END
      SUBROUTINE FORM(N,M)
C
C  THIS ROUTINE FORMS THE COEFFICEINT MATRICES USED TO SOLVE
C  FOR ELASTIC INTERLAMINAR STRESSES
C
      DIMENSION THETA(10)
      COMMON/XLIMIT/DC(2,51),DB(6,51),FF
      COMMON/ROT/Z9(10000),D(100),NALF
      COMMON/TOP/E3,T2,V1,SMX,SMY,G,CONS,Q,A1,SCON
      COMMON/BOT/E4,T4,V4,SCX,SCY,GB,CONB,Q1,GC,E5
      COMMON/ADHES/TAD,GAD
      COMMON/BOND/F,P1,P2,XKF,XKUNS,XKSTIF
      COMMON/BOND2/NE,NL,NT,XC(100),YC(100),XA(100),YA(100),
     1NOP(100)
      COMMON/CTOL/TOL,NC,NR,TX,TY,NBC(100),LBC
      COMPLEX Z,CI,F1,G2
      EXTERNAL F1,G2
      CI=CMPLX(0.,1.0)
      A=A1
      O=M/2
      P=N/2
      L=P
      MX=NC*NR
      K=0
C
C ASSEMBLE RIGHTHAND SIDE VECTOR
C
      PRINT 57
   57 FORMAT(/* NODE NUMBER*8X*X-COR*8X*Y-COR*/)
      PRINT 56,(I,DC(1,I),DC(2,I),I=1,MX)
   56 FORMAT(I10,2E15.3)
      DO 101 I=1,K
      X=DC(1,I)
      Y=DC(2,I)
      Z=X+CI*Y
      CALL REMTU(DU,DV,Z)
      CALL REMBU(BU,BV,Z)
      D(I)=DU-BU
      D(K+I)=DV-BV
      DO 102 J=1,MX
      CALLXINTG(Z,J,A,C1,C2,C3,C4,F1,1 )
      CALL XINTG(Z,J,A,B1,B2,B3,B4,F1,2 )
  802 CONTINUE
      I1=I
      J1=J
      IV1=(J1-1)*N+I1
```

```
      Z9(IV1)=C1+B1
      IF(I.EQ.J)Z9(IV1)=Z9(IV1)+TAD/GAD
      I2=I
      J2=J+L
      IV2=(J2-1)*N+I2
      Z9(IV2)=C2+B2
      I3=I+K
      J3=J
      IV3=(J3-1)*N+I3
      Z9(IV3)=C3+B3
      I4=I+K
      J4=J+L
      IV4=(J4-1)*N+I4
      Z9(IV4)=C4+B4
      IF(I4.EQ.J4)Z9(IV4)=Z9(IV4)+TAD/GAD
  102 CONTINUE
  101 CONTINUE
  104 CONTINUE
   20 CONTINUE
      RETURN
      END
      SUBROUTINE REMTU(U,V,Z)
C
C CALCULATE DISPLACEMENTS IN THE TOP SHEET DUE TO A REMOTE
C STRESS
C
      COMMON/TOP/E3,T2,V1,SMX,SMY,G,CONS,Q,A1,SCON
      COMPLEX CI,Z,ZI,ZB,CXSR,D,DPHI,PHI,DOMEGA
      CI=CMPLX(0.,1.)
      ZB=CONJG(Z)
      D=CXSR(Z,A1)
      DPHI=.5*SMY*D-.25*Z*(SMY-SMX)
      PHI=.5*SMY*Z/D-.25*(SMY-SMX)
      DOMEGA=.5*SMY*CXSR(ZB,A1)+.25*(SMY-SMX)*ZB
      D=(Q*DPHI-DOMEGA-(Z-ZB)*CONJG(PHI))/(2.*G)
      U=REAL(D)
      V=AIMAG(D)
      RETURN
      END
      SUBROUTINE REMBU(U,V,Z)
C
C CALCULATES DISPLACEMENTS IN THE BOTTOM SHEET DUE TO A
C REMOTE STRESS
C
      COMMON/BOT/E4,T4,V4,SCX,SCY,GB,CONB,Q1,GC,E5
      COMPLEX Z
      X=REAL(Z)
      Y=AIMAG(Z)
      S12=-V4/E5
      U=(SCX/E5+S12*SCY)*X
      V=(S12*SCX+SCY/E4)*Y
```

```
      RETURN
      END
      COMPLEX FUNCTION F1(Z,ZO)
C
C  EVALUATE INTEGRAL OF B(Z,ZO)
C
      COMPLEX Z,ZO,ZB,ZOB,XA,XB,XC,CXSR,CI,D,B,R
      COMPLEX H,H1,H2,BI
      DIMENSION N(300)
      COMMON/TOP/E3,T2,V1,SMX,SMY,G,CONS,Q,A1,SCON
      COMMON/KK/KCOUNT
C
C  COUNTER LIMITS INTEGRATION INTERVAL TO 50 STEPS
C
C  USE COMMON TO ZERO COUNTER
C
      XA(Z,ZO)=CLOG((Z*ZO-A**2-CXSR(Z,A)*CXSR(ZO,A))/(Z*ZO+A
     2**2-
     2CXSR(Z,A)*CXSR(ZO,A))*(-1.))
      XB(Z,ZO)=CLOG((Z*ZO-A**2-CXSR(Z,A)*CXSR(ZO,A))*(Z+ZO)*
     1*2/(
     2(Z*ZO+A**2-CXSR(Z,A)*CXSR(ZO,A))*(ZO-Z)**2))
      XC(Z,ZO)=(Z-ZO*CXSR(Z,A)/CXSR(ZO,A))*(ZOB-ZO)/(Z**2-
     1ZO**2)
      G1=G
      ZB=CONJG(Z)
      ZOB=CONJG(ZO)
      CI=CMPLX(0.,1.)
C
C  SAVE PREVIOUS VALUES OF XB AND CHECK PATH FOR BRANCH CUT
C  IF BRANCH IS CROSSED ADD PROPER IMAGINARY TERM TO KEEP
C  DISPLACEMENTS CONTINUOUS
C
      KCOUNT=KCOUNT+1
      K=KCOUNT
      A=A1
      BI=.5*(XB(Z,ZO)-Q*XB(Z,ZOB))+XC(Z,ZO)
      X=REAL(XB(Z,ZOB))
      Y=AIMAG(XB(Z,ZOB))
      I=1
      IF(X.LT.0.AND.Y.GE.0)I=2
      IF(X.LT.0.AND.Y.LT.0)I=3
      D=XB(Z,ZOB)
      IF(K.LE.2) GO TO 100
      IF(N(K-2).EQ.2.AND.I.EQ.3)D=D-6.283*CI
      IF(N(K-2).EQ.3.AND.I.EQ.2)D=D+6.283*CI
  100 CONTINUE
      N(K)=I
C
C
C
```

```
      H1=-Q*XC(Z,ZO)
      H=-Q*REAL(XA(Z,ZO))
      H2=.5*(Q**2*D+CONJG(D))
      R=H+H1+H2
      F1=R+XC(ZB,ZO)+2*(Z*ZO-ZOB*ZB)/(ZB**2-ZO**2)+(Z-ZB)*B(
     1ZB,ZO)
      G1=3.75*10**6
      F1=F1*CONS
      D1=REAL(D)
      D2=AIMAG(D)
      RETURN
      END
      SUBROUTINE XINTG(Z,I,A,S11,S12,S21,S22,F1,IC)
C
C   THIS ROUTINE INTEGRATES THE SUM AND DIFFERENCE OF TWO
C   COMPLEX FUNCTIONS, F1 AND F2, USED TO EVALUATE THE GREENS
C   FUNCTIONS FOR DISPLACEMENTS.
C
      COMMON/CTOL/TOL,NC,NR,TX,TY,NBC(100),IBC
      COMMON/KK/KCOUNT
        COMPLEX F1,F2,Z,ZO,CI,A1,B1,ZOB
      COMMON/XLIMIT/DC(2,51),DB(6,51),FF
      EXTERNAL F1
      CI=CMPLX(0.,1.)
      X=REAL(Z)
      S11=0.0
      S12=0.0
      S21=0.0
      S22=0.0
      Y=AIMAG(Z)
C
C   IF INDEX=1 THEN Z LIES OUTSIDE INTEGRATION PATCH
C   AND K1 POINTS ARE USED IN A SINGLE INTEGRATION.
C   IF INDEX=2 THEN THEN Z LIES WITHIN THE INTEGRATION PATCH
C   AND TWO INTEGRATIONS ARE MADE  WITH K2 POINTS IN EACH
C   INTEGRATION.
C   ICOUNT CONTROLS THE LOOPS ON THE INTEGRATION.  IF ICOUNT
C   EQUALS 0 CONTINUE OTHERWISE DO SECOND INTEGRATION.
C
      XSTART=DB(1,I)
      XFINAL=DB(2,I)
      IF(X.LE.XSTART.OR.X.GE.XFINAL)INDEX=1
      IF(X.GT.XSTART.AND.X.LT.XFINAL)INDEX=2
      ICOUNT=0
      K1=5
      K1=5
      IF(INDEX.EQ.1)2,3
    2 XL=XSTART
      XU=XFINAL
      GO TO 4
    3 XL=XSTART
```

```
      XU=X-TOL
      ICOUNT=ICOUNT+1
      GO TO 4
    5 XU=XFINAL
      XL=X+TOL
      ICOUNT=ICOUNT+1
    4 CONTINUE
      IF(XFINAL.EQ.A)XFINAL=A-TOL
      K=K1
      DX=(XU-XL)/(3.*K)
      M=K+1
      DO 7 L=1,M
       XX=(XU-XL)*(L-1)
      XO=XX/K+XL
      AT=I
      X1=AT/2.
      X2=L/2
       IF(L.EQ.1.OR.L.EQ.M)16,18
   16  XF=1
       GO TO 17
   18     IF(ABS(X1-X2).LT..0001)XF=4.
      IF(ABS(X1-X2).GT..0001)XF=2.
   17     CONTINUE
      ZO=XO+CI*0.0
      YO=AIMAG(ZO)
      ZOB=CONJG(ZO)
      KCOUNT=0.0
      CALL YINTG(Z,ZO,I,A,T11,T12,T21,T22,F1,IC)
  201 FORMAT(/* Y-STRIP AT XO=*E10.3*T1,T2,T3,T4=*4E11.3)
      C11=XF*DX*T11
      C12=XF*DX*T12
      C21=XF*DX*T21
      C22=XF*DX*T22
      S11=S11+C11
      S12=S12+C12
      S21=S21+C21
      S22=S22+C22
    7 CONTINUE
      IF(ICOUNT-1)6,5,6
    6 CONTINUE
      RETURN
      END
      SUBROUTINE YINTG(Z,ZO,I,A,S11,S12,S21,S22,F1,IC)
C
C  THIS ROUTINE INTEGRATES THE SUM AND DIFFERENCE OF TWO
C  COMPLEX FUNCTIONS, F1 AND F2, USED TO EVALUATE THE GREENS
C  FUNCTIONS FOR DISPLACEMENTS.
C
      COMPLEX H,A2,B2
      COMMON/CPARM/S1,S2,C11,C12,C22,C21,P1,P2,Q4,Q2
      COMPLEX Z1,Z2,W1,W2,G,GB,S1,S2,C11,C12,C22,C21,P1,P2,Q
     14,Q2
```

```
      COMMON/XLIMIT/DC(2,51),DB(6,51),FF
      COMMON/CTOL/TOL,NC,NR,TX,TY,NBC(100),LBC
        COMPLEX F1,F2,Z,ZO,CI,A1,B1,ZOB
      COMMON/ROT/Z9(10000),D(100),NALF
      CI=CMPLX(0.,1.)
      XO=REAL(ZO)
      X=REAL(Z)
      S11=0.0
      S12=0.0
      S21=0.0
      S22=0.0
      Y=AIMAG(Z)
      B1=DB(3,I)
      B2=DB(4,I)
      C1=DB(5,I)
      C2=DB(6,I)
      Y1=YYX(XO,B1,B2)
      Y2=YYX(XO,C1,C2)
      ICOUNT=0
      K1=3
      K1=5
      XL=Y1
      XU=Y2
      II=1
      IF(II.EQ.1)GO TO 4
C
C   LOGIC TO STATEMENT FOUR IS FOR THE NARROW STRIP THAT
C   CONTAINS THE SINGULARITY
C   THESE STATEMENTS CAN BE USED TO INTEGRATE THIS STRIP WITH
C   ADDITIONAL LOGIC.  CONSIDER X CONSTANT OVER THIS NARROW
C   STRIP
C
      IF(Y.LE.Y1.OR.Y.GE.Y2)INDEX=1
      IF(Y.GT.Y1.AND.Y.LT.Y2)INDEX=2
      IF(INDEX.EQ.1)2,3
    2 XL=Y1
      XU=Y2
      GO TO 4
    3 XL=Y1
      XU=Y-TOL
      ICOUNT=ICOUNT+1
      GO TO 4
    5 XL=Y+TOL
      XU=Y2
      K1=5
      ICOUNT=ICOUNT+1
    4 CONTINUE
      K=K1
      DX=(XU-XL)/(3.*K)
      M=K+1
      DO 1 I=1,M
```

```
      XX=(XU-XL)*(L-1)
      YO=XX/K+XL
      AT=L
      X1=AT/2.
      X2=L/2
      IF(L.EQ.1.OR.L.EQ.M) 16,18
 16   XF=1
      GO TO 17
 18      IF(ABS(X1-X2).LT..0001)XF=4.
      IF(ABS(X1-X2).GT..0001)XF=2.
 17      CONTINUE
      ZO=XO+CI*YO
      ZOB=CONJG(ZO)
C
C  IC=1    CRACKED METAL SHEET
C  IC=2 ORTHOTROPIC SOLID SHEET
C
      IF(IC.NE.2)30,31
   30 CONTINUE
      A1=F1(Z,ZO)
      B1=F1(Z,ZOB)
      T11=REAL(A1+B1)
      T12=REAL(CI*(A1-B1))
      T21=AIMAG(A1+B1)
      T22=AIMAG(CI*(A1-B1))
      GO TO 33
   31 CONTINUE
      Z1=X+S1*Y
      Z2=X+S2*Y
      W1=XO+S1*YO
      W2=XO+S2*YO
      A1=G(Z1,W1)
      B1=G(Z2,W2)
      A2=H(Z1,W1)
      B2=H(Z2,W2)
         T11=2.*REAL(P1*C11*A1+P2*C21*B1)
      T12=2.*REAL(P1*C12*A2+P2*C22*B2)
      T21=2.*REAL(Q4*C11*A1+Q2*C21*B1)
         T22=2.*REAL(Q4*C12*A2+Q2*C22*B2)
   33 CONTINUE
      IF(IC.NE.3)60,61
   60 FS=1.
      FR=1.
      GO TO 62
   61 CONTINUE
      FS=D(I)
      FR=D(I+HALF)
   62 CONTINUE
      P11=XF*FS*DX*T11
      P12=XF*FR*DX*T12
      P21=XF*FS*DX*T21
```

```
      P22=XF*FR*DX*T22
      S11=S11+P11
      S12=S12+P12
      S21=S21+P21
      S22=S22+P22
    1 CONTINUE
      IF(ICOUNT-1)6,5,6
    6 CONTINUE
      RETURN
      END
        COMPLEX FUNCTION CXSR(Z,B)
C
C     THIS FUNCTION TAKES THE SQUARE ROOT OF Z**2-B**2
C     IT ONLY RETURNS THE FIRST ROOT, THE SECOND ROOT CAN BE
C     FOUND BY ADDING PI/2 TO THE TRIP ARGUMENT
C
      COMPLEX Z,T1,T2,CI
        CI=CMPLX(0.,1.)
      T1=Z-B
      T2=Z+B
       X1=REAL(T1)
         Y1=AIMAG(T1)
        X2=REAL(T2)
        Y2=AIMAG(T2)
        A1=ATAN2(Y1,X1)
        A2=ATAN2(Y2,X2)
      S1=(REAL(T1)**2+AIMAG(T1)**2)**.5
      S2=(REAL(T2)**2+AIMAG(T2)**2)**.5
      SR=(S1*S2)**.5
      ANG=A1+A2
        CXSR=SR*(COS(ANG/2.0)+CI*SIN(ANG/2.))
        RETURN
        END
      COMPLEX FUNCTION XK(Z,ZO)
C
C  GREENS FUNCTION FOR STRESS INTENSITY
C
      COMMON/TOP/E3,T2,V1,SMX,SMY,G,CONS,Q,A1,SCON
      COMPLEX Z,ZO,ZB,ZOB,CXSR,D,F
      A=A1
      ZB=CONJG(Z)
      ZOB=CONJG(ZO)
      D=(ZO*ZOB-2.*ZO**2+A**2)/((ZO**2-A**2)*CXSR(ZO,A))
      F=Q*CXSR(ZOB,A)/(ZOB**2-A**2)
       XK=2*A**.5*(F+D)/(6.283*(1.+Q)*T2)
      RETURN
      END
      FUNCTION YY(T)
C
C  T IS A DUMMY PARAMETER FOR XO
C  CALCULATE YO FOR A GIVEN XO
```

```
C
      COMMON/TOP/E3,T2,V1,SMX,SMY,G,CONS,Q,A1,SCON
      COMMON/BOND/F,P1,P2,XKF,XKUNS,XKSTIFF
      IF(T/A1.LE.0)2,1
    1 CONTINUE
      YY=F*((1-(T/A1)**2)**(1/P2))*A1
      GO TO 3
    2   YY=F*A1
    3 CONTINUE
      RETURN
      END
      COMPLEX FUNCTION B(Z,ZO)
      COMMON/TOP/E3,T2,V1,SMX,SMY,G,CONS,Q,A1,SCON
      COMPLEX X1,X2,X3,X4,X5,CXSR,ZOB,ZO,Z,X6,X7,X8,X9
       Q1=Q
      A=A1
      ZOB=CONJG(ZO)
      X1=CXSR(Z,A)
      X2=CXSR(ZO,A)
      X3=1./(Z**2-ZO**2)
      X4=1./(Z**2-ZOB**2)
      X5=1./(Z-ZO)**2
      X6=1./(Z+ZO)**2
      X7=X1*((-4*ZO*X3)+2.*Q1*ZOB*X4+(Z-ZOB)*X5-(Z+ZOB)*X6)
      X8=(ZO-ZOB)*((A**2-Z*ZO)*X5-(A**2+Z*ZO)*X6)/X2+2.*X2*
     1X3*Z
      X9=-2.*Q1*Z*CXSR(ZOB,A)*X4
       B=(X7+X8+X9)/(2.0*X1)
      RETURN
        END
      SUBROUTINE CPAR
C
C  CALCULATE PARAMTERS FOR COMPLEX VARIABLES IN ORTHOTROPIC
C  ANALYSIS.
C
      COMPLEX CI,S1,S1B,S2,S2B,C11,C12,C21,C22,P1,P2,Q4,Q2,D
     1,U1,U2
      COMPLEX CC
      COMMON/BOT/E4,T4,V4,SCX,SCY,GB,CONB,Q1,GC,E5
      COMMON/CLARK/S1,S2,C11,C12,C22,C21,P1,P2,Q4,Q2
      CI=CMPLX(0.0,1.0)
      EX=E5
      EY=E4
        VX=V4
        GXY=GC
      B=EX/GXY-2*VX
      C=EX/EY
      CC=CMPLX(C,0.0)
        VY=VX*EY/EX
      D=CSQRT(B**2-4.*CC)
      U1=-.5*(B-D)
```

```
      U2=-.5*(B+D)
      S1=CSQRT(U1)
      IF(AIMAG(S1).LT.0)S1=-S1
      S2=CSQRT(U2)
      IF(AIMAG(S2).LT.0)S2=-S2
      S1B=CONJG(S1)
      S2B=CONJG(S2)
      IF(B**2-4.*C)1,2,3
    1 CONTINUE
      PRINT 4
    4 FORMAT(* ROOTS ARE COMPLEX U1=A+IB, U2=-A+IB*/)
      GO TO 5
    2 CONTINUE
      PRINT 6
    6 FORMAT(* ROOTS ARE PURE IMAGINARY AND EQUAL*/)
      GO TO 5
    3 B1=AIMAG(S1)
      D1=AIMAG(S2)
      P1=(S1**2-VX)/EX
      P2=(S2**2-VX)/EX
      Q2=(-VY*S2+1./S2)/EY
      Q4=(-VY*S1+1./S1)/EY
  100 FORMAT(4E12.3)
      COMP1=1./(12.566*T4*(B1**2-D1**2))
      C11=(D1**2*VY+1)*B1*COMP1
      C12=(VX+D1**2)*COMP1
      C21=-D1*(VY*B1**2+1)*COMP1
      C22=-(B1**2+VX)*COMP1
      GO TO 7
    5 PRINT 8
    8 FORMAT(/* ERROR-ERROR ORTHOTROPIC ANALYSIS IS NOT*
     1* DEFINED    */)
    7 CONTINUE
      RETURN
      END
      SUBROUTINE GRID
C
C  GENERATE MESH USED TO DISCRETIZE INTERLAMINAR STRESSES.
C
      COMMON/BOND2/NE,NL,NT,XC(100),YC(100),XA(100),YA(100),
     1NOP(100)
      COMMON/CTOL/TOL,NC,NR,TX,TY,NBC(100),LBC
      COMMON/TOP/E3,T2,V1,SMX,SMY,G,CONS,Q,A1,SCON
      COMMON/XLIMIT/DC(2,51),DB(6,51),FF
      COMMON/BOND/F,P1,P2,XKF,XKUNS,XKSTIF
      P=P1
      TXX=2.*TOL
      DX=TX/NC
      DY=TY/NR
      LBC=0
      MX=NC*NR
```

```
      DO 11 I=1,MX
   11 NBC(I)=0
      DO 100 J=1,NR
      DO 100 I=1,NC
      MT=NC*(J-1)+I
      AC=A1+DY*(J-1)+DY/2.
      YI=F*A1
      BC=YI+DY*(J-1)+DY/2.
      DC(1,MT)=DX/2.+(I-1)*DX
      X=DC(1,MT)
      Y=YYD(X,BC,AC,P)
      DC(2,MT)=Y
      DB(1,MT)=DX*(I-1)
      DB(2,MT)=DX*I
      DB(3,MT)=DY*(J-1)+YI
      DB(4,MT)=DY*(J-1)+A1
      DB(5,MT)=DY*J+YI
      DB(6,MT)=DY*J+A1
  100 CONTINUE
  110 FORMAT(I10,2E15.3)
  120 FORMAT(I10,6E12.3)
      RETURN
      END
      SUBROUTINE XINC(SUM,XNCY,DAS,DFS)
C
C  THIS ROUTINE INCREMENTS THE CRACK LENGTH AND DEBOND SHAPE
C  FOR NCY CYLES
C
       COMMON/XLIMIT/DC(2,51),DB(6,51),FF
      COMMON/CTOL/TOL,NC,NR,TX,TY,NBC(100),LBC
      COMMON/BOND/F,P1,P2,XKF,XKUNS,XKSTIFF
      COMMON/TOP/E3,T2,V1,SMX,SMY,G,CONS,Q,A1,SCON
      COMMON/BOT/E4,T4,V4,SCX,SCY,GB,CONB,Q1,GC,E5
      COMMON/XY/XD,YD
      DIMENSION YN(20),XN(20),BI(20,2),CI(20),D(20),CR(2,2)
      B1=A1*F
      R=.01
      DA=3.22E-14*XKSTIFF**3.38
      CFAC=1.79E-14
      CFAC=3.36E-14
      DA=CFAC*XKSTIFF**3.38
      DA=DA/((1.-R)*56000.-XKSTIFF)
      DF=3.158E-05*SUM**3.616
      DAS=DA
      DFS=DF
C
C  DETERMINE HOW MANY CYCLES REQUIRED FOR EITHER A CRACK OR
C  DEBOND EXTENSION OF .1 INCHES. THEN USE SMALLEST VALUE
C  AS THE INCREMENT OF APPLIED LOAD CYCLES
C
      XNCRACK=.10/DA
```

```
      XNBOND=.10/DF
      XNBOND=.20/DF
      XNCY=XNCRACK
      IF(XNCRACK.GT.XNBOND)XNCY=XNBOND
      DA=XNCY*DA
      A2=A1+DA
      DF=DF*XNCY
      B2=B1+DF
      P1=2
      A1=A2
      F=B2/A2
      RETURN
      END
      SUBROUTINE VERI(Z,SXX,SXY,SXXY,SYX,SYY,SYXY,MX,KTYPE)
C
C   INTEGRATE GREENS FUNCTIONS FOR STRESSES
C
      COMMON/CTOL/TOL,NC,NR,TX,TY,NBC(100),LBC
      COMPLEX Z
      Z=Z
      MX=MX
      J=J
      SXX=0.
      SXY=0.
      SXXY=0.
      SYX=0.
      SYXY=0.
      SYY=0.0
      DO 1 J=1,MX
      CALL VXINTG (J,Z,S1,S2,S3,S4,S5,S6,MX,KTYPE)
C
C   FIRST INDEX INDICATES LOAD DIRECTION, SECOND STRESS
C   DIRECTION
C
      SXX=S1+SXX
      SXY=S3+SXY
      SXXY=S5+SXXY
      SYX=S2+SYX
      SYY=S4+SYY
      SYXY=S6+SYXY
    1 CONTINUE
      RETURN
      END
      SUBROUTINE VXINTG(I,Z,S1,S2,S3,S4,S5,S6,MX,KTYPE)
C
C   DETERMINE STRESSES IN ADHERENDS DUE TO INTERLAMINAR
C   STRESSES.
C
      COMMON/XLIMIT/DC(2,51),DB(6,51),FF
      COMMON/ROT/Z9(10000),D(100),NALF
      COMMON/TOP/E3,T2,V1,SMX,SMY,G,CONS,Q,A1,SCON
```

```
      COMPLEX Z,ZB,ZO,ZOB,B,DBZ,B1,DB1B,B1B,DB1,G5,G6,G7,G8
      COMMON/CTOL/TOL,NC,NR,TX,TY,NBC(100),LBC
      COMPLEX CI
      COMPLEX P
      P=Z
      X=REAL(Z)
      S1=0
      S2=0
      S3=0
      S4=0
      S5=0
      S6=0
      ZB=CONJG(Z)
C
C   IF INDIX=1 THEN Z LIE OUTSIDE THE INTEGRATION PATCH
C   AND K1 POINTS ARE USED IN A SINGLE INTEGRATION
C   IF INDEX=2 THEN Z LIES WITHIN THE INTEGRATION PATCH AND
C   TWO INTEGRATIONS ARE MEADE EACH WITH K2 INTEGRATION POINT
C   IF ICOUNT=0 THEN CONTINUE OTHERWISE SECOND INTEGRATION
C
      XSTART=DB(1,I)
      XFINAL=DB(2,I)
      IF(X.LE.XSTART.OR.X.GE.XFINAL)INDEX=1
      IF(X.GT.XSTART.AND.X.LT.XFINAL)INDEX=2
      K1=3
      K1=5
      ICOUNT=0
      IF(INDEX.EQ.1)2,3
    2 XL=XSTART
      XU=XFINAL
      GO TO 4
    3 XL=XSTART
      XU=X-TOL
      ICOUNT=ICOUNT+1
      GO TO 4
    5 XU=XFINAL
      XL=X+TOL
      ICOUNT=ICOUNT+1
    4 CONTINUE
      IF(XFINAL.EQ.A1)XFINAL=A1-TOL
      Y=K1
      DX=(XU-XL)/(3.*K)
      M=K+1
      CI=CMPLX(0.,1.0)
      DO 7 L=1,M
      XX=(XU-XL)*(L-1)
      XO=XX/K+XL
      YO=YY(XO)
      ZO=XO+CI*YO
      ZOB=CONJG(ZO)
      AT=I
```

```
      X1=AT/2.
      X2=L/2
      IF(L.EQ.1.OR.L.EQ.M) 16,18
   16 XF=1
      GO TO 17
   18 IF(ABS(X1-X2).LT..0001)XF=4
       IF(ABS(X1-X2).GT..0001)XF=2
   17 CONTINUE
      CALL VYINTG(Z,ZO,I,TXX,TXY,TYX,TYY,TXYX,TXYY,KTYPE)
      S1=XF*DX*TXX+S1
      S2=XF*DX*TXY+S2
      S3=XF*DX*TYX+S3
      S4=XF*DX*TYY+S4
      S5=XF*DX*TXYX+S5
      S6=XF*DX*TXYY+S6
    7 CONTINUE
      IF(ICOUNT-1)6,5,6
    6 CONTINUE
      RETURN
      END
       SUBROUTINE VYINTG(Z,ZO,I,S7,S8,S3,S4,S5,S6,KTYPE)
C
C  INTEGRATE GREENS FUNCTIONS FOR STRESSES
C
      COMMON/CPARM/S1,S2,C11,C12,C22,C21,P1,P2,Q4,Q2
      COMMON/XLIMIT/DC(2,51),DB(6,51),FF
      COMPLEX Z1,Z2,W1,W2,   GB,S1,S2,C11,C12,C22,C21,P1,P2,Q
     14,Q2
      COMMON/TOP/E3,T2,V1,SMX,SMY,G,CONS,Q,A1,SCON
      COMMON/ROT/Z9(10000),D(100),NALF
      COMPLEX Z,ZB,ZO,ZOB,B,DBZ,B1,DB1B,B1B,DB1,G5,G6,G7,G8
      COMPLEX CI,G1A
      COMPLEX G1,G2,G3,G4,H1,H2,W1B,W2B
      COMMON/CTOL/TOL,NC,NR,TX,TY,NBC(100),IBC
      COMPLEX F
      X=REAL(Z)
      Y=AIMAG(Z)
      L=Z
      Q1=Q
      ZB=CONJG(Z)
      S7=0.
      S8=0.0
      S3=0
      S4=0
      S5=0
      S6=0
      MX=IR*NC
C
C  DB GIVES PARAMETERS FOR UPPER AND LOWER GRID BOUNDARIES.
C
      B1=DB(3,I)
```

```
      B2=DB(4,I)
      C1=DB(5,I)
      C2=DB(6,I)
      XO=REAL(ZO)
      Y2=YYX(XO,C1,C2)
      Y1=YYX(XO,B1,B2)
      K1=5
      K1=3
      XL=Y1
      XU=Y2
      K=K1
C
C   SEE YINTG FOR LOGIC FOR INTEGRATION OF NARROW STRIP THAT
C   CONTAINS THE SINGULARITY. THAT STRIP IS NEGLECTED HERE
C
      DX=(XU-XL)/(3.*K)
      M=K+1
      CI=CMPLX(0.,1.0)
      DO 7 L=1,M
      XX=(XU-XL)*(L-1)
      YO=XX/K+XL
      ZO=XO+CI*YO
      ZOB=CONJG(ZO)
      AT=L
      X1=AT/2.
      X2=L/2
      IF(L.EQ.1.OR.L.EQ.M) 16,18
   16 XF=1
      GO TO 17
   18 IF(ABS(X1-X2).LT..0001)XF=4
      IF(ABS(X1-X2).GT..0001)XF=2
   17 CONTINUE
      IF(KTYPE.EQ.1)30,31
   30 CONTINUE
      B1=B(Z,ZO)
      B1B=B(Z,ZOB)
      DB1=DBZ(Z,ZO)
      DB1B=DBZ(Z,ZOB)
           G1=-4*(ZO/(Z**2-ZO**2)+ZOB/(Z**2-ZOB**2))
         G1=REAL(G1)
         G1A=-4*(ZO/(Z**2-ZO**2)-ZOB/(Z**2-ZOB**2))
       G1A=REAL(CI*G1A)
       G2=2*Q1*ZOB/(Z**2-ZOB**2)
          G2=G2-((ZOB+ZB)/(Z+ZO)**2+(ZOB-ZB)/(Z-ZO)**2)
          G3=2*Q1*ZO/(Z**2-ZO**2)
       G3=G3-((ZO+ZB)/(Z+ZOB)**2+(ZO-ZB)/(Z-ZOB)**2)
      G5=B1+B1B
      G6=CI*(B1-B1B)
      G7=(ZB-Z)*(DB1+DB1B)
        G8=CI*(ZB-Z)*(DB1-DB1B)
        T1S=REAL(G1-G2-G3)
```

```
          T2S=REAL(G1A-CI*(G2-G3))
          T3S=REAL(G1+G2+G3)
          T4S=REAL(G1A+CI*(G2-G3))
          T5S=AIMAG(G1+G2+G3)
         T6S=AIMAG(G1A+CI*(G2-G3))
        T11=(-REAL(2*G5-G7)+T1S)*SCON
         T22=(-REAL(2*G6-G8)+T2S)*SCON
         T33=(-REAL(2*G5+G7)+T3S)*SCON
         T44=(-REAL(2*G6+G8)+T4S)*SCON
         T55=(AIMAG(-G7)+T5S)*SCON
         T66=(AIMAG(-G8)+T6S)*SCON
C
C   CHANGE SIGNS TO ACCOUNT FORNEGATIVE BODY FORCES
C
      T11=-T11
      T22=-T22
      T33=-T33
      T44=-T44
      T55=-T55
      T66=-T66
      GO TO 32
   31 CONTINUE
      Z1=X+S1*Y
      Z2=X+S2*Y
      W1=X0+S1*Y0
      W2=X0+S2*Y0
      W1B=CONJG(W1)
      W2B=CONJG(W2)
       G1=2*(W1/(Z1** 2-W1** 2)+W1B/(Z1** 2-W1B** 2))
        G2=2*(W2/(Z2** 2-W2** 2)+W2B/(Z2** 2-W2B** 2))
        H1=2*(W1/(Z1** 2-W1** 2)-W1B/(Z1** 2-W1B** 2))
        H2=2*(W2/(Z2** 2-W2** 2)-W2B/(Z2** 2-W2B** 2))
        T11=2*REAL(S1** 2*C11*G1+S2** 2*C21*G2)
         T22=2*REAL(CI*(S1** 2*C12*H1+S2** 2*C22*H2))
        T33=2*REAL(C11*G1+C21*G2)
        T44=2*REAL(CI*(C12*H1+C22*H2))
        T55=-2*REAL(S1*C11*G1+S2*C21*G2)
         T66=-2*REAL(CI*(S1*C12*H1+S2*C22*H2))
C
C   CALCULATE STRESSES IN ORTHOTROPIC SHEET
C
   32 CONTINUE
      S7=XF*DX*T11*D(I)+S7
      S8=XF*DX*T22*D(I+MX)+S8
      S3=XF*DX*T33*D(I)+S3
      S4=XF*DX*T44*D(I+MX)+S4
      S5=XF*DX*T55*D(I)+S5
      S6=XF*DX*T66*D(I+MX)+S6
    7 CONTINUE
      RETURN
      END
```

```
      COMPLEX FUNCTION DBZ(Z,ZO)
      COMMON/TOP/E3,T2,V1,SMX,SMY,G,CONS,Q,A1,SCON
C
C  THIS FUNCTION IS THE DERIVATIVE OF B(Z,ZO) WITH RESIECT
C  TO Z
C
      COMPLEX ZB,CXSR
      COMPLEX Z,ZO,B1,B2,B3,ZOB
      COMPLEX XIZO,XIZOB,XIZ
      ZB=CONJG(Z)
      ZOB=CONJG(ZO)
      A=A1
      XIZ=CXSR(Z,A)
      XIZO=CXSR(ZO,A)
      XIZOB=CXSR(ZOB,A)
      B1=(-4*Q*Z*ZOB /(Z**2-ZOB**2)**2-4*Z*(3*ZO**2*ZOB+Z**2
     1*ZOB-4*ZO**3
     2)/((ZO-Z)**3*(ZO+Z)**3))/2
      B2=-((Q*XIZOB*(A**2*ZOB**2-2*Z**4+A**2*Z**2)/(ZOB**4-2
     1*Z**2*ZOB
     2**2+Z**4)-XIZO*(A**2*ZO**2-2*Z**4+A**2*Z**2)/(ZO**4-2*
     1Z**2*ZO**2
     2+Z**4))/(Z**2-A**2)+((ZO**2+Z*ZO-2*A**2)/(ZO-Z)**3+(ZO
     1**2-Z*ZO
     3-2*A**2)/(ZO+Z)**3+Z*((A**2-Z*ZO)/(ZO-Z)**2-(Z*ZO+A**2
     1)/(ZO+Z)**2
     4)/(Z**2-A**2))*(ZO-ZOB)/(2*XIZO))/XIZ
      DBZ=B1+B2
      RETURN
      END
      SUBROUTINE RESIGM(Z,S11,S22,S12,KTYPE,STRESSM,STRESSC)
C
C  COMPUTE STRESSES IN ADHEREINDS DUE TO REMOTE STRESSES
C
      COMMON/TOP/E3,T2,V1,SMX,SMY,G,CONS,Q,A1,SCON
      DIMENSION STRESSM(3),STRESSC(3)
      COMPLEX Z,CXSR,PHI,OMEGAB,DPHI,XK,ZB,SI
      IF(KTYPE.EQ.1)1,2
    1 CONTINUE
      ZB=CONJG(Z)
      PHI=STRESSM(2)*(Z/CXSR(Z,A1))/2.-.25*(STRESSM(2)-STRES
     1SM(1))
      OMEGAB=STRESSM(2)*(ZB/CXSR(ZB,A1))/2.+.25*(STRESSM(2)-
     1STRESSM(1))
      DPHI=-A1**2/(CXSR(Z,A1)*(Z**2-A1**2))
      DPHI=DPHI*STRESSM(2)/2.
      SI=CONJG(OMEGAB)-PHI-Z*DPHI
      XPHI=2*REAL(PHI)
      XK=XPHI+ZB*DPHI+SI
      S11=REAL(XPHI-(ZB*DPHI+SI))
      S22=REAL(XK)
```

```
      S12=AIMAG(XK)
      GO TO 3
    2 S11=STRESSC(1)
      S22=STRESSC(2)
      S12=STRESSC(3)
    3 CONTINUE
      RETURN
      END
       COMPLEX FUNCTION G(Z,W)
      COMPLEX Z,ZB,W,WB
      ZB=CONJG(Z)
      WB=CONJG(W)
        G=CLOG(W-Z)-CLOG(Z+WB)-CLOG(Z+W)+CLOG(WB-Z)
      RETURN
      END
      COMPLEX FUNCTION H(Z,W)
      COMPLEX Z,ZB,W,WB          ,CI
      CI=CMPLX(0.0,1.0)
      ZB=CONJG(Z)
      WB=CONJG(W)
      H=CLOG(W-Z)+CLOG(Z+WB)-CLOG(Z+W)-CLOG(WB-Z)
      H=CI*H
      RETURN
      END
      SUBROUTINE PLASTIC(SYIELD,GAD2,S,DR)
C
C   PERFORM INCREMENTAL PLASTIC ANALYSIS
C
      COMMON/ROT/Z9(10000),D(100),NALF
      COMMON/ADHES/TAD,GAD
       DIMENSION F(100),G(100),DR(100),NOF(100),NYIELD(100)
      KK=0
C
C   COMPUTE YIELD STRESS FOR EACH POINT
C   CHOOSE CRITICAL ELEMENT
C
        N=2*NALF
       NSQ=NALF
       SUM=0
        DO 55 I=1,NALF
        F(I)=0.0
         F(I+NALF)=0.0
   55    NOF(I)=0
      FCI=9999999999999.
   12    FCC=999999999.
      KK=KK+1
      DO 1I=1,NALF
        IF(NOF(I).EQ.1)GO TO 1
C
C   ADD LOGIC TO SKIP ALL YIELDED ELEMENTS
C
```

```
          A=D(I)**2+D(I+NALF)**2
           B=2*(F(I)*D(I)+F(I+NALF)*D(I+NALF))
           C=F(I)**2+F(I+NALF)**2-SYIELD**2/3.
           TEST=(-B+SQRT(B**2-4*A*C))/(2.*A)
        IF(TEST.LT.FCC)2,3
      2 K=I
        FCC=TEST
      3 CONTINUE
      1 CONTINUE
        IF(KK.EQ.1)FCI=FCC
        LL=K-1
            SUM1=SUM
         SUM=SUM+FCC
          IF(SUM.GT.S)5,6
 6         IF(FCC.EQ.999999999.)GO TO 18
          NOP(K)=1
        NYIELD(KK)=K
C
C SAVE STRESS IN EACH ELEMENT ATYIELDING
C
        DO 8 I=1,N
        F(I)=FCC*D(I)+F(I)
        G(I)=FCC*D(I)
     8 CONTINUE
C
C  MODIFY EQUATION SET FOR YIELDING OF CRITICAL ELEMENT
C
        I1=(K-1)*N+K
        I4=K+NALF
        I2=(I4-1)*N+I4
         Z9(I1)=Z9(I1)+TAD*(1./GAD2-1./GAD)
          Z9(I2)=Z9(I2)+TAD*(1./GAD2-1./GAD)
C
C USING AN ITERATIVE METHOD UPDATE ELEMENT STRESSES
C
        CALL GAUSS(DR)
          IF(KK.EQ.NALF)GO TO 18
        GO TO 12
     5 IF(KK.EQ.1)13,14
    13 PRINT 15
          SUM=0.
    15     FORMAT(/* THE SOLUTION IS COMPLETELY ELASTIC*/)
        GO TO 16
    14 CONTINUE
        KK=K-1
         SUM=SUM1
    18 CONTINUE
        PRINT 31,KK,SUM
    31 FORMAT(/I10* ELEMENTS HAVE YIELDED AT *E10.3/)
    16 CONTINUE
  1001 FORMAT(8E10.3)
```

```
      DO 26 I=1,NALF
      D(I)=(S-SUM)*D(I)+F(I)
        D(I+NALF)=(S-SUM)*D(I+NALF)+F(I+NALF)
   26 CONTINUE
      IF(KK.GT.1)25,29
   25 PRINT 27
   27 FORMAT(/* YIELDED ELEMENTS */)
      PRINT 28,(NYIELD(I),I=1,KK)
   28 FORMAT(12I10)
   29 CONTINUE
      PRINT 30,FCI
   30 FORMAT(' THE YIELD MACROSCOPIC STRESS IS *E11.3/)
      RETURN
      END
      SUBROUTINE GAUSS(DD)
C
C  GAUSS SEIDEL METHOD FOR SOLVING INCREMENTAL
C  PLASTIC SOLUTION
C
       DIMENSION DD(100),ASAVE(100)
      COMMON/ADHES/TAD,GAD
      COMMON/ROT/Z9(10000),D(100),NALF
      EPS=.005
      N=2*NALF
       NSQ=N*N
      ITMAX=20
        DO 33 I=1,N
       K=(I-1)*N+I
        ASTAR=Z9(K)
      ASAVE(I)=ASTAR
       DO 3 J=1,N
      II=(J-1)*N+I
      Z9(II)=Z9(II)/ASTAR
    3  CONTINUE
        DD(I)=DD(I)/ASTAR
   33    CONTINUE
      DO 9 ITER=1,ITMAX
       KFLAG=1
      DO 7 I=1,N
       XSTAR=D(I)
       D(I)=DD(I)
      DO 5 J=1,N
        II=(J-1)*N+I
      IF (I .EQ. J) GO TO 5
      D(I)=D(I)-Z9(II)*D(J)
    5 CONTINUE
      IF(ABS(XSTAR-D(I)).LE.EPS)GO TO 7
       KFLAG=0
    7 CONTINUE
        IF(KFLAG.NE.1)GO TO 9
         GO TO 1
```

```
    9 CONTINUE
      PRINT 204
    1 CONTINUE
C
C   RECONSTRUCT Z9 AND DD MATRIX FOR USE ON FUTUTRE
C   ELEMENTS THAT YIELD
C
        DO 330 I=1,N
        K=(I-1)*N+I
      ASTAR=ASAVE(I)
        DO 30 J=1,N
        II=(J-1)*N+I
        Z9(II)=Z9(II)*ASTAR
   30 CONTINUE
        DD(I)=DD(I)*ASTAR
  330 CONTINUE
  204 FORMAT(/* CAUTION THE GAUSS SEIDEL DID NOT CONVERGE*/)
      RETURN
      END
      FUNCTION YYX(X,B,A)
      COMMON/BOND/F,P1,P2,XKF,XKUNS,XKSTIFF
      IF(X.EQ.0)GO TO 4
      IF(X/A.GE.1)1,2
    2 YYX=B*((1.-(X/A)**P1)**(1./P2))
      GO TO 3
    1 YYX=0.
      GO TO 3
    4 YYX=B
    3 CONTINUE
      RETURN
      END
      FUNCTION YYD(X,B,A ,P)
      IF(X/A.GE.1)1,2
    2 YYD=B*((1.-(X/A)**P )**-(1./P ))
      GO TO 3
    1 YYD=0.
    3 CONTINUE
      RETURN
      END
```

LIST OF REFERENCES

Ames, W. F., Numerical Methods for Partial Differential Equations, (New York: Barnes and Nobel, 1971) pp. 15-23.

Armen, H., Jr., Pifko, A., and Levine, H. S., "Finite Element Analysis of Structures in the Plastic Range," NASA CR-1649, 1971.

Blichfeldt, R., and McCarty, J. E., "Analytical and Experimental Investigation of Aircraft Metal Structures Reinforced with Filamentary Composites," NASA CR-2039, 1972.

Burlington, R. S., Handbook of Mathematical Tables and Formulas, (New York: McGraw Hill, 1973) p. 89.

Calcote, L. R., The Analysis of Laminate Composite Structures, (New York: Van Nostrand Reinhold, 1969) pp. 115-123.

DenHartog, J. P., Advanced Strength of Materials, (New York: McGraw Hill, 1952) p. 252.

Dennemeyer, R., Introduction to Partial Differential Equations and Boundary Value Problems, (New York: McGraw Hill, 1968) pp. 133-136.

Durchlaub, E. C., and Freeman, R. B., "Design Data for Composite Structure Safelife Prediction," AFML TR-73-225, 1974.

Ellis, J. R., "The Demonstration of Advanced Metallic Technology in Primary Wing Structures," AIAA 76-908, 1976.

Erodogan, F., "Crack Propagation Theories," in Fracture V II 5.497-590 Liebowitz, H ED. (New York: Academic Press, 1968)

Erdogan, F., and Arin, K., "A Sandwich Plate with a Part-Through and Debonding Crack," Engineering Fracture Mechanics Vol. 4, 1972.

Figge, I. E., and Newman, J. C., "Fatigue Crack Propagation in Structures with Simulated Rivet Forces," Fatigue Crack Propagation, ASTM STP 415, Am. Soc. Testing Mats., 1967, p. 71.

Forman, R. G., Kearney, V. E., and Engle, R. M., "Numerical Analysis of Crack Propagation in Cyclic-Loaded Structures," Trans ASME, Ser. D.: J. Basic Eng, Vol. 89, No. 3, 1967, pp. 459-464.

Foye, R. L., and Baker, D. J., "Design of Orthotropic Laminates," AIAA/ASME 11th Conf. Structures, Structural Dynamics and Materials, 1970.

Griffith, A. A., (1921) Phil. Trans. Roy. Soc., London, Ser. A 221,163.

Halpin, J. C., Waddoups, M. E., and Johnson, T. A., "Kinetic Fracture Models and Structural Reliability," Int. J. Fracture Mechanics, Vol. 8, pp. 465-468, 1972.

Harvill, W. E., Kays, A., Young, E. C., and McGee, W. M., "Program for Establishing Long-Time Flight Service Performance of Composite Materials in the Center Wing Structure of C-130 Aircraft," NASA CR-112126, 1973.

Hardrath, H. F., "Vehicle Technology for Civil Aviation the Seventies and Beyond," NASA SP-292, 1971.

Hildebrand, F. B., Advanced Calculus for Engineers, (Englewood Cliffs, NJ: Prentice-Hall, 1957) pp. 532-533.

Hill, R., The Mathematical Theory of Plasticity, (London: Oxford University Press, 1960) p. 26.

Hoffman, D. J., and June, R. R., "Debonding of Adhesive Joints: Summary Report," NASA CR-2207, 1973.

Hudson, C. M., "Effect of Stress Ratio of Fatigue Crack Growth in 7075-T6 and 2024-T3 Aluminum Alloy Specimens," NASA TN-D-5390, 1961.

Hughes, E. J., and Rutherford, J. L., "Study of Micromechanical Properties of Adhesive Bonded Joints," Technical Report 3744, 1968.

Irwin, G. R., "Analysis of Stresses and Strains Near the End of a Crack Transversing a Plate," J. Appl. Mech., Vol. 24, 1957.

Johnson, W. S., and Stratton, J. M., "Effective Remote Stresses and Stress Intensity Factors for an Adhesive Bonded Multiply Laminates," Eng. Fracture Mechanics, Vol. 9, 1977.

Kula, E. B., Anctil, A. A., and Johnson, H. H., "Fatigue Crack Growth in Dual Hardness Steel Armor," ASTM STP 569, 1975.

Lekhnitskii, S. G., Anisotropic Plates, (New York: Gordon and Breach, 1968, 2nd Ed.) pp. 19-54, 130-134.

Lowndes, H. B., Jr., and Miller, W. B., "The U. S. Air Force Weapon Systems Fatigue Certification Program," Proceedings of the 4th Symposium of the International Committee on Aeronautical Fatigue, 1965.

MACSYMA Reference Manual Version Eight, Mathlab Group, MIT, Cambridge, Massachusetts, 1975.

McCracken, D. D., and Dorn, W. S., Numerical Methods and Fortran Programming. (New York: Wiley, 1968) p. 261.

McLaughlin, P. V., Jr., Kulkarni, S. V., Huang, S. N., and Rosen, B. W., "Fatigue of Notched Fiber Composite Laminates, Part I: Analytical Model" NASA CR-132747, 1975.

McMaster, R. C., "Nondestructive Testing Handbook," Vol. II (New York: Ronald Press Company, 1963) p. 43.35.

Military Specification MIL-A-83444 Airplane Damage Tolerance Requirements, 1974.

Mostovoy, S., Crosley, P. B., and Ripling, J. E., "Use of Crack-Line-Loaded Specimens for Measuring Plane-Strain Fracture Toughness," ASTM STP 490, 1967.

Mostovoy, S., and Ripling, E. J., "Fracture Toughness of an Epoxy System," J. Appl. Polymer Science, Vol. 10, pp. 1351-1371, 1966.

Muskhelishvili, N. I., Some Basic Problems of the Mathematical Theory of Elasticity, 2nd English Ed. (Netherlands: Noordhoff, 1975) passim.

Paris, P. C., Gomez, M. P., and Anderson, W. E., "A Rational Analytic Theory of Fatigue," The Trend in Engineering, Vol. 13, No. 1, 1961.

Ratwani, M. M., "Characterization of Crack Growth in Bonded Structures," Vol. I and II, AFFDL-TR-77-31, 1977.

Reifsnider, K. L., "Fatigue of Composite Materials," NATO AGARD Report No. 638, 1976.

Reifsnider, K. L., Stinchcomb, W. W., Williams, R. S., and Turgay, H. M., "Influence of Cycle Frequency on Composite Fatigue Reliability," AFOSR-TR-74-1201, 1974.

Renton, W. J., and Vinson, J. R., "The Analysis and Design of Composite Material Bonded Joints Under Static and Fatigue Loadings," AFSOR TR-73-0494, 1973.

Rich, M. J., and Wegle, R. T., Design, Analysis, and Test of a Boron/Epoxy Reinforced Airframe, AIAA No. 72-392, 1972.

Ripling, E. J., Mostovoy, S., and Patrick, R. L., "Adhesion-1963," ASTM STP 360, 1964.

Roderick, G. L., Everett, R. A., and Crews, J. H., Jr., "Debond Propagation in Composite Reinforced Metals," ASTM 569, pp. 295-306, 1975.

Roderick, G. L., Everett, R. A., and Crews, J. H., Jr., "Cyclic Debonding of Unidirectional Composite Bonded to Aluminum Sheet for Constant Amplitude Loading," NASA TN D-8126, 1976.

Roderick, G. L., and Whitcomb, J. D., "Fatigue Damage of Notched Boron/Epoxy Laminates Under Constant Amplitude Loading," ASTM STP 636, pp. 73-88, 1977.

Salkind, M. J., "Fatigue of Composites," ASTM STP 497, pp. 143-169, 1973.

Sanders, J. L., Jr., Journal of App. Mech, 27,352, 1960.

Shockey, P. D., Anderson, J. D., and Hofer, K. E., "Structural Airframe Applications of Advanced Composite Materials," Vol. V., AFML-TR-69-101, 1970.

Sih, G. C., and Liebowitz, H., "Mathematical Theories of Brittle Fracture," in Fracture Vol. II, Liebowitz ed., 1968.

Timoshenko, S. P., and Goodier, J. N., Theory of Elasticity, (New York: McGraw-Hill, 1951) p. 119.

Timoshenko, S. P., and Gere, J. M., Theory of Elastic Stability (New York: McGraw-Hill, 1961) pp. 1-3.

Volkerson, O., "Die Nietraftvertellung in zugbeanspruchten Nieverbindungen mit konstaten Laschenquerschnitten," Luftfahrtforschung, Vol. 15, 1938, pp. 41-47.

Wang, S. S., and Mandel, J. F., and McGarry, F. J., "Fracture of Adhesive Joints," MIT Research Report R76-1, Dept. of Materials Science and Eng., 1976.

Wylie, C. R., Jr., Advanced Engineering Mathematics, (New York: (McGraw-Hill, 1966), p. 188.

Yang, J. N., and Liu, M. D., "Residual Strength Degradation Model and Theory of Periodic Proof Tests for Graphite/Epoxy Laminates," Jor. Comp. Mat., Vol. II, April 1977.

Yoder, G. R., and Griffis, G. A., "J Integral and the Initiation of Crack Extension in a Titanium Alloy," NRL Report 7662, February 1974.

Zienkiewicz, O. C., The Finite Element Method in Engineering Science, (London: McGraw-Hill, 1971) pp. 435-471.

End of Document